Chapter 3

Characteristics of Vortex Flow at Long Time

As mentioned in Chapter 1, the flow characteristics associated with the air jet impinging onto the heated disk confined in the cylindrical space under investigation are affected by the jet inertia, buoyancy force due to the heated disk, and the geometry of the chamber including the injection pipe diameter and jet-to-disk separation distance. The present study intends to explore the effects of these parameters on the flow and thermal characteristics in the processing chamber. More specifically, in the present experiment the air flow rate Q_j is varied from 0.2 to 9.3 slpm (standard liter per minute) and the temperature difference between the heated plate and injected air ΔT is varied from 0 to 25.0℃ for two injection pipes with D_j=10.0 and 22.1 mm. Four jet-to-disk separation distances are considered with H=10.0, 15.0, 20.0, and 30.0 mm. The dimensionless groups governing the flow are the jet Reynolds number and the Rayleigh number. They are respectively defined as

$$Re_j = \overline{V}_j D_j / \nu = 4Q_j / \pi \nu D_j \qquad (3.1)$$

and

$$Ra = g\beta\Delta T H^3 / \alpha\nu \qquad (3.2)$$

In addition, the local Reynolds number and average radial velocity of the flow in the wall-jet region are respectively defined as

$$Re_w = \bar{u}H/\nu \qquad (3.3)$$

and

$$\bar{u} = Q_j / 2\pi rH = Re_j D_j \nu / (8rH) \qquad (3.4)$$

Hence Re_w can be rewritten as

$$Re_w = Re_j \cdot D_j / 8r \qquad (3.5)$$

Thus, in this part of the study the jet Reynolds number ranges from 12 to 1,258 and the Rayleigh number from 0 to 63,420. At this low Reynolds number the impinging

jet when unheated is laminar and steady, according to Chiriac and Ortega [40]. Only in examining the critical condition for the appearance of the inertia-driven and buoyancy-driven rolls, however, the maximum jet Reynolds number is increased to 1,258 (Q_j=9.3 slpm). The ranges of the parameters chosen above are in accordance with the values of the governing dimensionless groups for the flow often encountered in the CVD processes [4]. In what follows selected flow photos from the top and side views taken at steady or statistically stable state in the present study are examined closely to unravel how the jet Reynolds number, Rayleigh number, jet-to-disk separation distance and injection pipe diameter affect the recirculating gas flow patterns resulting from the impinging air jet in the processing chamber.

3.1 Typical steady vortex flow pattern

At first, the typical vortex flow pattern observed in the processing chamber with the jet issued from the small injection pipe (D_j=10.0 mm) at long time when the flow already reaches steady state for the case with a low buoyancy-to-inertia ratio Gr/Re_j^2 is illustrated in Fig. 3.1. Here Gr is the Grashof number and Gr=Ra/Pr. In the figure the steady flow photos from the top and side views taken respectively at the selected horizontal and vertical planes along with the schematic sketch of the flow based on the detailed flow visualization for a typical case with Q_j=3.0 slpm, ΔT=10.0℃ and H=15.0 mm (Re_j=406, Ra=3,170 and Gr/Re_j^2=0.019) are shown. Since the flow is axisymmetric at this low Gr/Re_j^2, only a half of the top view flow photo and the side view flow photo at the vertical plane θ=0° & θ=180° are given here. Examining the top and side view photos together reveals that the steady vortex flow consists of three circular vortex rolls in the processing chamber. The first (inner) circular roll directly surrounds the downward air jet and is much larger than the

second vortex roll induced in the middle zone of the chamber. The third (outer) roll is also large in size and dominates in the outer zone of the chamber. A close inspection of the successive top and side view flow photos in the video tapes taken during the transient stage of the flow formation indicates that immediately after the impinging, the jet is deflected by the circular disk to move obliquely upwards (Fig. 3.1(c)). Then the oblique flow is divided into two streams as it encounters the chamber top. One stream moves radially inwards towards the low pressure region created by the jet injection forming the inner toroidal vortex, which is considered as the primary inertia-driven vortex roll. This inner roll is also entrained by the jet and is normally stronger and larger at a higher jet Reynolds number. Another stream moves radially outwards, later turns to move downwards along the sidewall of chamber, and finally leaves the chamber through the outlets in the chamber bottom. Besides, the smaller second circular roll is found to be induced through the viscous shearing effects produced by the stronger and larger inner vortex roll, which is termed as the secondary inertia-driven roll. Moreover, the local maximum pressure occurs at the stagnation point and sharply decreases to minimum value after stagnation point. The local pressure after minimum value gradually increases since the available flow area increases as the air flows past the center of the primary inertia-driven roll. In the pressure recovering region, the positive pressure gradient enhances the occurrences of the flow separation. It should be mentioned that this secondary roll is induced only when the jet Reynolds number exceeds certain level around 180 for the small injection pipe (D_j=10.0 mm) when the disk is unheated with Ra=0. Moreover, the outer roll near the cold chamber side is driven by the buoyancy force associated with the heated disk and is regarded as the buoyancy-driven roll. For the large injection pipe (D_j=22.1 mm) at the same gas flow rate the secondary inertia-driven roll is weaker and smaller since the jet

Reynolds number is much lower (Equ. (3.1)). In addition, for a further increase in the jet Reynolds number a small circular roll appears near the top wall around the impinging jet at D_j=10.0 mm and it is considered as the tertiary inertia-driven roll. At this high Re_j for the small injection pipe the primary roll is strong enough to induce a tertiary roll through the viscous shearing of the stagnant flow around the primary roll. For D_j=22.1 mm the range of the jet Reynolds number covered in the present study is not high enough to induce a tertiary roll. The inertia-driven steady tertiary flow is illustrated in Fig. 3.2 by showing the steady side view flow photos taken at the cross plane $\theta=0^\circ$ for slightly supercritical jet Reynolds numbers at various jet-to-disk separation distances for D_j=10.0 mm. Since the steady flow is still axisymmetric, only the results in the half plane are shown. The results in Fig. 3.2 manifest that the tertiary roll is small and appears in the region near the chamber top adjacent to the primary inertia-driven roll. The primary, secondary and tertiary inertia-driven rolls are smaller at the smaller jet-to-disk separation distance. This simply reflects the fact that at a smaller H the available space in the processing chamber for the rolls to develop is less. Note that at H=10.0 mm the tertiary roll is rather small. Besides, the tertiary roll grows slightly in size and in vortex intensity with the jet Reynolds number. At the larger jet-to-disk separation distance for H=20.0 mm the growth of the tertiary roll with Re_j is slightly larger, as evident from the results in Fig. 3.2(a). Moreover, the tertiary roll becomes smaller and weaker for an increase in Ra.

3.2 Onset of inertia- and buoyancy-driven vortex flow

The understanding of the critical condition for the appearance of the inertia- and buoyancy-driven vortex rolls in the chamber is of fundamental interest in the fluid flow study. Here we investigate the onset of the inertia-driven rolls by

visualizating the flow in the processing chamber at various jet Reynolds numbers for an unheated disk (Ra=0). Note that the lowest jet flow rate which can be accurately resolved in the present experimental apparatus is 0.1 slpm. Even at this small Q_j the primary inertia-driven roll is already seen in the chamber for all H with the jet issued from the small injection pipe (D_j=10.0 mm). For the large injection pipe (D_j=22.1 mm) the critical Re_j for the onset of the primary inertia-driven roll is somewhat higher and thus can be located here. The present data are summarized in Table 3.1 for the onset of the primary and secondary inertia-driven rolls at various jet-to-disk separation distances. The results suggest that as the jet Reynolds number exceeds certain low level the primary inertia-driven roll appears. The secondary inertia-driven roll is initiated at somewhat higher jet Reynolds numbers (Table 3.1). Some inertia-driven rolls at slightly supercritical Re_j are shown in Fig. 3.3 for the jet-to-disk separation distance fixed at 20.0 mm. The results manifest that the primary inertia-driven roll is much smaller and weaker for the large injection pipe (Figs. 3.3 (c) & (d)). More specifically, for D_j=10.0 and 22.1 mm the primary inertia-driven roll respectively appears at Re_j=13.6 and 15. Note that at the low Re_j near the critical level the roll is relatively small and appears near the exit of the injection pipe (Figs. 3.3 (a) & (d)). It should be mentioned that for an unheated disk an outer roll also appears in the duct (Figs. 3.3 (a) & (b)). This roll is formed by the deflection of the wall-jet flow along the disk by the chamber side. At a higher Re_j this outer roll is smaller and weaker (Fig. 3.3(b)) due to the radial thickening of the boundary layer flow along the disk and the deflection of the flow at the chamber side is milder. It has nothing to do with buoyancy effect since Ra=0. Besides, the onset conditions of the tertiary inertia-driven roll are also given in the table. It is of interest to note that at a smaller jet-to-disk separation distance the primary inertia-driven roll is induced at a slightly higher jet Reynolds number, as evident

from comparing the results in Figs. 3.4 and 3.5.

The results summarized in Table 3.1 indicate that at given D_j the critical jet Reynolds numbers for the onset of the primary, secondary and tertiary inertia-driven rolls increase when the jet-to-disk separation distance is reduced from 20.0 mm to 10.0 mm. However, it is of interest to note that the critical Re_j does not experience any change when H is reduced from 30.0 to 20.0 mm for the primary and tertiary rolls. The increase of the critical Re_j at decreasing H is conjectured to mainly result from the more significant retarding of the jet by the disk at a smaller H, which in turn yields a higher viscous damping effect on the impinging jet and a higher Re_j is needed to induce the flow recirculations.

As we continue to increase the jet Reynolds number slightly beyond the critical Re_j for the onset of the tertiary roll, the flow in the processing chamber does not reach any steady state at long time. Instead, the flow becomes time dependent and experiences a transition from steady to unsteady states. Obviously, this transition is driven by the jet inertia since $\Delta T=0$ and no buoyancy-driven rolls appear. The present data for the inertia driven steady-to-unsteady transition are summarized in Table 3.2 for D_j=10.0 mm. The results indicate that the critical Re_j for this flow transition increases when the jet-to-disk separation distance is shortened, similar to those for the onset of the inertia-driven rolls. It is of interest to note that the critical Re_j for this steady-unsteady transition increases with Ra at given H. The above results suggest that the time-dependent flow induced by the jet inertia can be stabilized by increasing the Rayleigh number Ra at $H \leqq 20.0$ mm. However, for H=30.0 mm an opposite trend is noted. This is due to the fact that at the longest H (=30.0 mm) tested here the radial extent of the buoyancy-driven roll is so large and it directly contacts with the primary inertia-driven roll. As Re_j gradually increases, both the primary inertia-driven and buoyancy-driven rolls squeeze each other

resulting in time-dependent flow.

When the disk is heated, our flow visualization further shows that for given D_j, ΔT and H the buoyancy-driven roll begins to appear in the region near the heated disk edge as Re_j is below certain critical level for a given Ra. This critical condition is considered to be reached as long as we can barely see the buoyancy-driven roll in the video films recording the images of the vortex rolls. This is exemplified in Fig. 3.6. Moreover, Table 3.3 summarizes the critical condition for the onset of the buoyancy-driven roll based on the present data. The data indicate that for given D_j and H the critical Re_j for the onset of the buoyancy driven roll is higher for a higher Gr. It should be mentioned that how the onset condition of the buoyancy roll is affected by the jet-to-disk separation distance is reflected in the Grashof number since Gr is proportional to H^3. Note that the critical buoyancy-to-inertia ratio Gr/Re_j^2 for the onset of the buoyancy roll is nearly constant for a given D_j, irrespective of the jet-to-disk separation distance. For D_j=10.0 and 22.1 mm the critical ratio Gr/Re_j^2 is nearly equal to 0.0045 and 0.021, respectively. It is also noted that the onset of the buoyancy-driven roll occurs when the wall-jet flow in the radial direction is reversed by the upward buoyancy associated with the heated disk and hence the onset should be mainly determined by the local flow condition characterized by the local Reynolds number of the wall-jet flow Re_w and the Grashof number Gr. Besides, the onset is most likely to take place near the outer edge of the disk. Therefore, the onset condition is expected to depend primarily on the local buoyancy-to-inertia ratio Gr/Re_w^2. The data given in Table 3.3 do show that the buoyancy roll begins to appear when the local buoyancy-to-inertia ratio at the edge of the disk Gr/Re_{we}^2 is around 33.0 with the deviations within the experimental uncertainty for all D_j and H considered.

3.3 Effects of jet Reynolds number

How the Reynolds number of the impinging jet affects the gas flow pattern at long time in the processing chamber is demonstrated in Figs. 3.7-3.12 by presenting the steady side view flow photos for the cross plane θ=0° & 180° for selected Ra at various jet Reynolds numbers for two injection pipes with the jet-to-disk separation distance H=20.0 mm. As the disk is unheated, apparently the primary and secondary inertia-driven rolls are dominated by the jet flowrate for a fixed H (Fig. 3.7). The secondary inertia-driven roll first appears in the processing chamber when Re_j approximately exceeds 180 for D_j=10.0 mm and 220 for D_j=22.1 mm. The inertia-driven rolls grow in size and intensity and its center moves radially outward at increasing Re_j. It should be mentioned that for an unheated disk an outer roll also appears in the chamber, as mentioned earlier (Fig. 3.7). This roll results from the deflection of the wall-jet flow along the disk by the chamber side. At a higher Re_j this outer roll is smaller due to the radial thickening of the boundary layer flow along the disk and the deflection of the flow at the chamber side is milder. It is nothing to do with the buoyancy effect since Ra=0. When the disk is heated with ΔT=5.0℃ (Ra=3,760), the results in Fig. 3.8(a) for the small injection pipe indicate that at this low buoyancy the gas flow in the chamber is still dominated by the three circular vortex rolls as the typical flow pattern shown in Fig. 3.1. We further note from Fig. 3.8(a) that at increasing Reynolds number the primary and secondary inertia-driven rolls grow in size and intensity with the accompanying decay of the buoyancy-driven roll. Similar trend is noted in Figs. 3.9-3.12 for the high buoyancies. In general, the stronger forced flow for a higher Re_j suppresses the buoyancy effects. Besides, the results clearly show that at higher Re_j(≧406) the secondary inertia-driven roll can be large enough to merge with the buoyancy-driven roll for the small injection pipe (Figs. 3.9(a)-3.12(a)). The gas flow in the chamber

then is dominated by two large circular vortex rolls. Additionally, it is important to note from the results in Figs. 3.7(b) and 3.8(b) that for the large injection pipe even at $Re_j \geqq 245$ the secondary inertia-driven roll disappears as Ra increases from 0 to 3,760 and higher, so we only have two circular vortex rolls in the chamber. Besides, the primary inertia-driven roll for the large injection pipe is much weaker than that for the small injection pipe. It is also interesting to note that at the higher Ra the size of the primary inertia-driven roll changes insignificantly with the jet Reynolds number (Figs. 3.10-3.12).

It is of interest to investigate the effects of the jet Reynolds number on the vortex flow patterns in the processing chamber for a shorter jet-to-disk separation distance. This is shown in Figs. 3.13-3.17 for H=15.0 mm. These results, qualitatively similar to those for the larger H given in Figs. 3.7-3.12, indicate that for H=15.0 mm we still have three circular rolls in the chamber for the higher Re_j. The inertia-driven rolls also increase in size and intensity at increasing Re_j except at high Ra (Fig. 3.17). The secondary inertia-driven roll is seen in the processing chamber at $Re_j \geqq 270$ for D_j=10.0 mm and at $Re_j \geqq 306$ for D_j=22.1 mm (Fig. 3.13) when the disk is unheated. A close inspection of the results in Figs. 3.7-3.17 does reveal some differences in the vortex flow patterns for the change in the jet-to-disk separation distances. Besides, the inertia and buoyancy-driven rolls are much smaller for the smaller H and the merging of the secondary inertia-driven roll and buoyancy-driven roll does not occur even at the highest Ra considered here. The corresponding top view flow photos for several selected cases shown in Figs. 3.18-3.21 for H=15.0 mm clearly demonstrate the circular nature of the vortex rolls for the lower Ra.

For completeness, the long time vortex flow patterns in the processing chamber are presented in Figs. 3.22-3.30 for various Re_j for the smallest jet-to-disk separation distance considered here with H=10.0 mm. Similar trends are again noted.

But at this smallest H no secondary inertia-driven roll is induced even for Re_j=306 for the large injection pipe. It is important to note that at this H (=10.0 mm) the buoyancy-driven vortex flow is somewhat different especially at low Re_j. More specifically, at the high buoyancy-to-inertia ratio for the small Re_j the steady buoyancy-driven vortex flow consists of two small circular rolls (Figs. 3.24-3.27).

3.4 Effects of Rayliegh number

The effects of the Rayleigh number on the recirculating flow patterns in the chamber are illustrated in Figs. 3.31 & 3.32 by showing the steady side view flow photos for various Ra at given Q_j for the fixed jet-to-disk separation distance H=20.0 mm. Some selected side view and top view photos are displayed together in Figs. 3.33 and 3.34. We first note from the results for the unheated disk (Ra=0) that the outer roll due to the flow deflection at the chamber side is rather small and weak for the large injection pipe (Figs. 3.31(b) & 3.32(b)). As the disk becomes heated, the buoyancy-driven roll grows significantly in size and intensity with the Rayleigh number. Note that in the chamber installed with the small injection pipe the buoyancy-driven roll at certain high Ra can be large enough to merge with the secondary inertia-driven roll (Figs. 3.31(a) and 3.32(a) at Ra=15,030). Thus, at certain high Ra ($\geqq$15,030) there are only two steady circular rolls in the chamber. The situation is somewhat different for the large injection pipe due to the absence of the secondary inertia-driven roll (Figs. 3.31(b) and 3.32(b)). More specifically, the radial size growth of the buoyancy-driven roll with Ra is milder for the large injection pipe. Additionally, for the both injection pipes significant size growth of the primary inertia-driven roll with Ra occurs except for H=10.0 mm.

For the smaller jet-to-disk separation distance of 10.0 mm and 15.0 mm, the effects of the Rayleigh number on the vortex flow in the chamber are similar to

those for H=20.0 mm, as evident from the results in Figs. 3.35-3.42. Note that the Rayleigh number is proportional to H^3 according to Equation (3.2) and hence the buoyancy effects are much weaker for the smaller H for the range of ΔT examined here. The buoyancy-driven roll is smaller and it does not have a chance to merge with the secondary inertia-driven roll.

3.5 Effects of processing chamber geometry

In addition to the physical parameters—Reynolds and Rayleigh numbers, the geometry of the processing chamber including the injection pipe diameter and jet-to-disk separation distance is also expected to significantly affect the vortex flow in the processing chamber. This is the direct consequence of the simple fact that at given Q_j and ΔT the jet Reynolds number Re_j is inversely proportional to the injection pipe diameter D_j and the Rayleigh number Ra is proportional to the third power of the jet-to-disk separation distance H (Equs. (3.1) & (3.2)). In view of the dependence of Re_j and Ra on D_j and H, we examine the effects of the chamber geometry on the flow by comparing the results for different D_j and H at the same jet flowrate Q_j and disk-to-jet temperature difference ΔT.

First, the effects of the injection pipe diameter on the vortex flow pattern are illustrated in Figs. 3.43-3.47 by showing the steady side view flow photos at the same Q_j and ΔT for different jet-to-disk separation distances. The results in Fig. 3.43 indicate that the outer roll near the chamber side is larger for the small injection pipe with the disk unheated. The size of the corner roll increases slightly with the jet Reynolds number for both injection pipes. Besides, for the jet issuing from the large injection pipe the secondary inertia-driven roll appears at lower Re_j and it is weaker and smaller at the same Q_j than that for D_j=10.0 mm. As the disk is heated, the buoyancy-driven roll is substantially larger for the small injection pipe at certain

high Q_j since it merges with the larger secondary inertia-driven roll (Figs. 3.44(b) and (d)). However, the radial extent of the primary inertia-driven roll is somewhat larger for the large injection pipe as the disk heated. At certain small jet-to-disk separation distance the size of the primary inertia-driven and the buoyancy-driven roll is less affected by the injection pipe diameter (Figs. 3.45-3.47).

The effects of the jet-to-disk separation distance on the flow pattern are shown in Figs. 3.48-3.51 for both injection pipes at given temperature differences. We first note from Figs. 3.48 and 3.50 that the centers of the inertia-driven rolls in the chamber significantly move radially outward owing to the increase of the jet-to-disk separation distance from 10.0 to 30.0 mm for the unheated disk (Ra=0). Moreover, the size of the corner roll in the outer region of the chamber increases substantially with the jet-to-disk separation distance for D_j=10.0 mm (Fig. 3.48). Nevertheless, for the large injection pipe (D_j=22.1 mm) the corner roll is small and is insignificantly affected by the jet-to-disk separation distance (Fig. 3.50). As the disk is heated, the results in Figs. 3.49 and 3.51 clearly indicate that the buoyancy-driven roll which dominates in outer region of the processing chamber is much bigger for a larger H. This large increase in the size of the buoyancy-driven roll with the jet-to-disk separation distance is due to the large increase in Ra associated with a small increase in H since Ra is proportional to H^3. Moreover, the size of the inertia- and buoyancy-driven rolls for both injection pipes increases with the jet-to-disk separation distance. However, the results in Fig. 3.49(b) show that the radial extent of the buoyancy-driven roll for H=30.0 mm is not larger than that for H=20.0 mm because the secondary inertia-driven roll merging with the buoyancy-driven roll at a higher Re_j for the small injection pipe and for H=20.0 mm. It is of interest to note that at the longest H (=30.0 mm) tested here the radial extent of the primary inertia-driven roll is so large and it directly contacts with the buoyancy-driven roll as

the disk heated. Thus, no space is available for the secondary inertia-driven roll to emerge. Only two circular vortex rolls appear in the chamber for H=30.0 mm.

3.6 Size and Location of the Vortex Rolls

To quantify the effects of the governing parameters on the vortex flow characteristics, the data for the maximum radial extent of the inner roll S_I, the maximum height of the outer roll S_O, and the radial location of the center of the secondary roll r_s are measured from the steady side view flow photos for various cases tested in the present study. The results from this measurement are shown in Figs. 3.52-3.53, which indicate that S_I increases almost linearly with the jet Reynolds number for a given Ra. The increase is more significant for smaller H and Ra. A close inspection of the data reveals that at the small H of 10.0 mm the increase of S_I with Re_j is substantially larger. However, S_O decreases due to an increase in Re_j. We also note that the increase in the size of the inner and outer rolls with the Rayleigh number can be substantial at low Ra. To facilitate the flow design in the practical application, empirical equations are proposed to correlate the above data. They can be expressed as

(a) size of the primary inertia-driven roll

$$\frac{S_I}{H} = 1.852 + 7.287\times10^{-5}\,Ra + 0.00229\,Re_j \qquad (3.6)$$

for 0≤ Ra≤ 18,790, 61≤ Re_j≤ 6 76, 10.0 mm≤ D_j≤ 22.1 mm and 10.0 mm≤ H≤ 20.0 mm,

(b) size of the buoyancy-driven roll

$$\frac{S_O}{H} = 0.0433 + 0.00444Ra^{0.5} + 3.45\,Re_j^{-0.5} \qquad (3.7)$$

for 470≤ Ra≤ 18,790, 61≤ Re_j≤ 676, 10.0 mm≤ D_j≤ 22.1 mm and 10.0 mm≤ H≤ 20.0 mm,

(c) location of the secondary inertia-driven roll for D_j =10.0 mm

$$\frac{r_s}{D_j} = 3.283 + 0.000205\mathrm{Ra} + 0.00316\,\mathrm{Re}_j \qquad (3.8)$$

for 0≤ Ra≤ 7,930, 270≤ Re_j≤ 676 and 10.0 mm≤ H≤ 20.0 mm.

When compared with the present data, the standard deviations of Equs. (3.6)-(3.8) are respectively 12%, 13% and 12%.

3.7 Steady temperature distribution in vortex flow

In addition to the vortex flow characteristics presented above, selected results from the measured steady air temperature distributions in the vortex flow are shown in Figs. 3.54-3.57 along the horizontal line at the middle horizontal plane between the disk and chamber top Z=0.5 at θ=0°. The non-dimensional air temperature Φ is defined as $(T-T_j)/(T_f-T_j)$. Note that in the region dominated by the primary inertia-driven roll the air temperature increases with the radial distance measured from the jet axis. The air temperature reaches a maximum in the region when the wall-jet separates from the disk surface and moves obliquely upwards. Beyond that the air temperature starts to decline. Near the chamber side the temperature decline is relatively sharp due to the presence of the buoyancy-driven roll. Moreover, a sharper temperature decline at a lower Re_j for a given ΔT results from the stronger buoyancy roll. We also note that for a smaller jet-to-disk separation distance the air temperature in the middle horizontal plane is slightly lower. This is considered to result from the higher mean radial flow speed in the wall-jet region in the chamber with a smaller H for a given Q_j. Thus the above nonmonotonic radial air temperature distributions for a given H result directly from the presence of the counter-rotating primary inertia-driven and buoyancy-driven vortex rolls in the chamber and the deflection of the impinging jet flow by these rolls. A close examination of these data

further reveals that at increasing jet Reynolds number the temperature peak moves away from the jet axis and the temperature decay in the region near the chamber side is smaller, reflecting from the fact that we have a larger primary inertia-driven roll and a weaker buoyancy-driven roll for a higher Re_j.

Table 3.1 Critical condition for appearance of the inertia-driven vortex roll ($\Delta T=0^{\circ}C$).

Vortex Roll	Separation distance (H, mm)	Jet diameter (D_j, mm)	Flowrate (Q_j, SLPM)	Re_j
Primary inertia-driven roll	30.0	22.1	0.25	15
	20.0	22.1	0.25	15
	15.0	22.1	0.3	18
	10.0	22.1	0.7	43
Secondary inertia-driven roll	30.0	10.0	0.8	108
		22.1	3.3	202
	20.0	10.0	1.3	180
		22.1	3.6	220
	15.0	10.0	1.7	230
		22.1	4.9	300
	10.0	10.0	1.8	245
		22.1	7.0	430
Tertiary inertia-driven roll	30.0	10.0	5.0	676
	20.0	10.0	5.0	676
	15.0	10.0	5.5	744
	10.0	10.0	7.0	947

Table 3.2 Critical condition for onset of time-dependent flow for D_j=10.0 mm.

H (mm)	ΔT (℃)	Gr	Q_j (slpm)	Re_j
10.0	0	0	7.7	1041
	5.0	652	8.6	1163
	10.0	1,304	8.6	1,163
	15.0	1,957	8.7	1,177
	20.0	2,609	9.0	1,217
	25.0	3,262	9.3	1,258
15.0	0	0	6.2	839
	5.0	2,202	6.5	879
	10.0	4,404	6.7	906
	15.0	6,606	6.9	933
	20.0	8,808	7.1	960
	25.0	11,010	7.2	974
20.0	0	0	5.9	798
	5.0	5,220	6.2	839
	10.0	10,439	6.5	879
	15.0	15,658	6.9	933
	20.0	20,878	7.2	974
	25.0	26,098	7.3	987
30.0	0	0	5.9	798
	5.0	18,120	5.7	771
	10.0	36,240	5.5	744
	15.0	54,360	5.0	676
	20.0	72,480	4.5	609
	25.0	90,600	3.5	473

Table 3.3 Critical condition for onset of the buoyancy-driven vortex roll.

Jet diameter (D_j, mm)	Separation distance (H, mm)	Gr	Re_j	Gr/Re_j^2	Gr/Re_{we}^2	Deviation (%)
10.0	20.0	3,340	879	0.0043	32.3	2.2
		4,200	947	0.0047	35.0	5.9
		5,220	1,082	0.0045	33.3	0.8
	15.0	1,321	541	0.0045	33.7	2.0
		2,202	676	0.0048	36.0	9.0
	10.0	1,304	541	0.0044	33.3	0.8
		1,957	676	0.0043	32.0	3.1
22.1	20.0	3,340	398	0.021	32.2	2.5
		4,200	459	0.020	30.5	7.7
		5,220	520	0.019	29.5	10.7
	15.0	1,321	245	0.022	33.7	2.0
		2,202	306	0.024	35.9	8.7
	10.0	1,304	245	0.022	33.2	0.5
		1,957	306	0.021	31.9	3.4

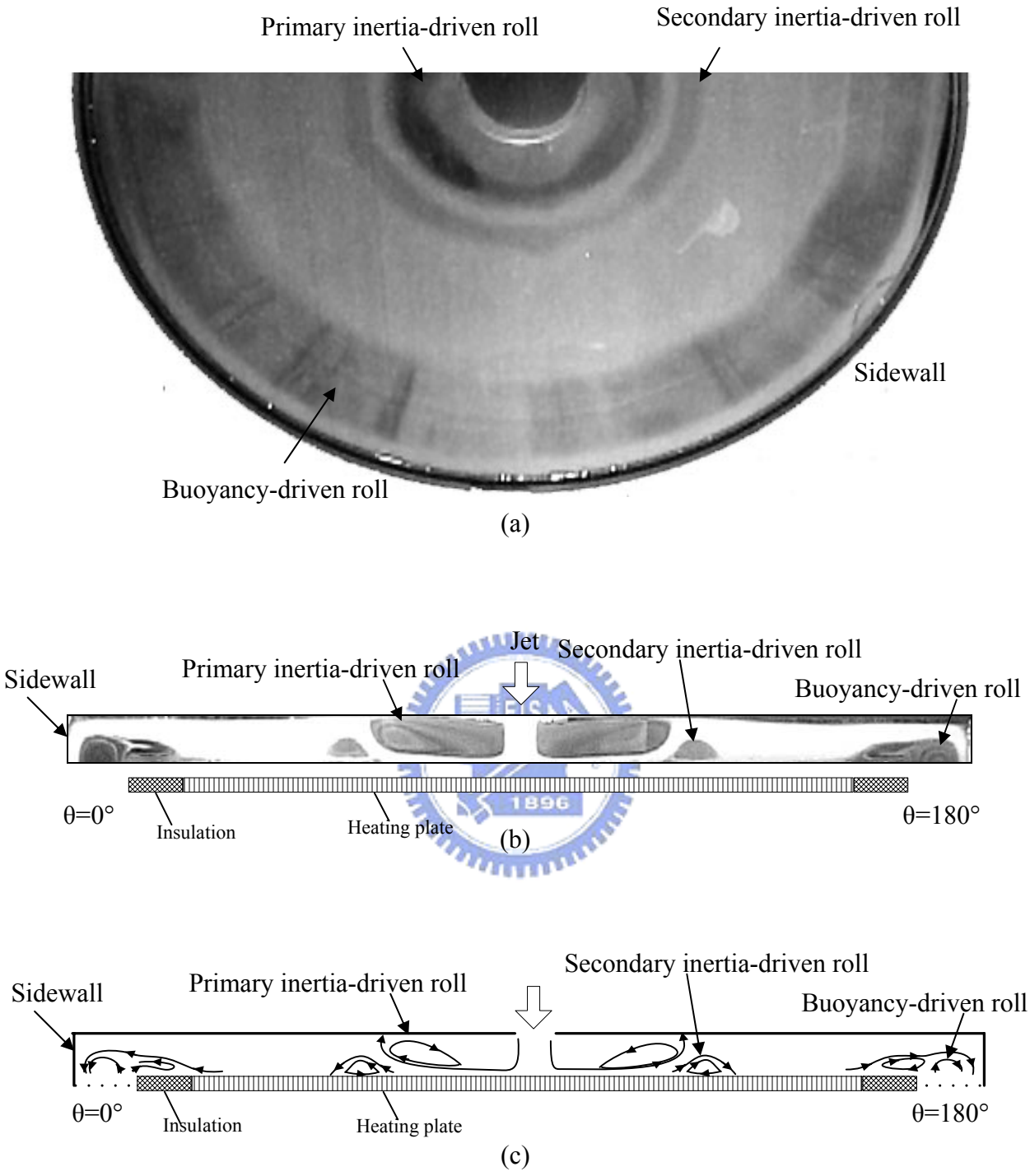

Fig. 3.1 Steady vortex flow pattern for D_j=10.0 mm and H=15.0 mm at Re_j=406 (Q_j=3.0 slpm) and Ra=3,170 (ΔT=10.0℃): (a) top view flow half of photo taken at the middle horizontal plane between the disk and chamber top, (b) side view flow photo taken at the vertical plane θ=0° & 180° and (c) the corresponding schematically sketched cross plane vortex flow.

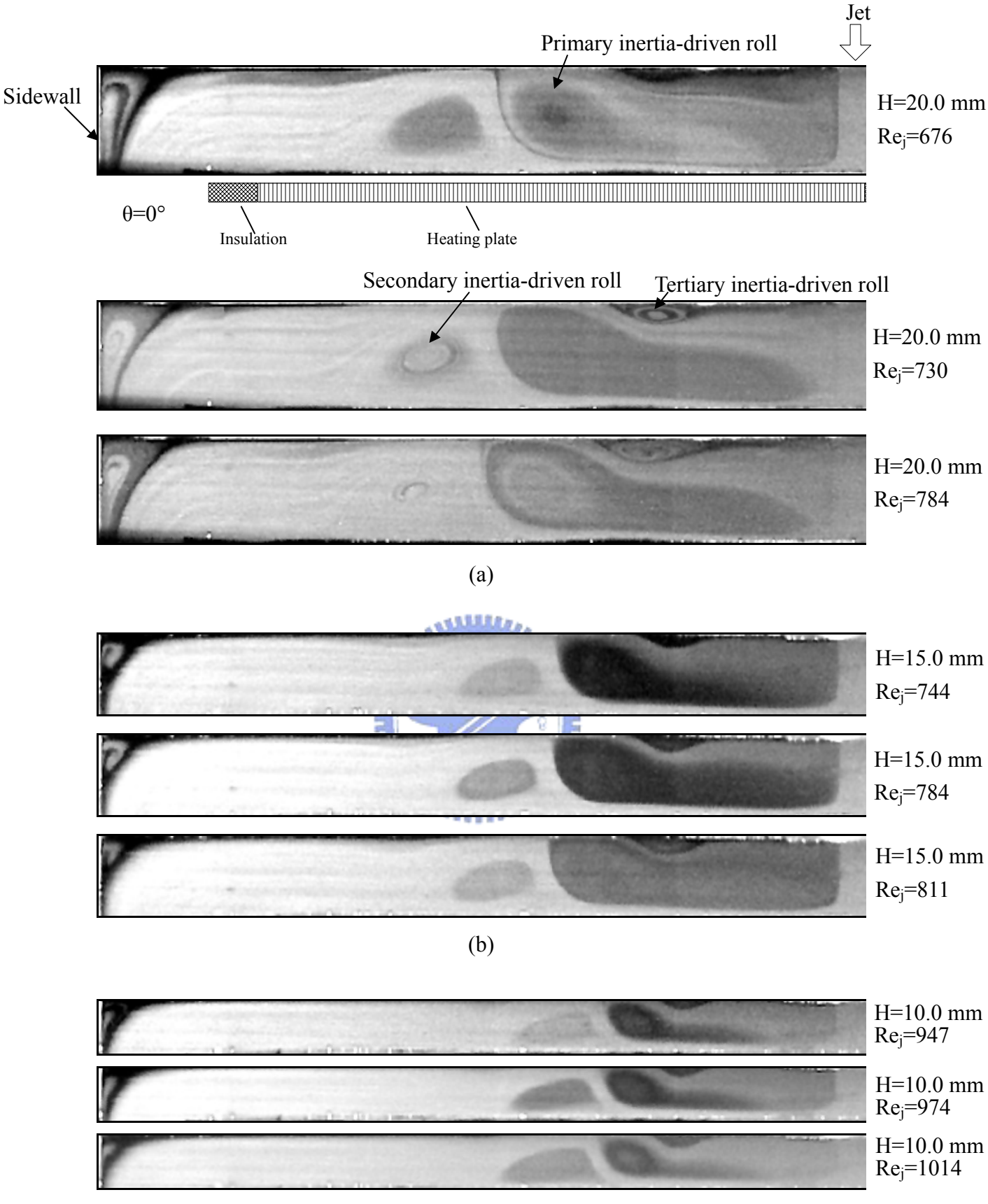

Fig. 3.2 Steady side view flow photos taken at the cross plane θ=0° for various Re_j to illustrate the tertiary inertia-driven roll with Ra=0 & D_j=10.0 mm for (a) H=20.0 mm, (b) H=15.0 mm, and (c) H=10.0 mm.

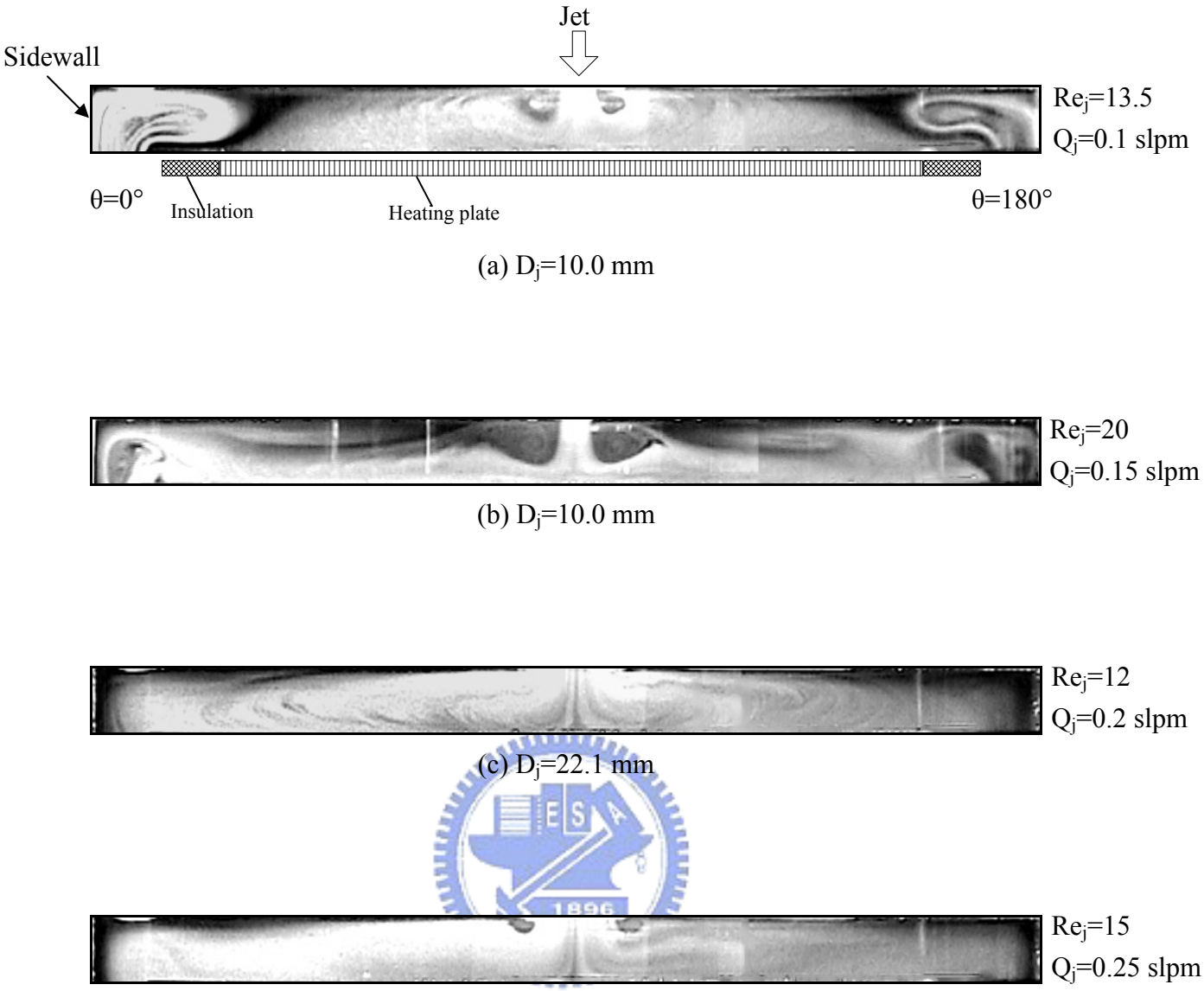

Fig. 3.3 Steady side view flow photos at low Reynolds numbers for Ra=0 & H=20.0 mm: (a) Re$_j$=13.6 & D$_j$=10.0 mm, (b) Re$_j$=20.0 & D$_j$=10.0 mm, (c) Re$_j$=12.0 & D$_j$=22.1 mm, and (d) Re$_j$=15.0 & D$_j$=22.1 mm.

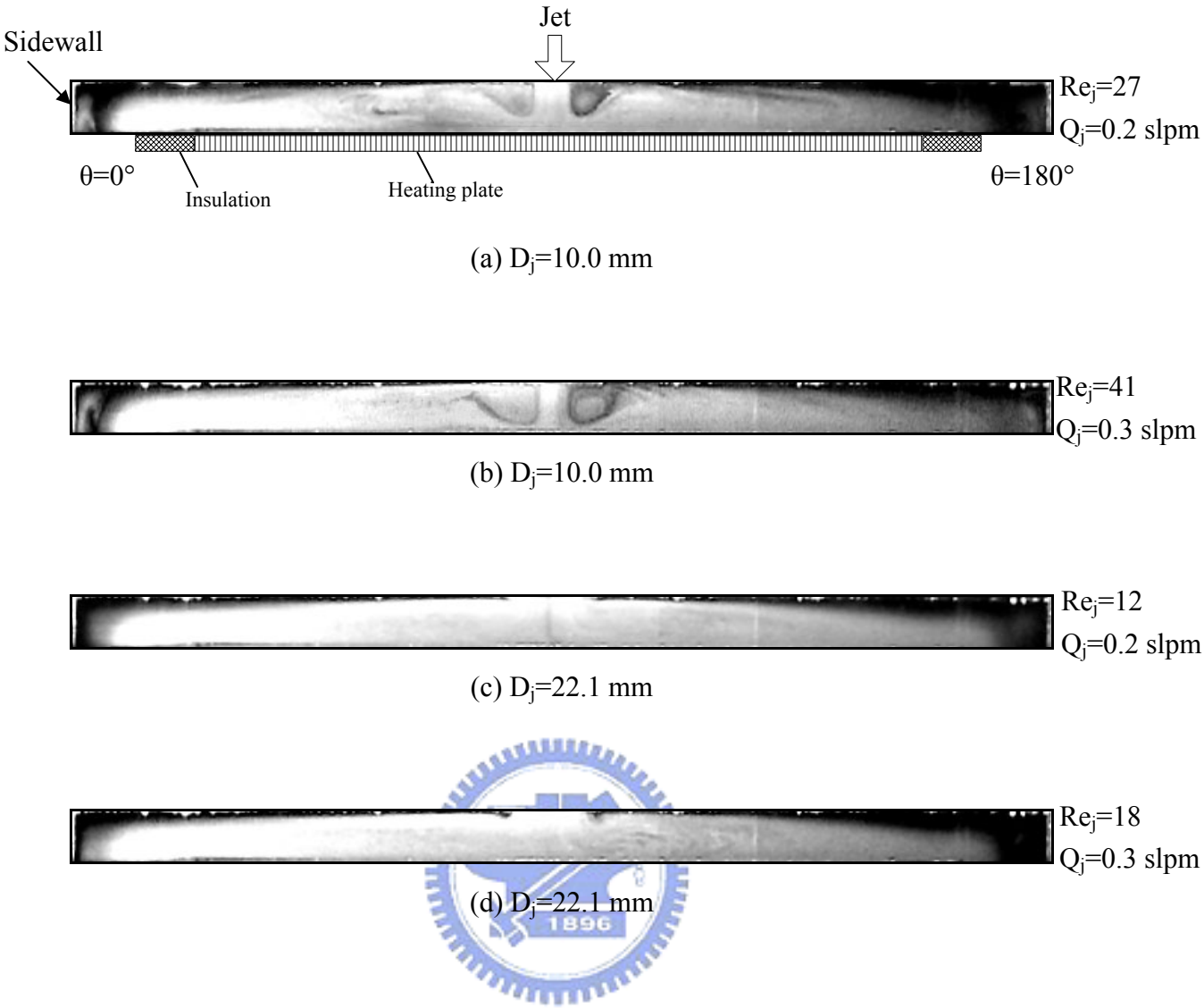

Fig. 3.4 Steady side view flow photos at low Reynolds numbers for Ra=0 & H=15.0 mm at Re$_j$ = (a) 27 & D$_j$=10.0 mm, (b) 41 & D$_j$=10.0 mm, (c) 12 & D$_j$=22.1 mm, and (d) 18 & D$_j$=22.1 mm.

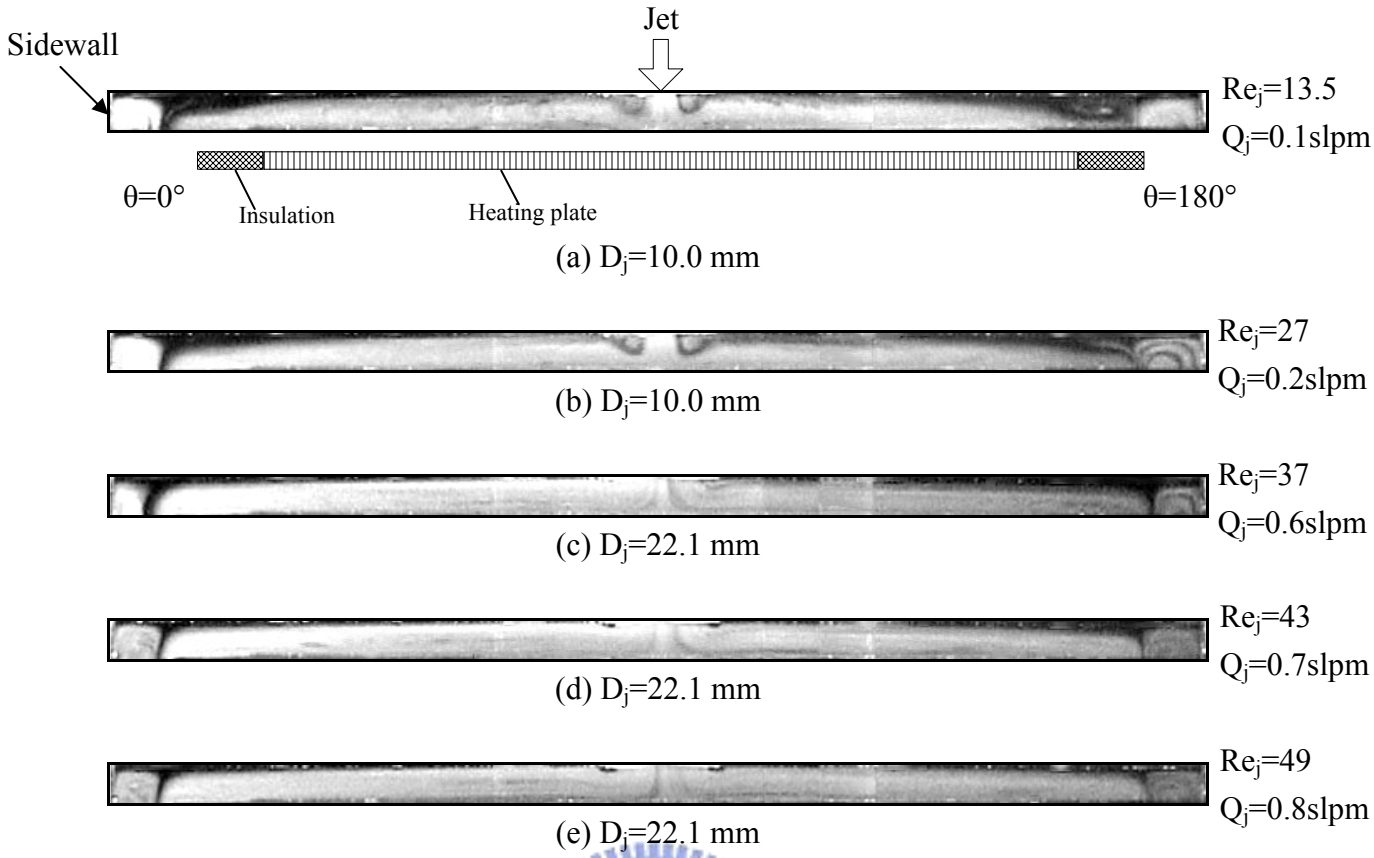

Fig. 3.5 Steady side view flow photos at low jet Reynolds numbers for Ra=0 with H=10.0 mm at Re_j = (a) 13.5 & D_j=10.0 mm, (b) 27 & D_j=10.0 mm, (c) 37 & D_j=22.1 mm, (d) 43 & D_j=22.1 mm, and (e) 49 & D_j=22.1 mm.

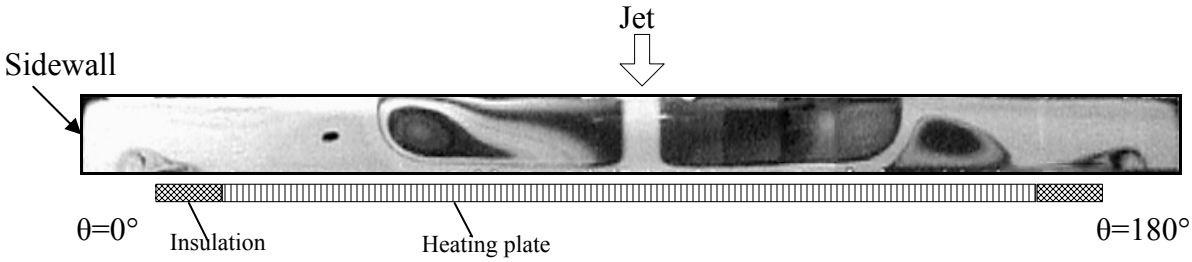

(a) Re_j=612 & D_j=10.0 mm

(b) Re_j=680 & D_j=10.0 mm

(c) Re_j=748 & D_j=10.0 mm

(d) Re_j=275 & D_j=22.1 mm

(e) Re_j=305 & D_j=22.1 mm

(f) Re_j=336 & D_j=22.1 mm

Fig. 3.6 Steady side view flow photos near the critical condition showing the flow near the onset of buoyancy-driven roll for Ra=1650 (ΔT=2.2℃) with (a) Re_j=612 & D_j=10.0 mm, (b) Re_j=680 & D_j=10.0 mm, (c) Re_j=748 & D_j=10.0 mm, (d) Re_j=275 & D_j=22.1 mm, (e) Re_j=305 & D_j=22.1 mm, and (f) Re_j=336 & D_j=22.1 mm.

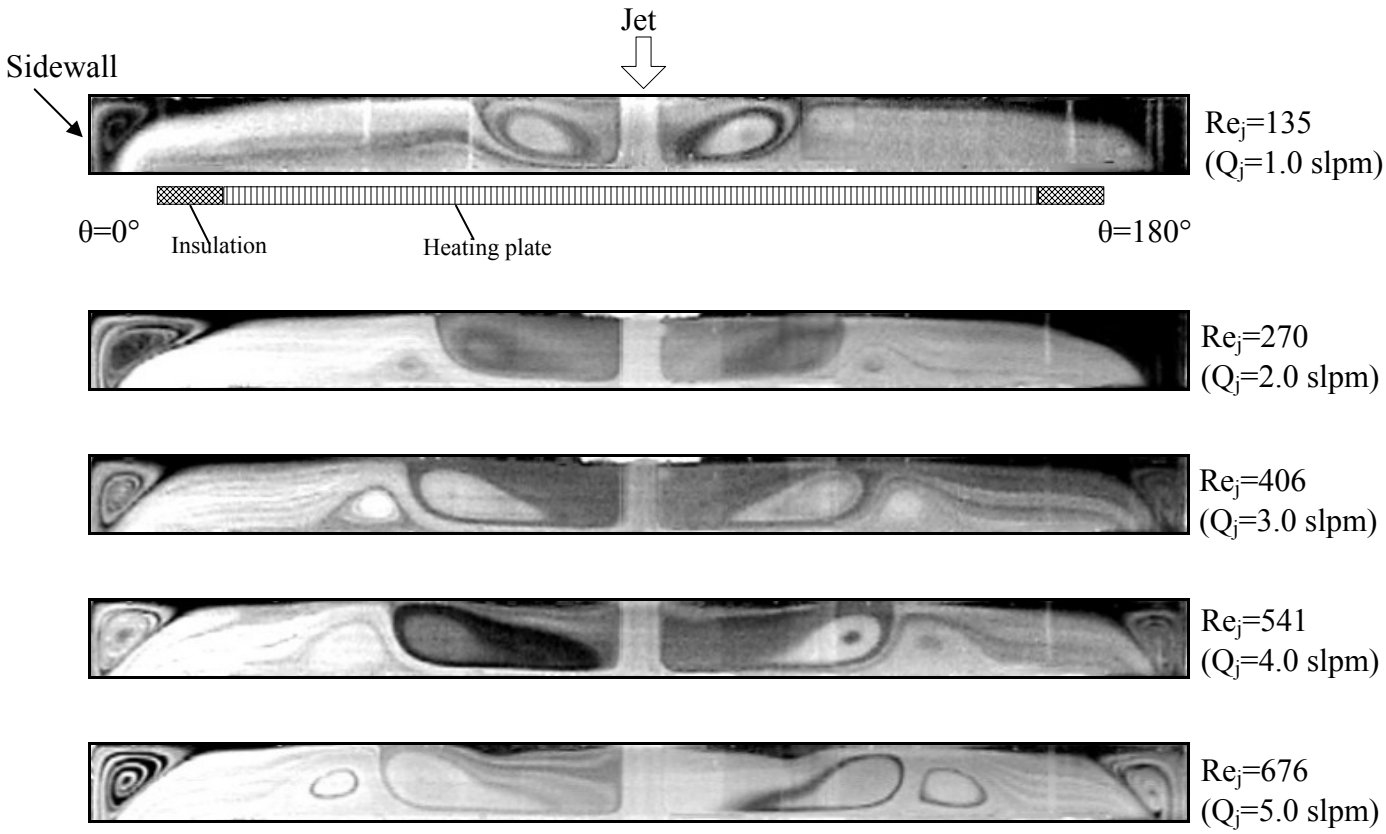

(a) D_j=10.0 mm

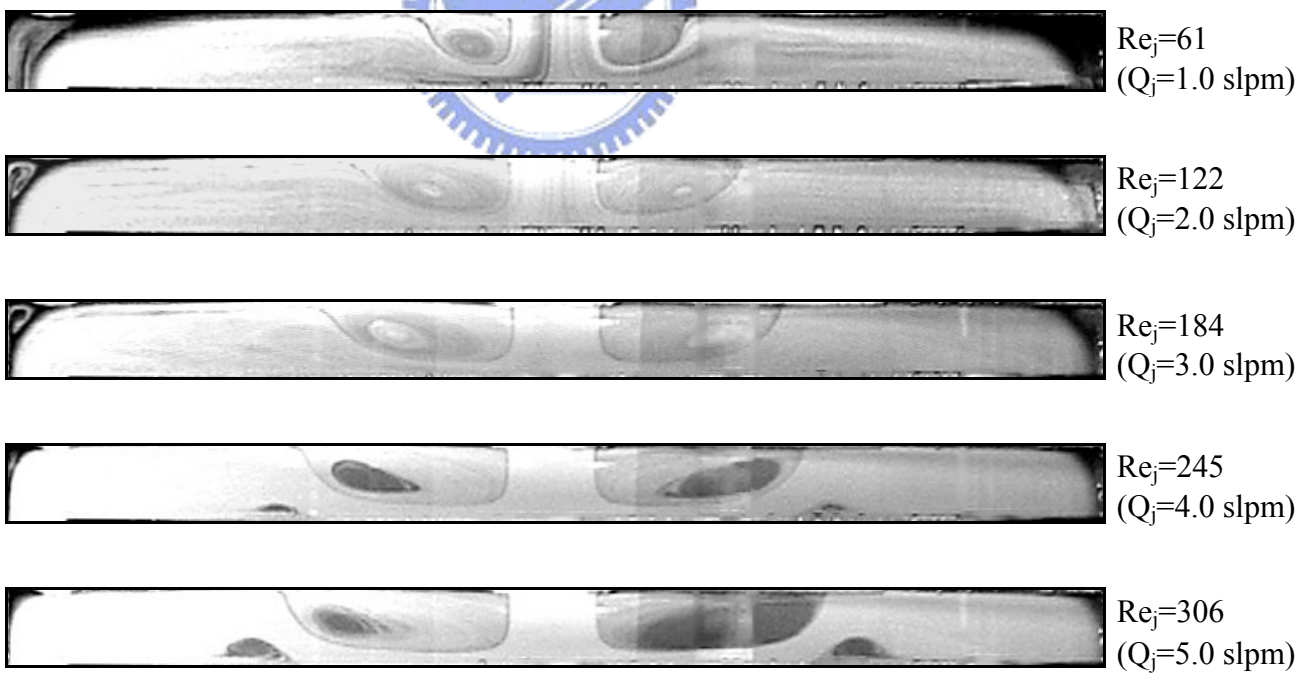

(b) D_j=22.1 mm

Fig. 3.7 Steady side view flow photos taken at the cross plane θ=0° & 180° for various jet Reynolds numbers at Ra=0 (ΔT=0℃) for D_j= (a) 10.0 mm and (b) 22.1 mm.

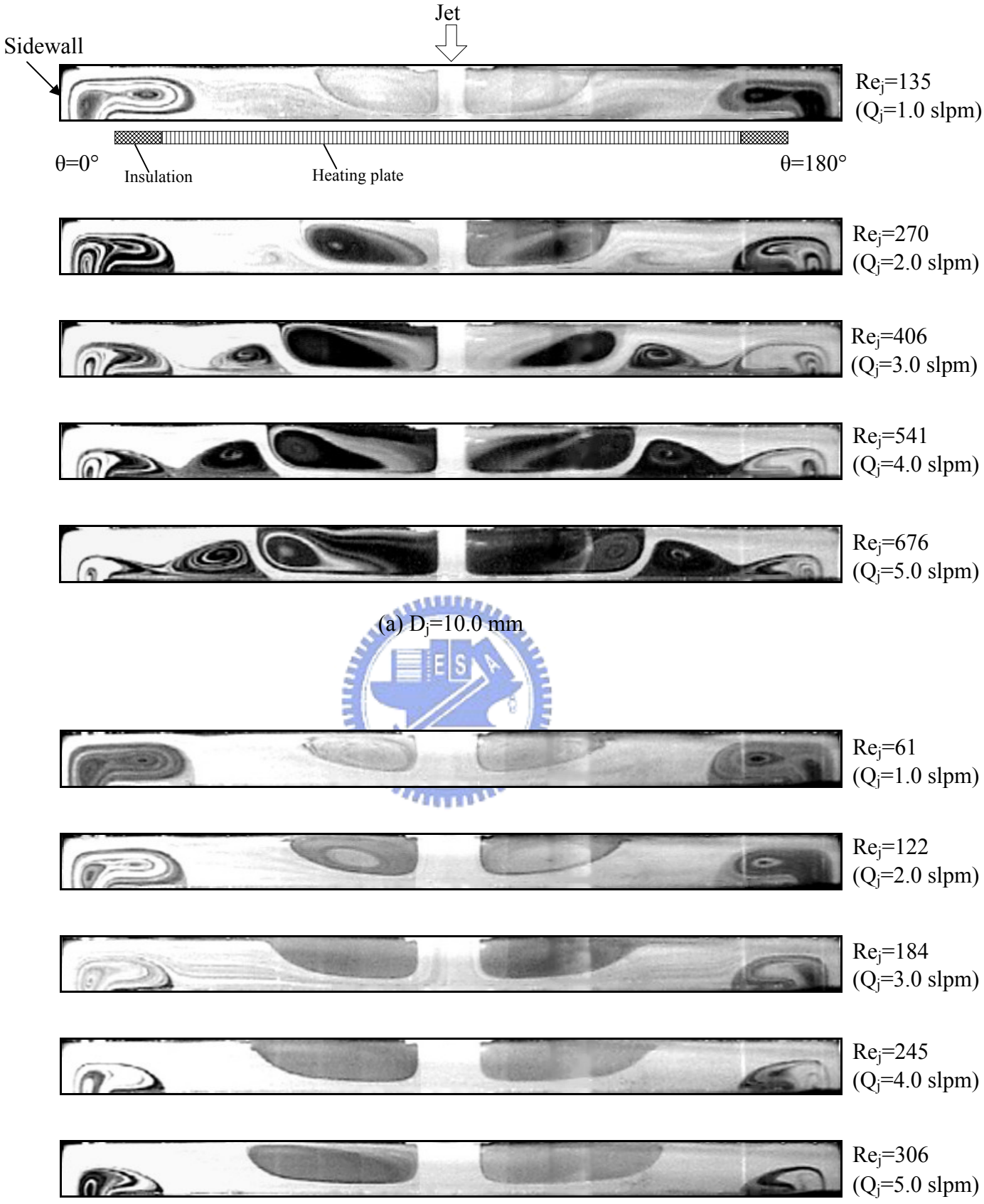

Fig. 3.8 Steady side view flow photos taken at the cross plane θ=0° & 180° for various jet Reynolds numbers at Ra=3,760 (ΔT=5.0℃) for D$_j$= (a) 10.0 mm and (b) 22.1 mm.

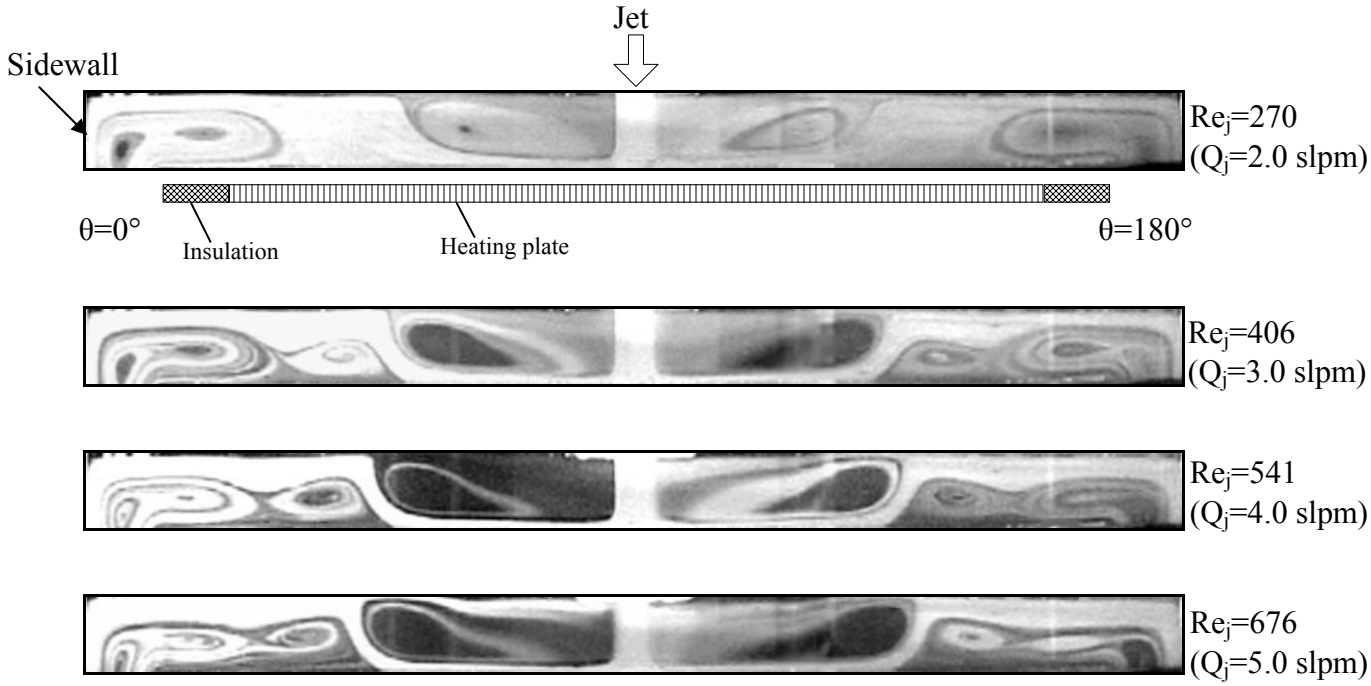

(a) D_j=10.0 mm

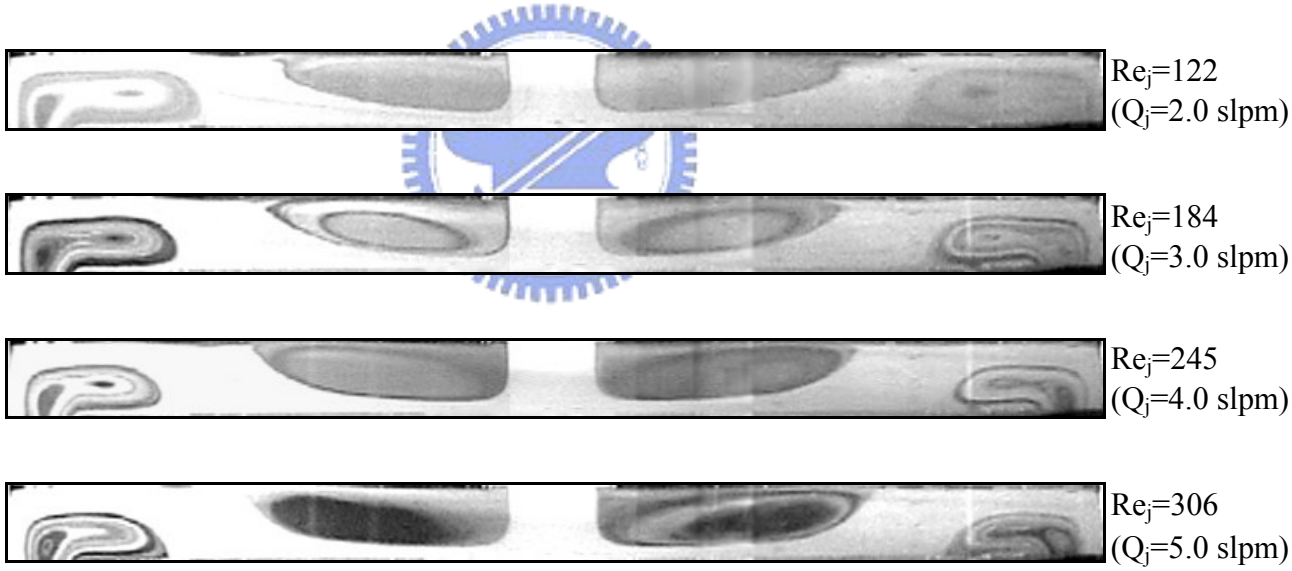

(b) D_j=22.1 mm

Fig. 3.9 Steady side view flow photos taken at the cross plane θ=0° & 180° for various jet Reynolds numbers at Ra=7,520 (ΔT=10.0℃) for D_j= (a) 10.0 mm and (b) 22.1 mm.

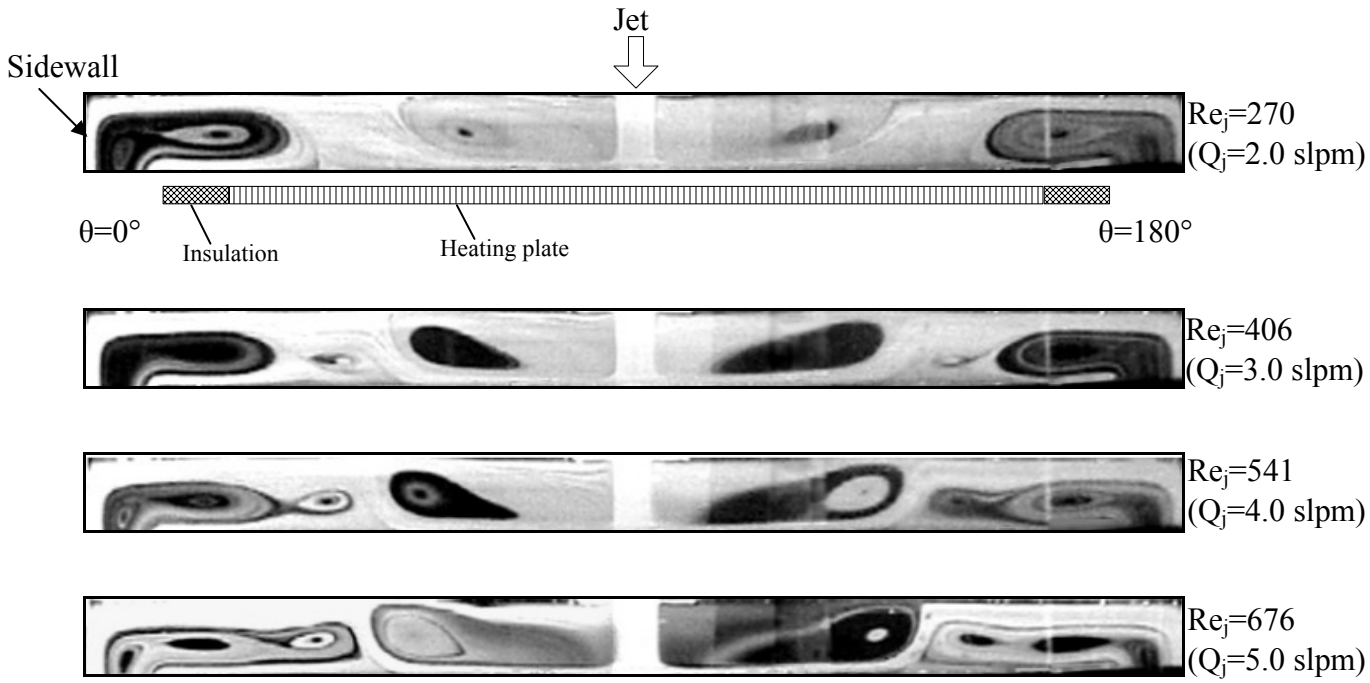

(a) D_j=10.0 mm

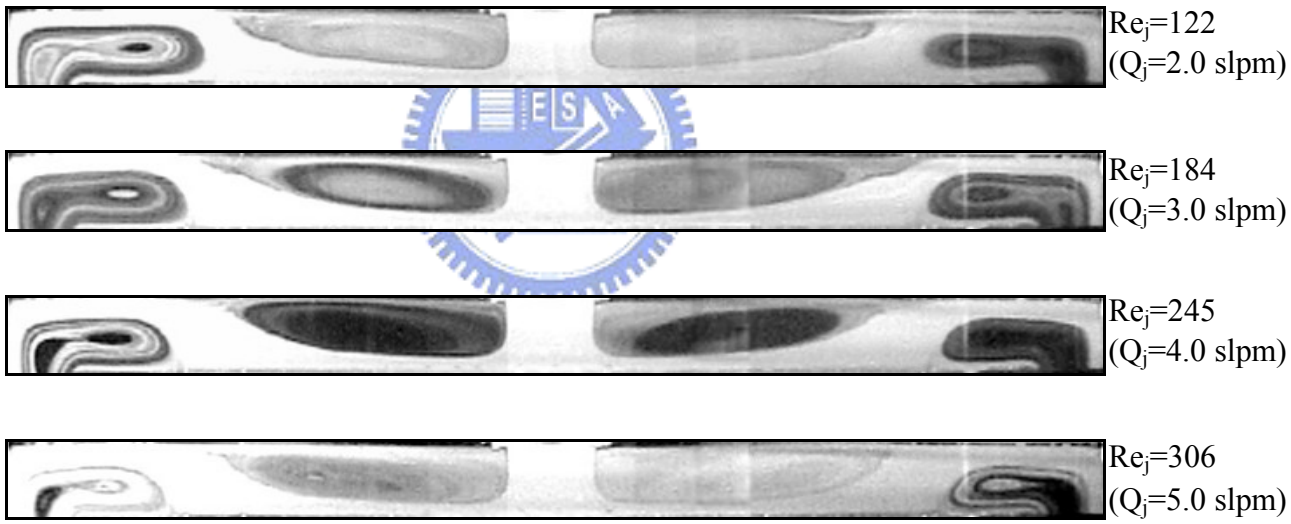

(b) D_j=22.1 mm

Fig. 3.10 Steady side view flow photos taken at the cross plane θ=0° & 180° for various jet Reynolds numbers at Ra=11,270 (ΔT=15.0℃) for D_j= (a) 10.0 mm and (b) 22.1 mm.

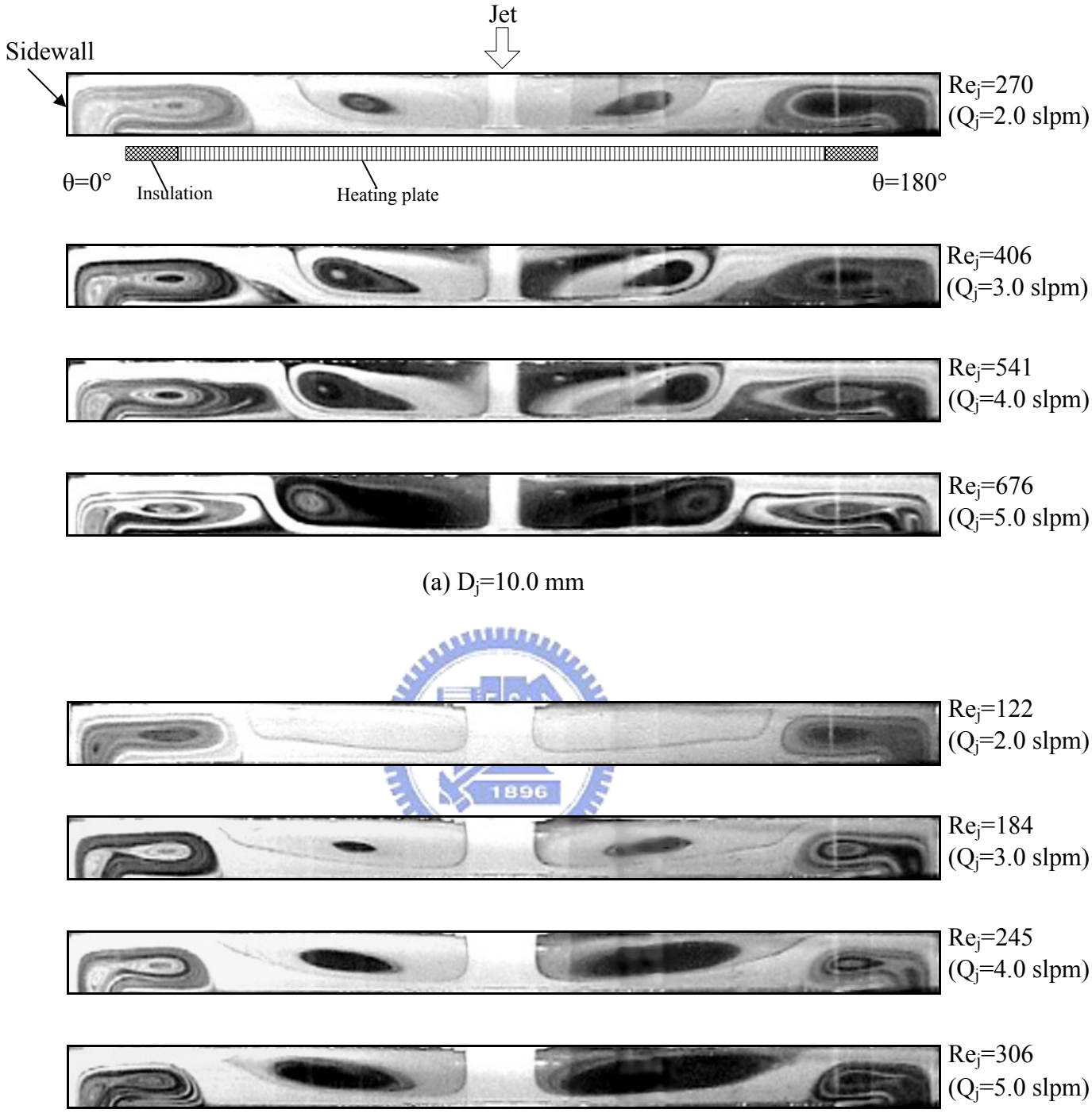

(a) D_j=10.0 mm

(b) D_j=22.1 mm

Fig. 3.11 Steady side view flow photos taken at the cross plane θ=0° & 180° for various jet Reynolds numbers at Ra=15,030 (ΔT=20.0℃) for D_j= (a) 10.0 mm and (b) 22.1 mm.

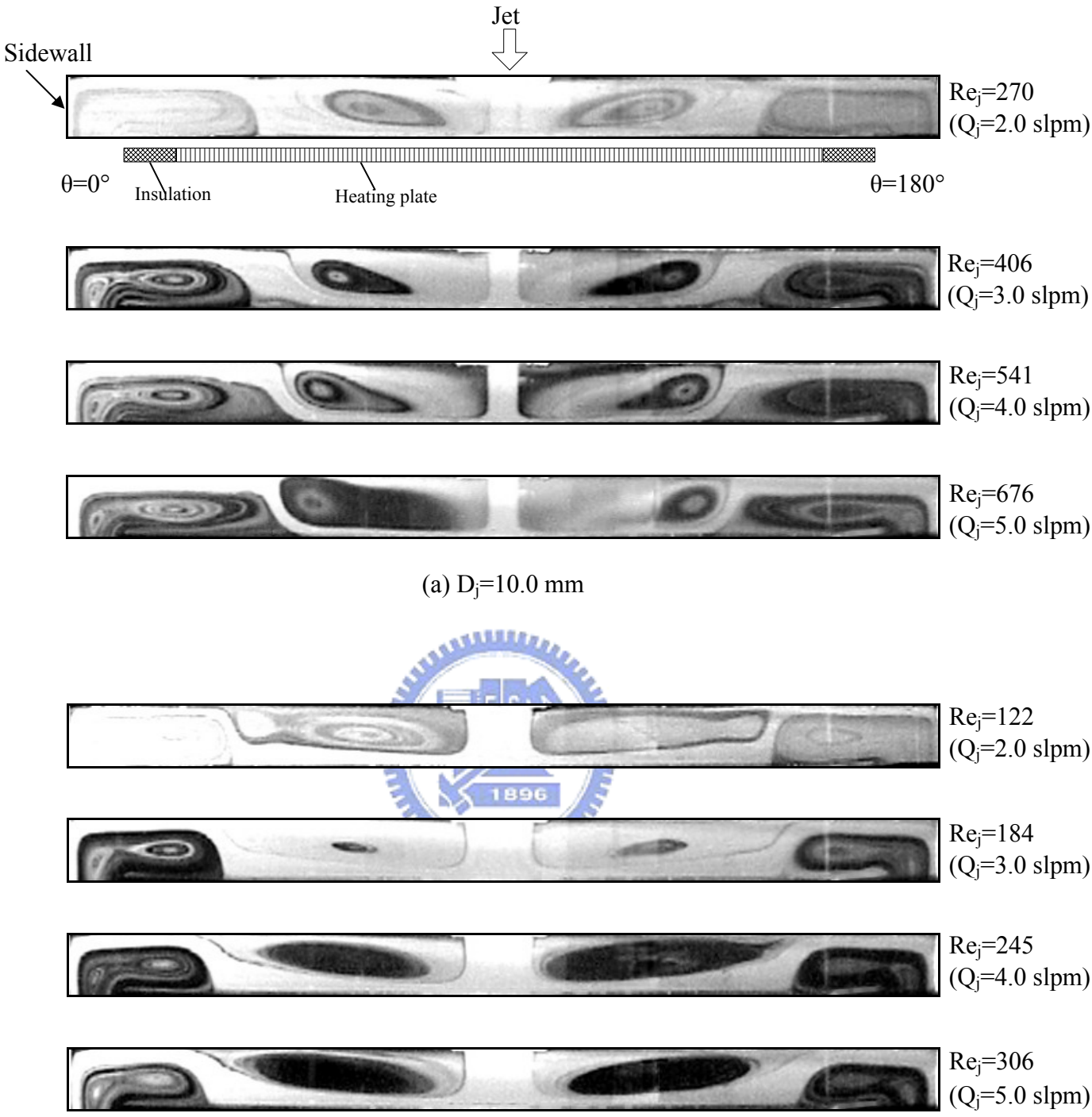

(a) D_j=10.0 mm

(b) D_j=22.1 mm

Fig. 3.12 Steady side view flow photos taken at the cross plane θ=0° & 180° for various jet Reynolds numbers at Ra=18,790 (ΔT=25.0℃) for D_j= (a) 10.0 mm and (b) 22.1 mm.

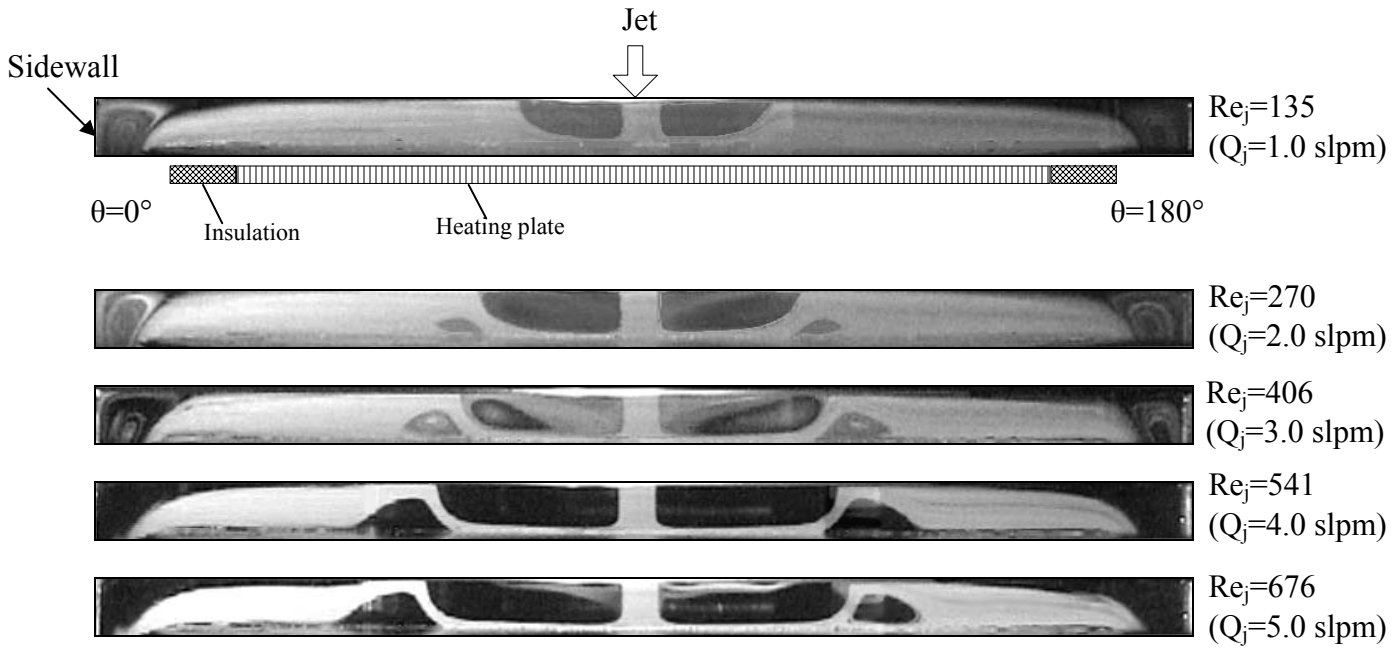

(a) D_j=10.0 mm & Ra=0

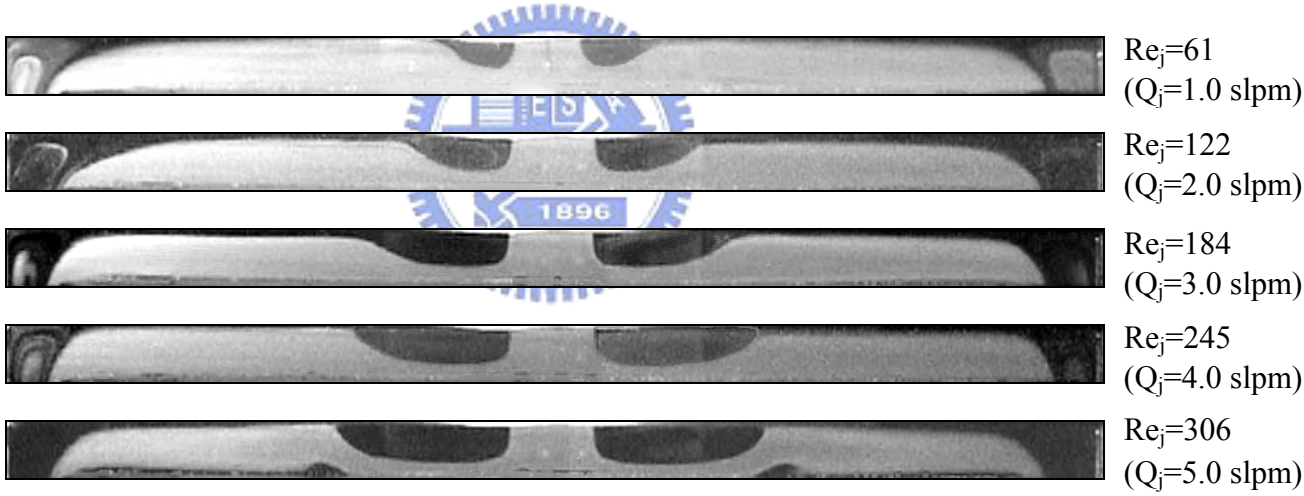

(b) D_j=22.1 mm & Ra=0

Fig. 3.13 Steady side view flow photos taken at the cross plane θ=0° & 180° for various jet Reynolds numbers at H=15.0 mm & Ra=0 (ΔT=0℃) for D_j= (a) 10.0 mm and (b) 22.1 mm.

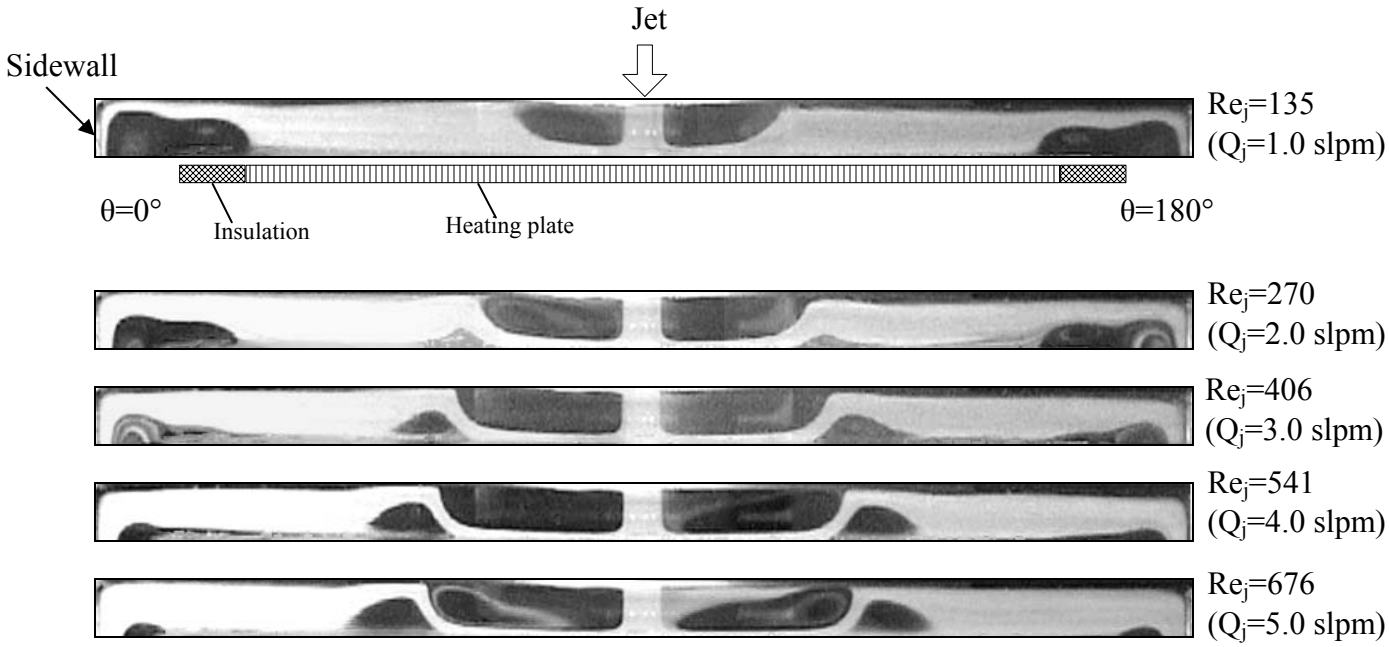

(a) D_j=10.0 mm & Ra=1,590

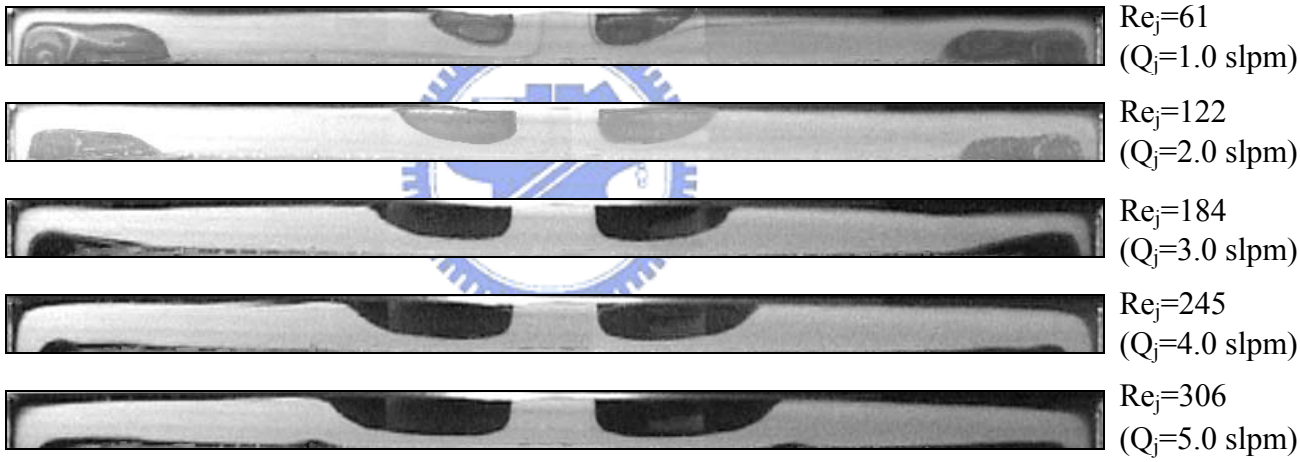

(b) D_j=22.1 mm & Ra=1,590

Fig. 3.14 Steady side view flow photos taken at the cross plane θ=0° & 180° for various jet Reynolds numbers at H=15.0 mm & Ra=1,590 (ΔT=5.0℃) for D_j= (a) 10.0 mm and (b) 22.1 mm.

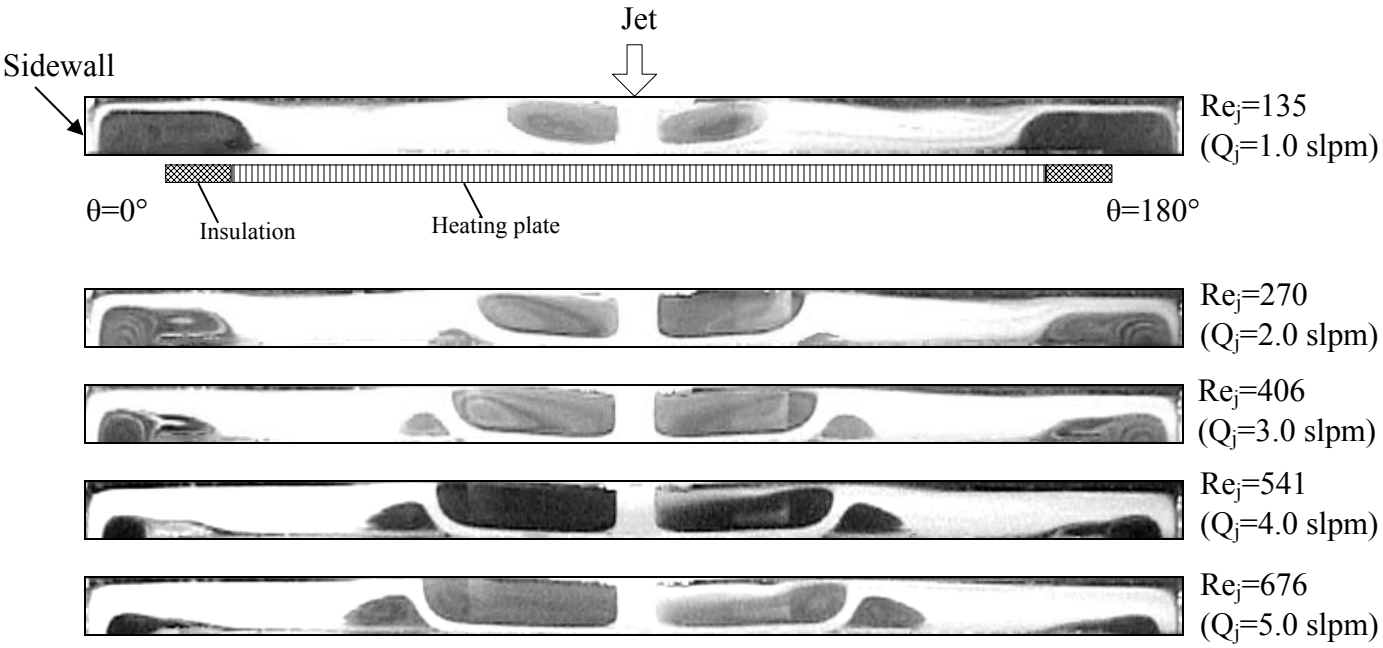

(a) D_j=10.0 mm & Ra=3,170

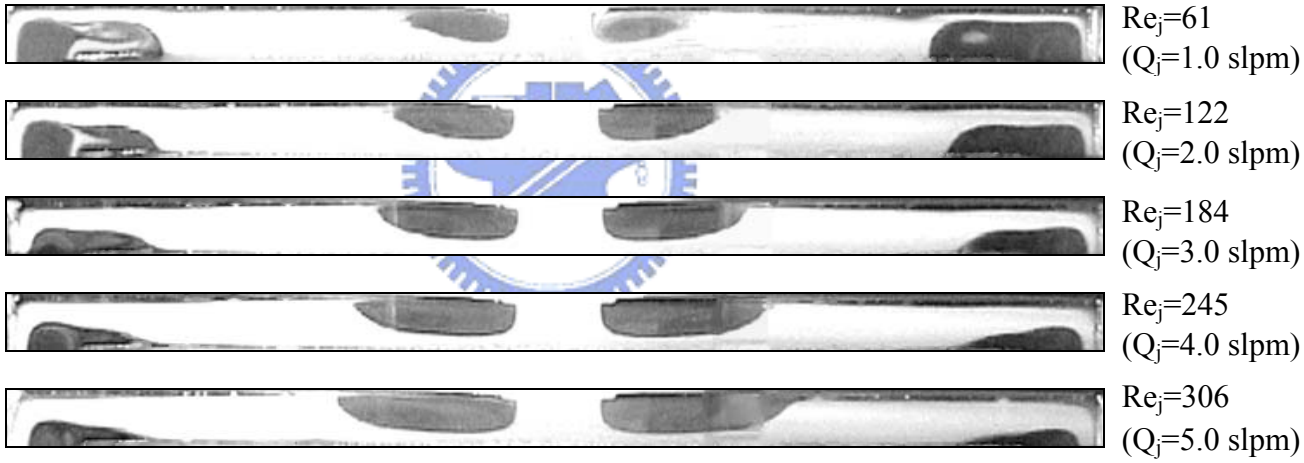

(b) D_j=22.1 mm & Ra=3,170

Fig. 3.15 Steady side view flow photos taken at the cross plane θ=0° & 180° for various jet Reynolds numbers at H=15.0 mm & Ra=3,170 (ΔT=10.0℃) for D_j= (a) 10.0 mm and (b) 22.1 mm.

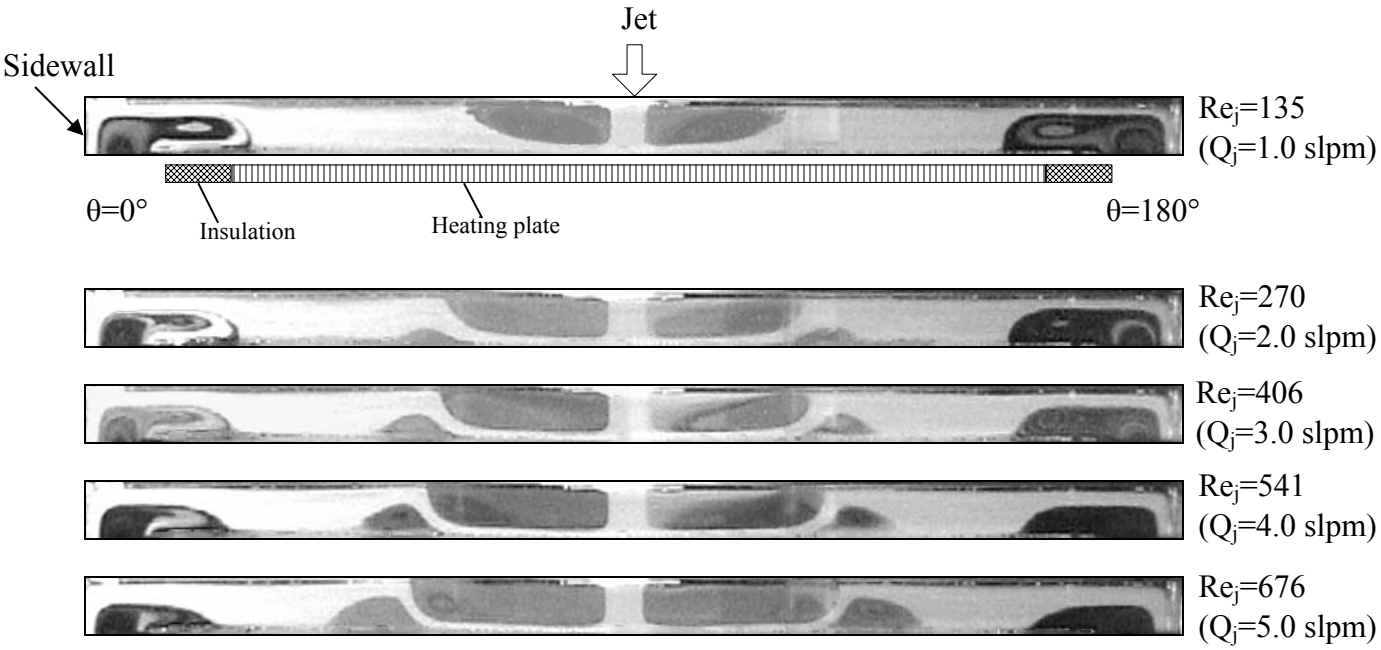

(a) D_j=10.0 mm & Ra=6,340

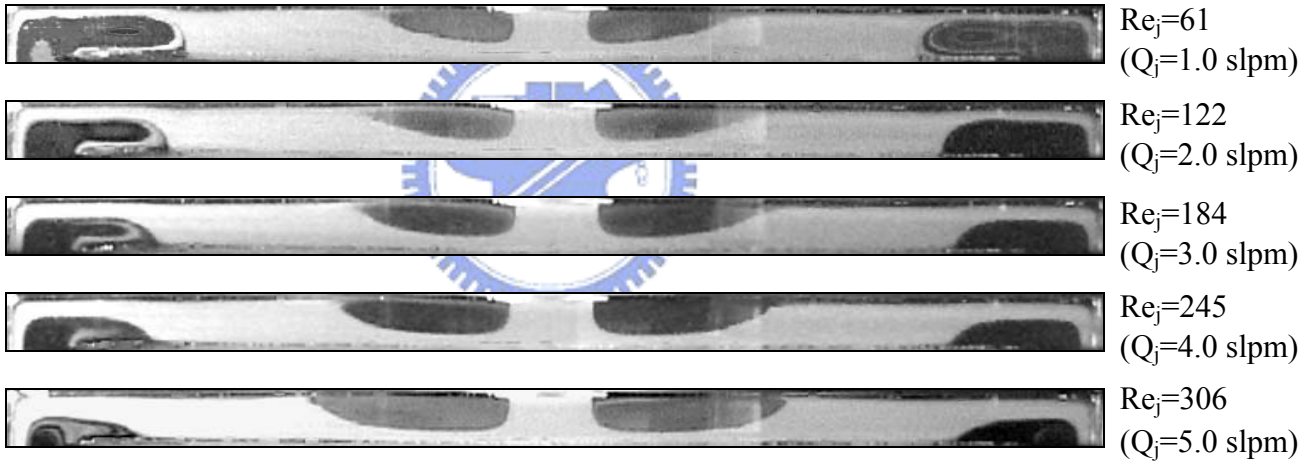

(b) D_j=22.1 mm & Ra=6,340

Fig. 3.16 Steady side view flow photos taken at the cross plane θ=0° & 180° for various jet Reynolds numbers at H=15.0 mm & Ra=6,340 (ΔT=20.0℃) for D_j= (a) 10.0 mm and (b) 22.1 mm.

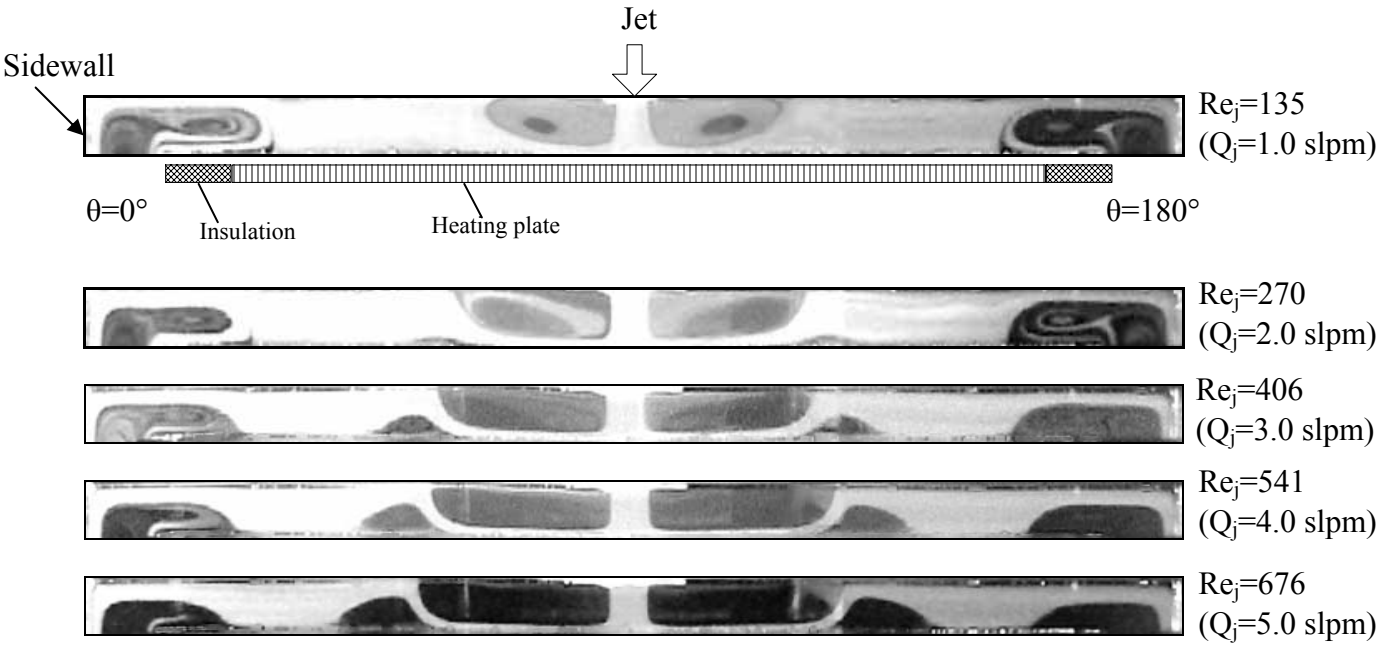

(a) D_j=10.0 mm & Ra=7,930

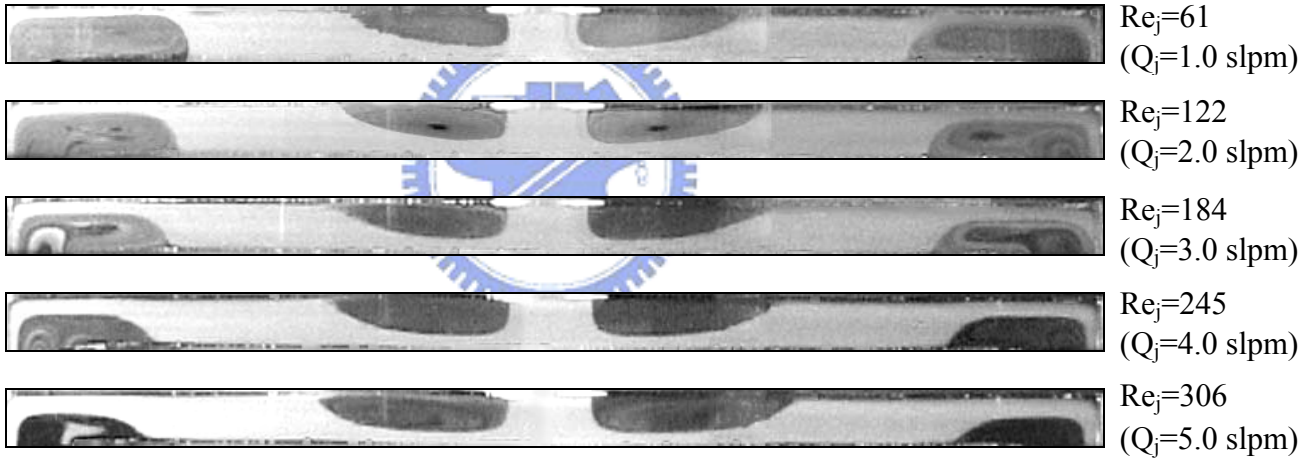

(b) D_j=22.1 mm & Ra=7,930

Fig. 3.17 Steady side view flow photos taken at the cross plane θ=0° & 180° for various jet Reynolds numbers at H=15.0 mm & Ra=7,930 (ΔT=25.0℃) for D_j= (a) 10.0 mm and (b) 22.1 mm.

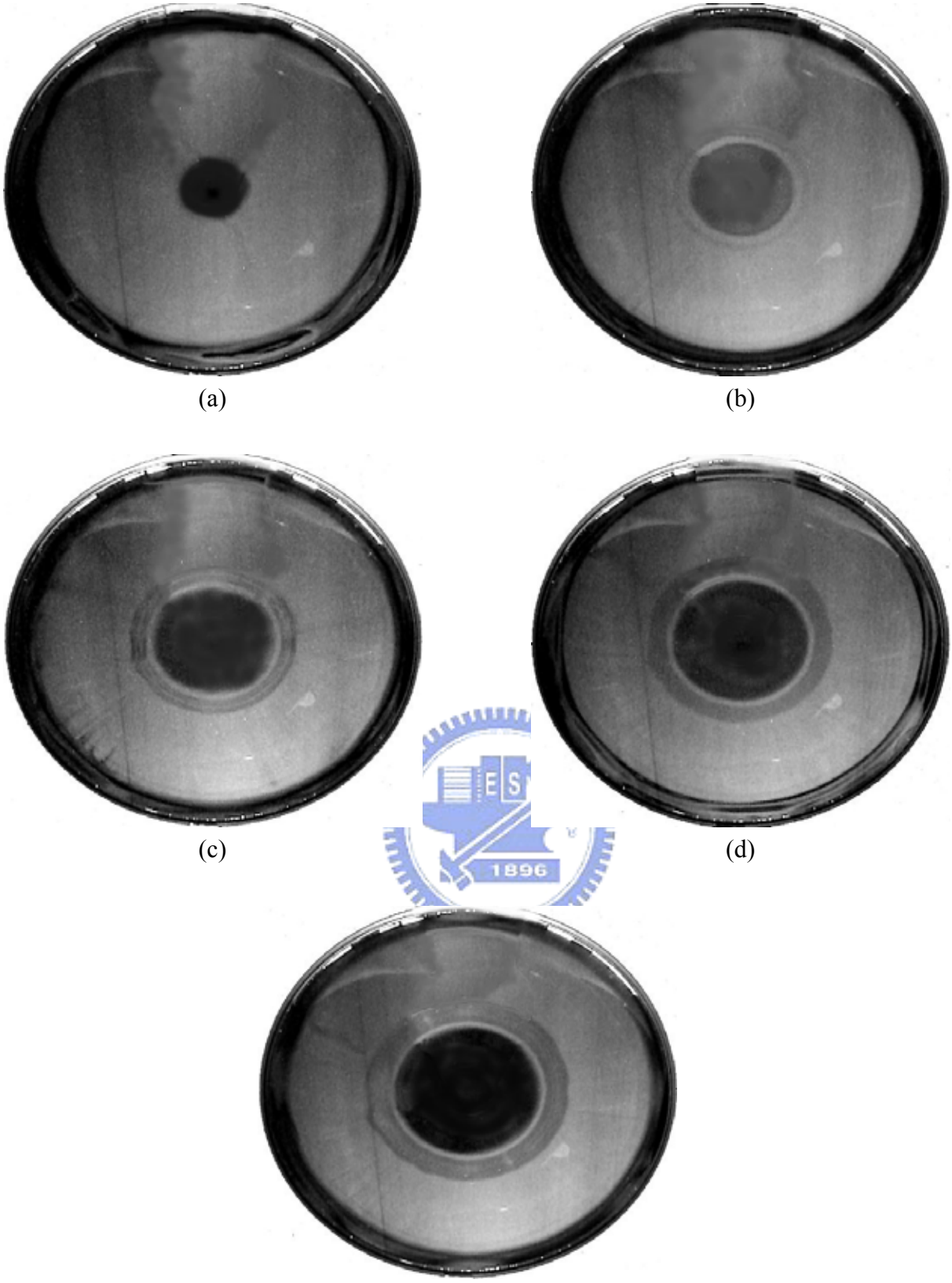

Fig. 3.18 Steady top view flow photos taken at the middle horizontal plane between the disk and chamber top with Ra=0 ($\Delta T=0$℃) & D_j=10.0 mm at H=15.0 mm for Re_j= (a) 135, (b) 270, (c) 406, (d) 541, and (e) 676.

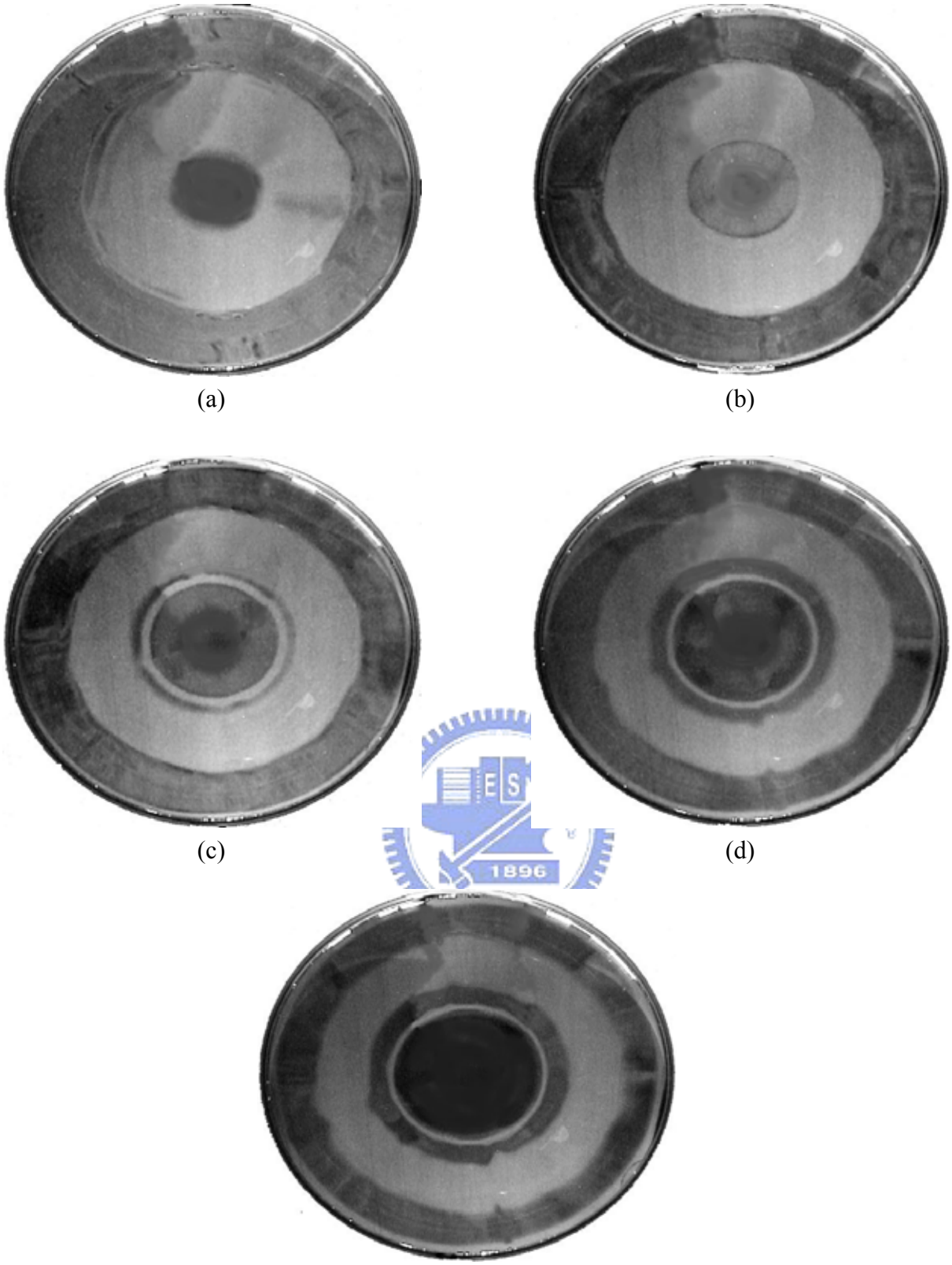

Fig. 3.19 Steady top view flow photos taken at the middle horizontal plane between the disk and chamber top with Ra=6,340 (ΔT=20.0℃) & D_j=10.0 mm at H=15.0 mm for Re_j= (a) 135, (b) 270, (c) 406, (d) 541, and (e) 676.

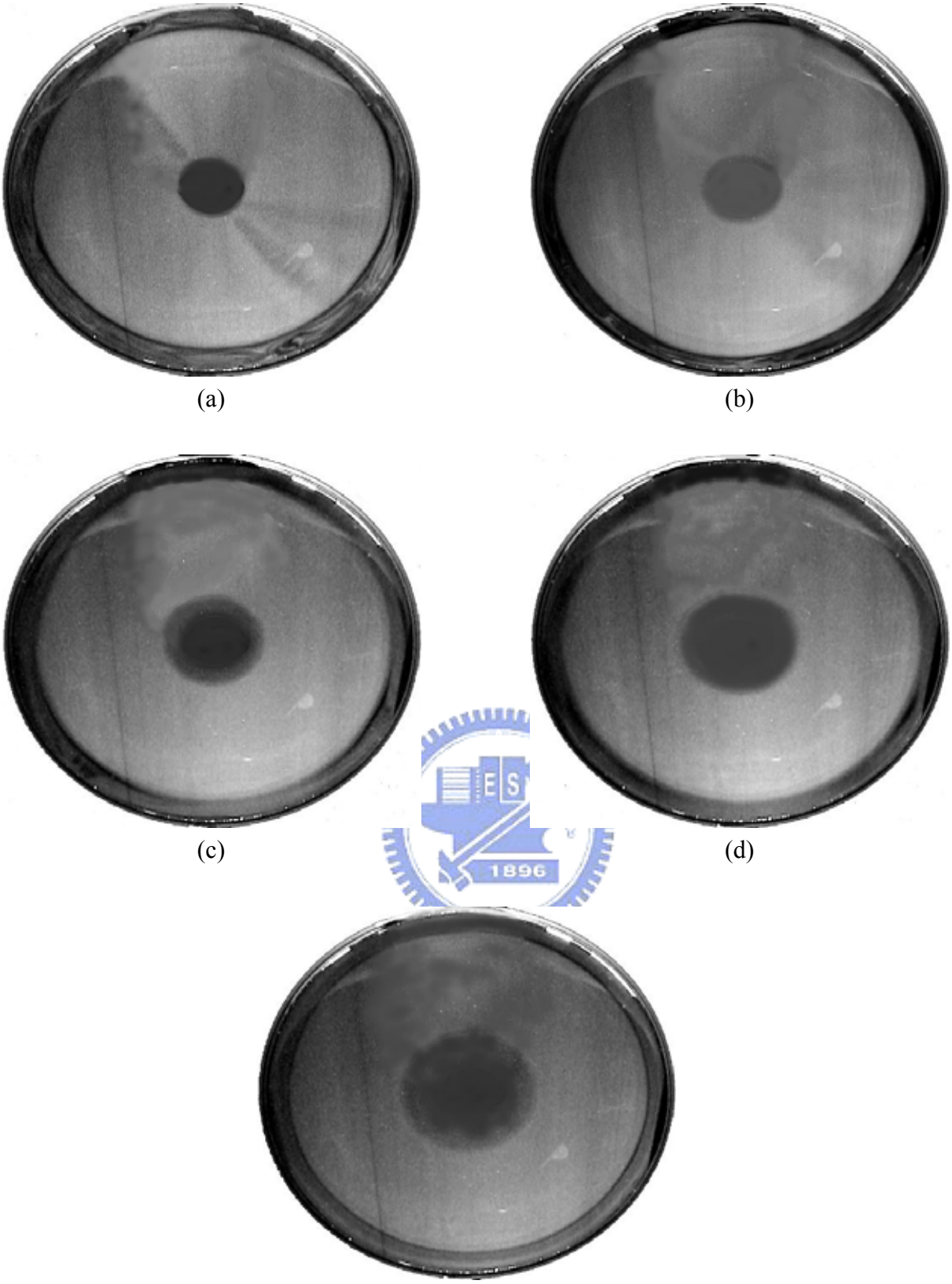

Fig. 3.20 Steady top view flow photos taken at the middle horizontal plane between the disk and chamber top with Ra=0 ($\Delta T=0^{\circ}C$) & D_j=22.1 mm at H=15.0 mm for Re_j= (a) 61, (b) 122, (c) 183, (d) 245, and (e) 306.

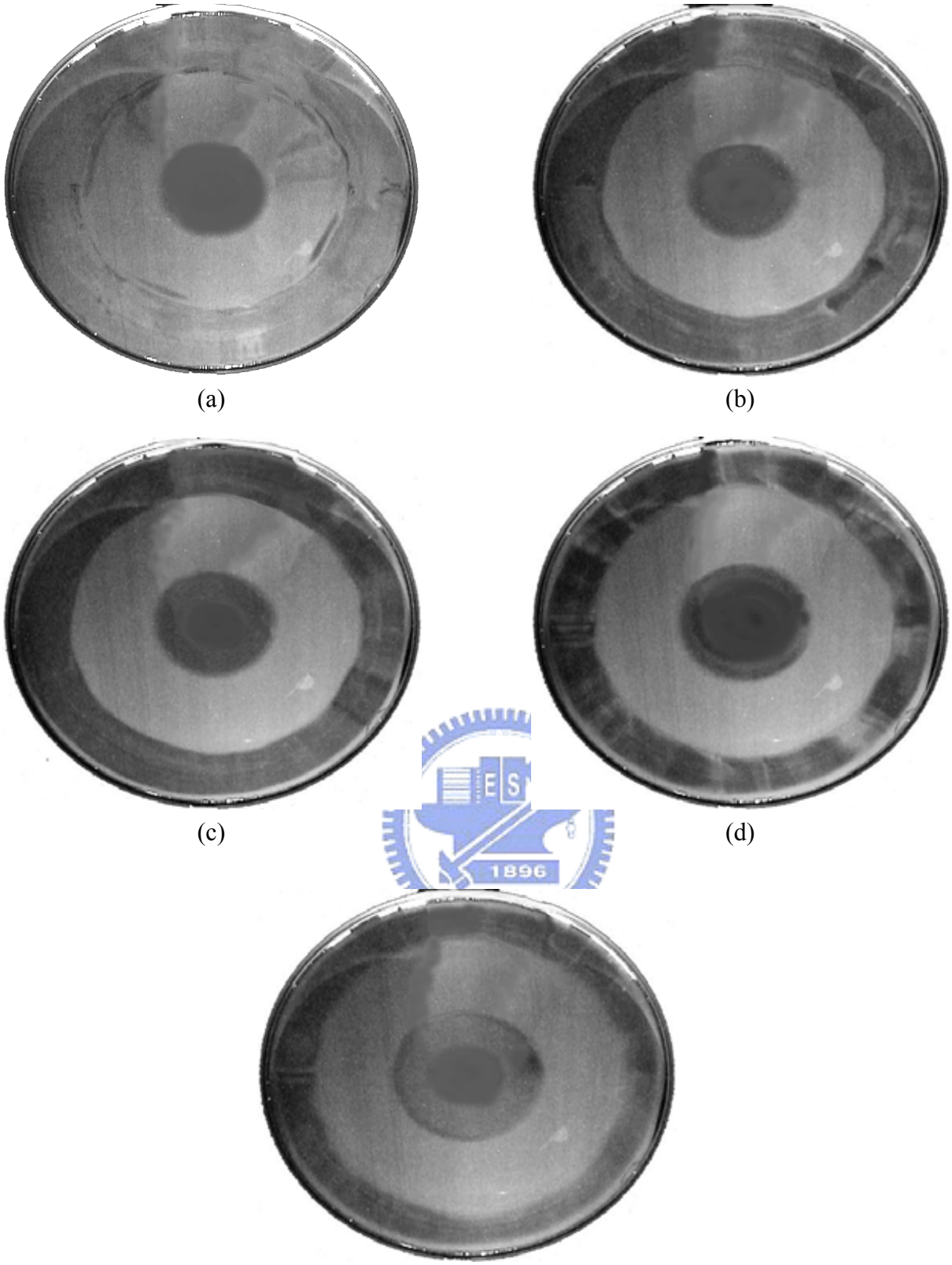

Fig. 3.21 Steady top view flow photos taken at the middle horizontal plane between the disk and chamber top with Ra=6,340 (ΔT=20.0℃) & D_j=22.1 mm at H=15.0 mm for Re_j= (a) 61, (b) 122, (c) 183, (d) 245, and (e) 306.

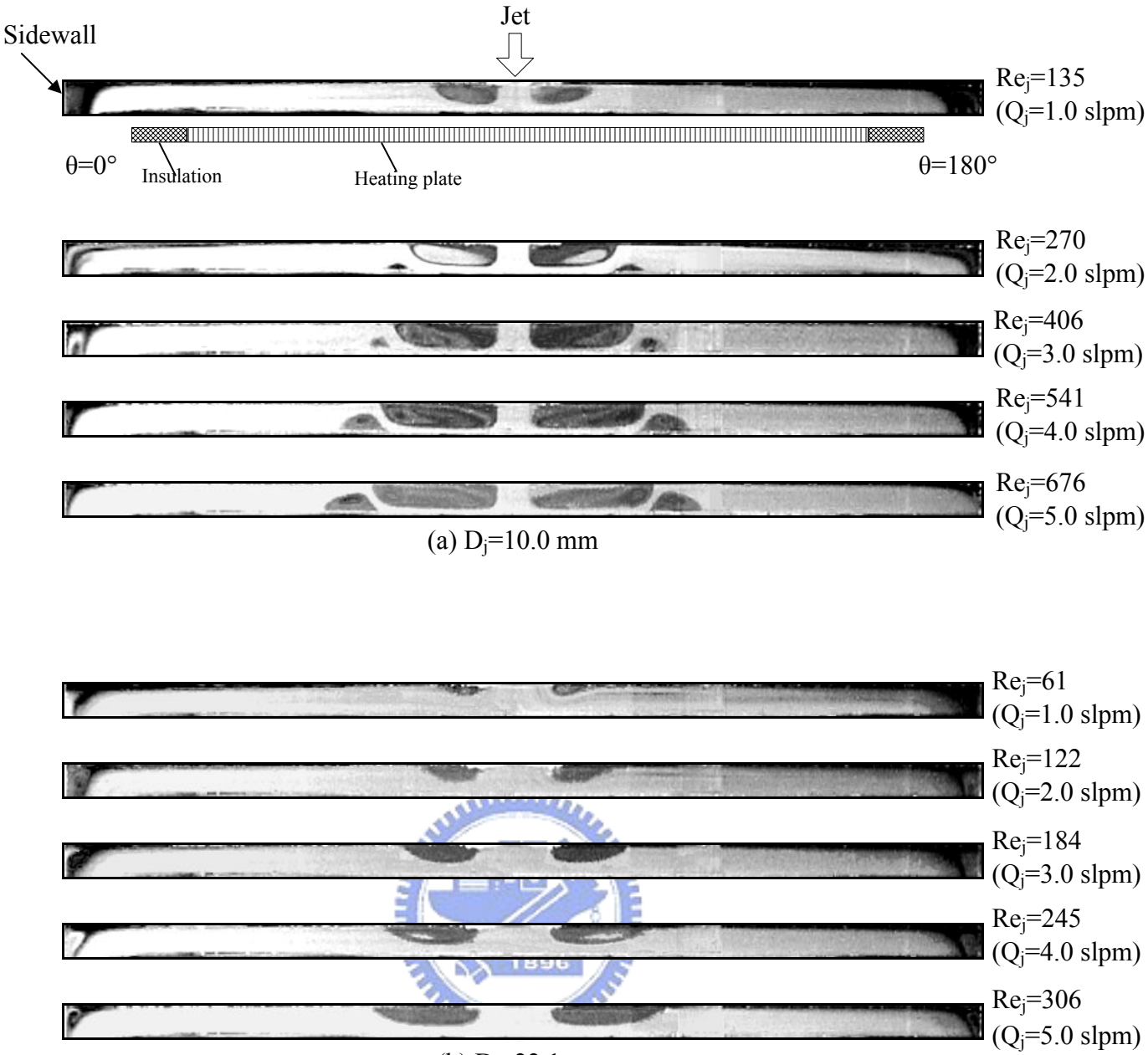

Fig. 3.22 Steady side view flow photos taken at the cross plane θ=0° & 180° for various jet Reynolds numbers at H=10.0 mm and Ra=0 (ΔT=0℃) for D$_j$= (a) 10.0 mm and (b) 22.1 mm.

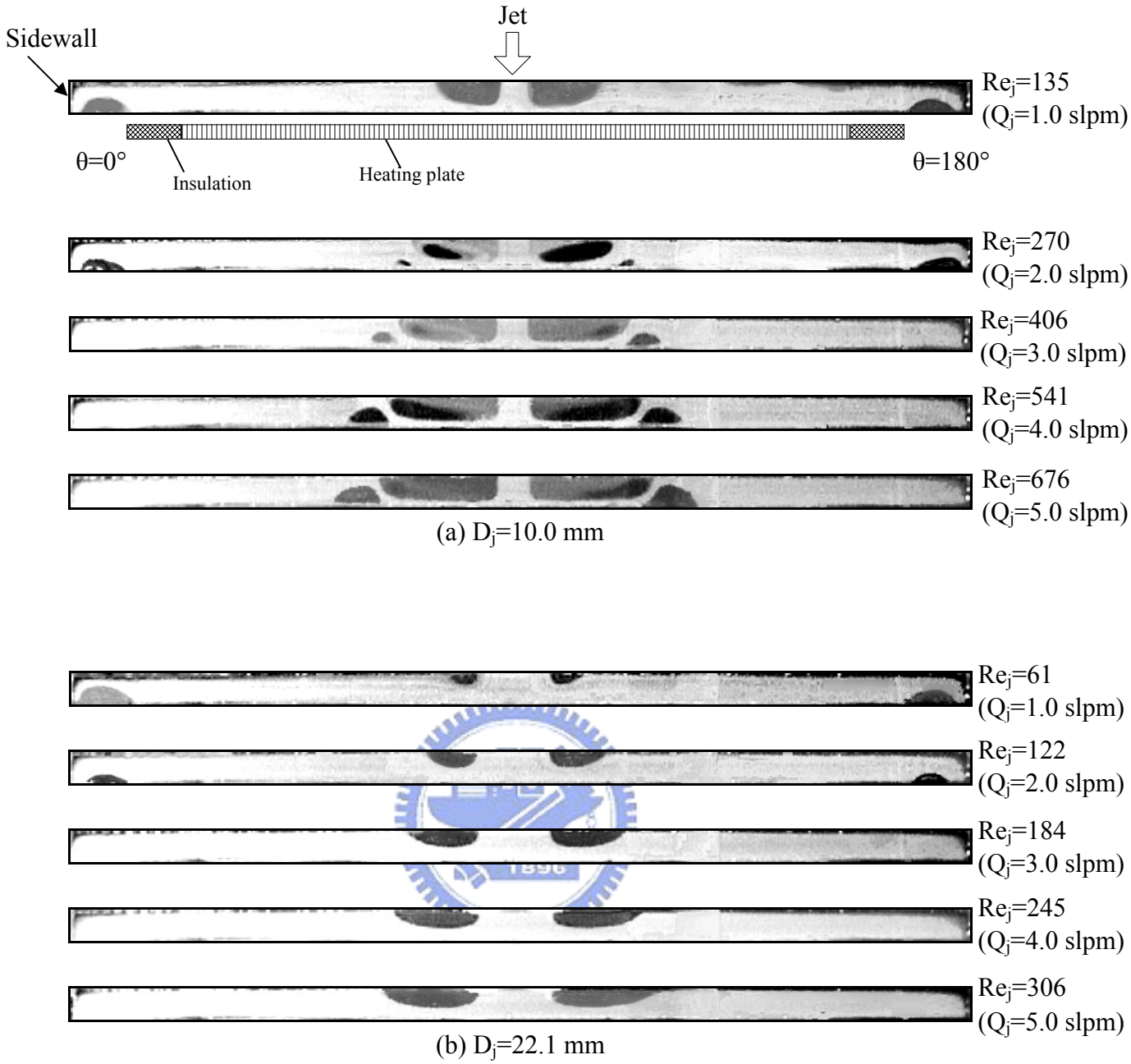

Fig. 3.23 Steady side view flow photos taken at the cross plane θ=0° & 180° for various jet Reynolds numbers at H=10.0 mm and Ra=470 (ΔT=5.0℃) for D$_j$= (a) 10.0 mm and (b) 22.1 mm.

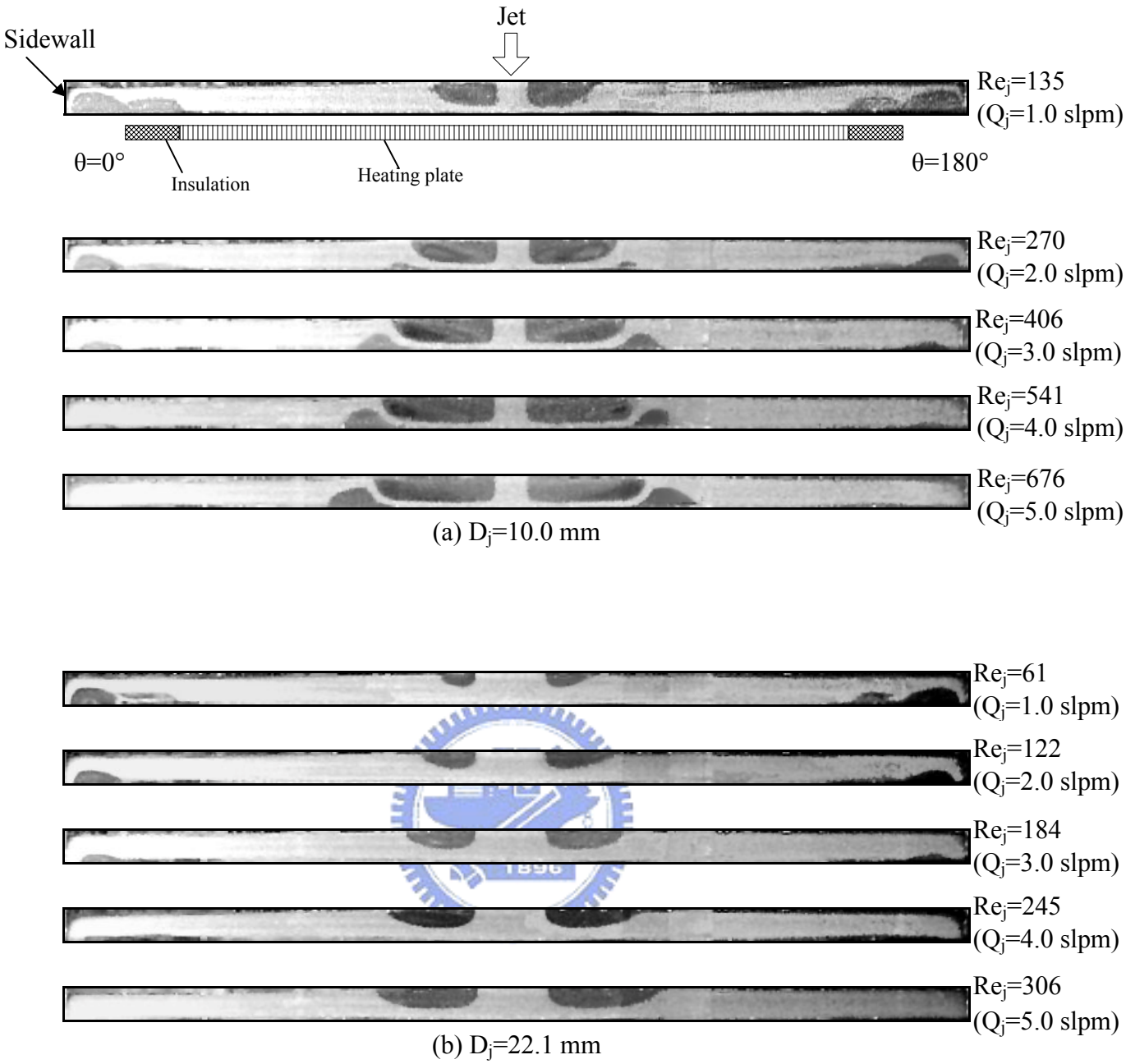

Fig. 3.24 Steady side view flow photos taken at the cross plane θ=0° & 180° for various jet Reynolds numbers at H=10.0 mm and Ra=940 (ΔT=10.0℃) for D$_j$= (a) 10.0 mm and (b) 22.1 mm.

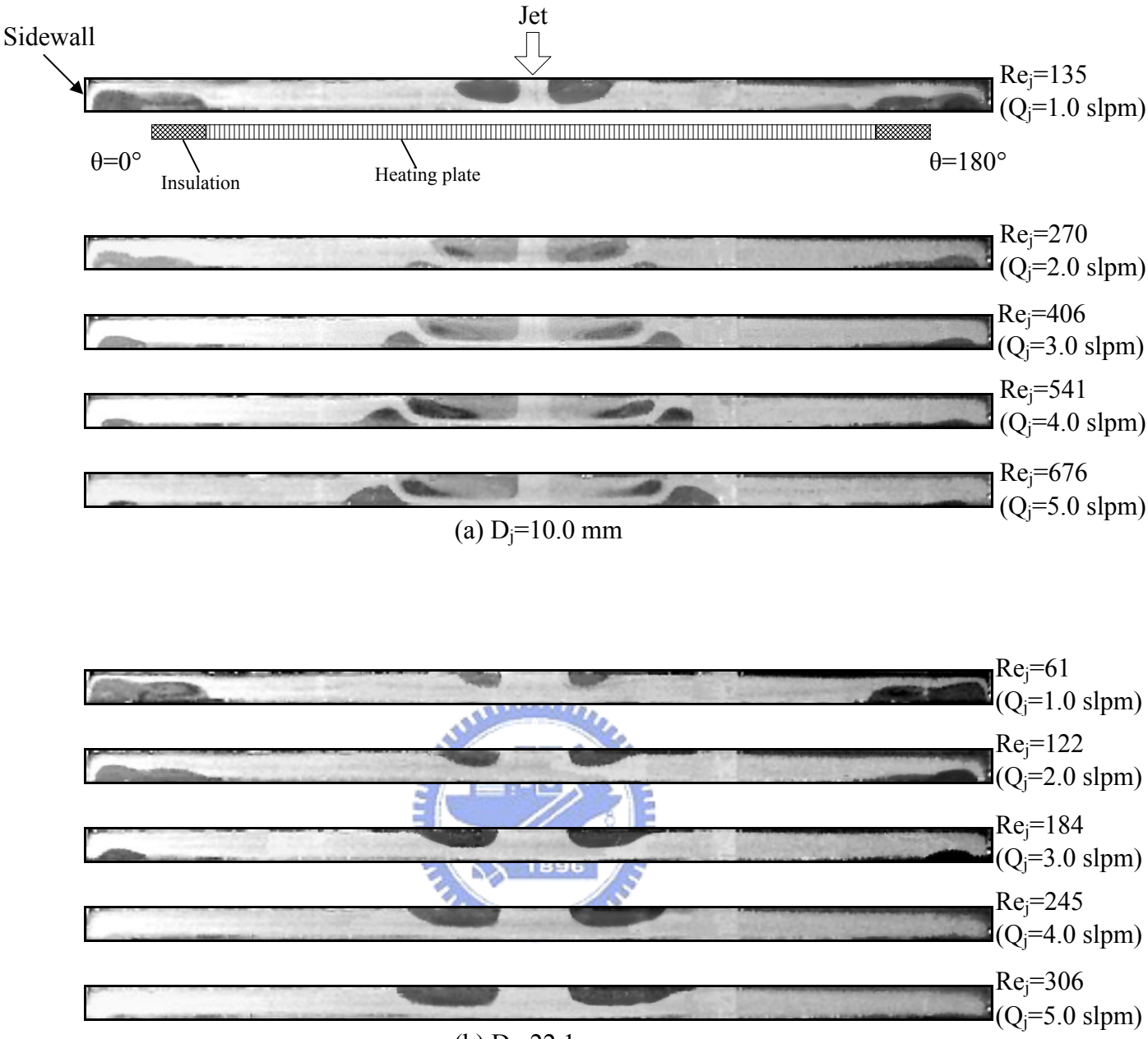

Fig. 3.25 Steady side view flow photos taken at the cross plane θ=0° & 180° for various jet Reynolds numbers at H=10.0 mm and Ra=1,410 (ΔT=15.0℃) for D$_j$= (a) 10.0 mm and (b) 22.1 mm.

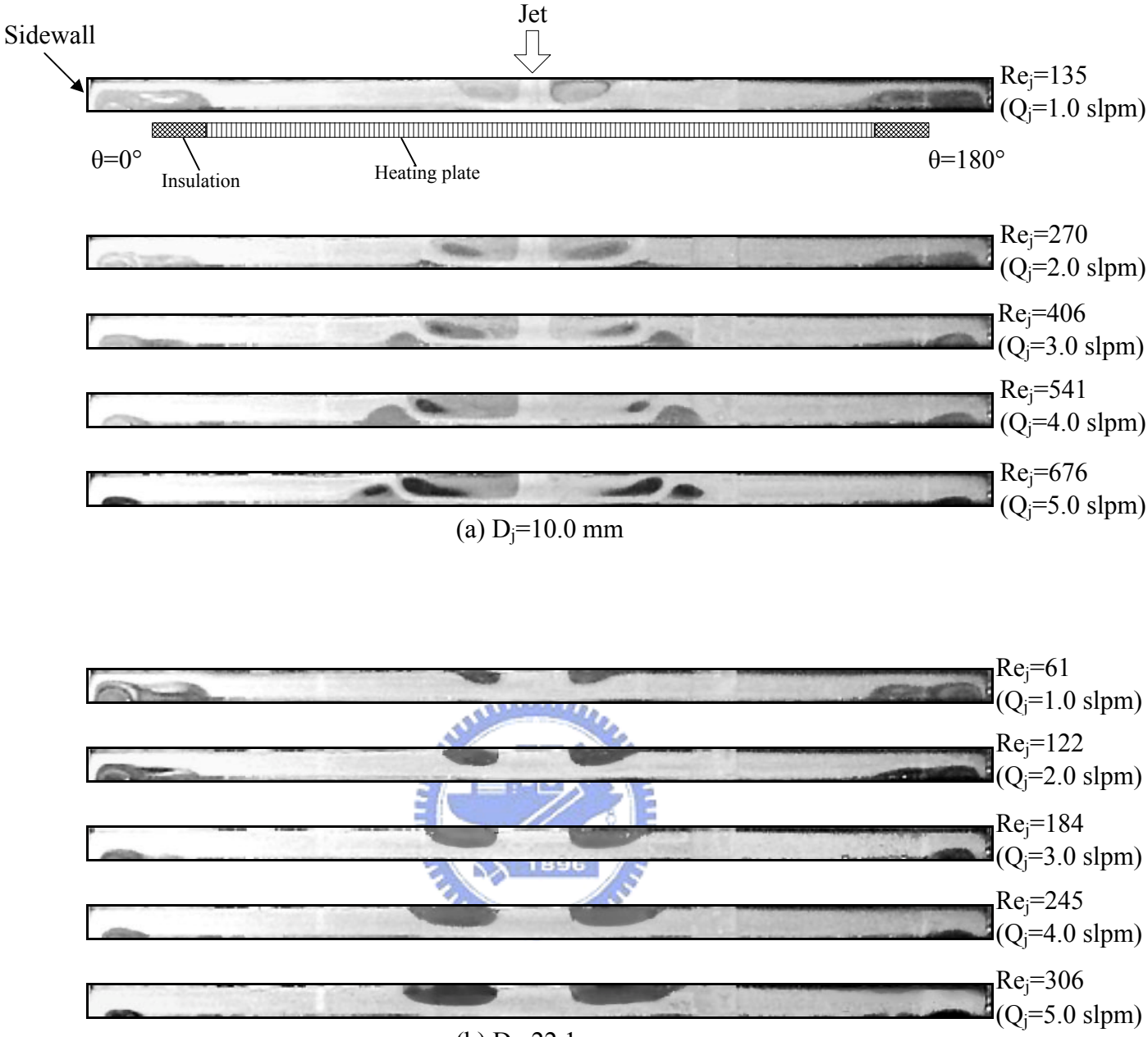

Fig. 3.26 Steady side view flow photos taken at the cross plane θ=0° & 180° for various jet Reynolds numbers at H=10.0 mm and Ra=1,880 (ΔT=20.0℃) for D$_j$= (a) 10.0 mm and (b) 22.1 mm.

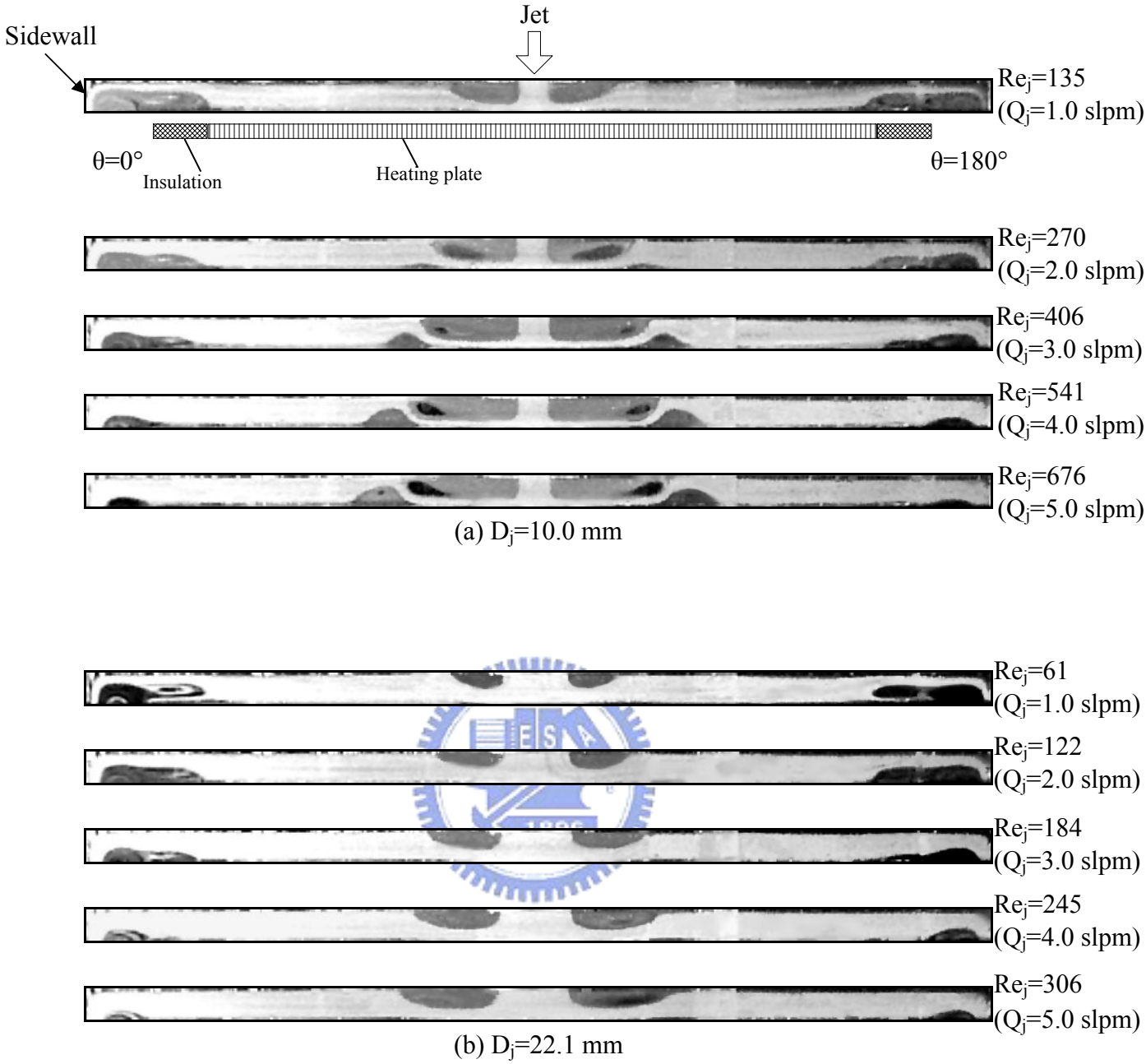

Fig. 3.27 Steady side view flow photos taken at the cross plane θ=0° & 180° for various jet Reynolds numbers at H=10.0 mm and Ra=2,350 (ΔT=25.0℃) for D$_j$= (a) 10.0 mm and (b) 22.1 mm.

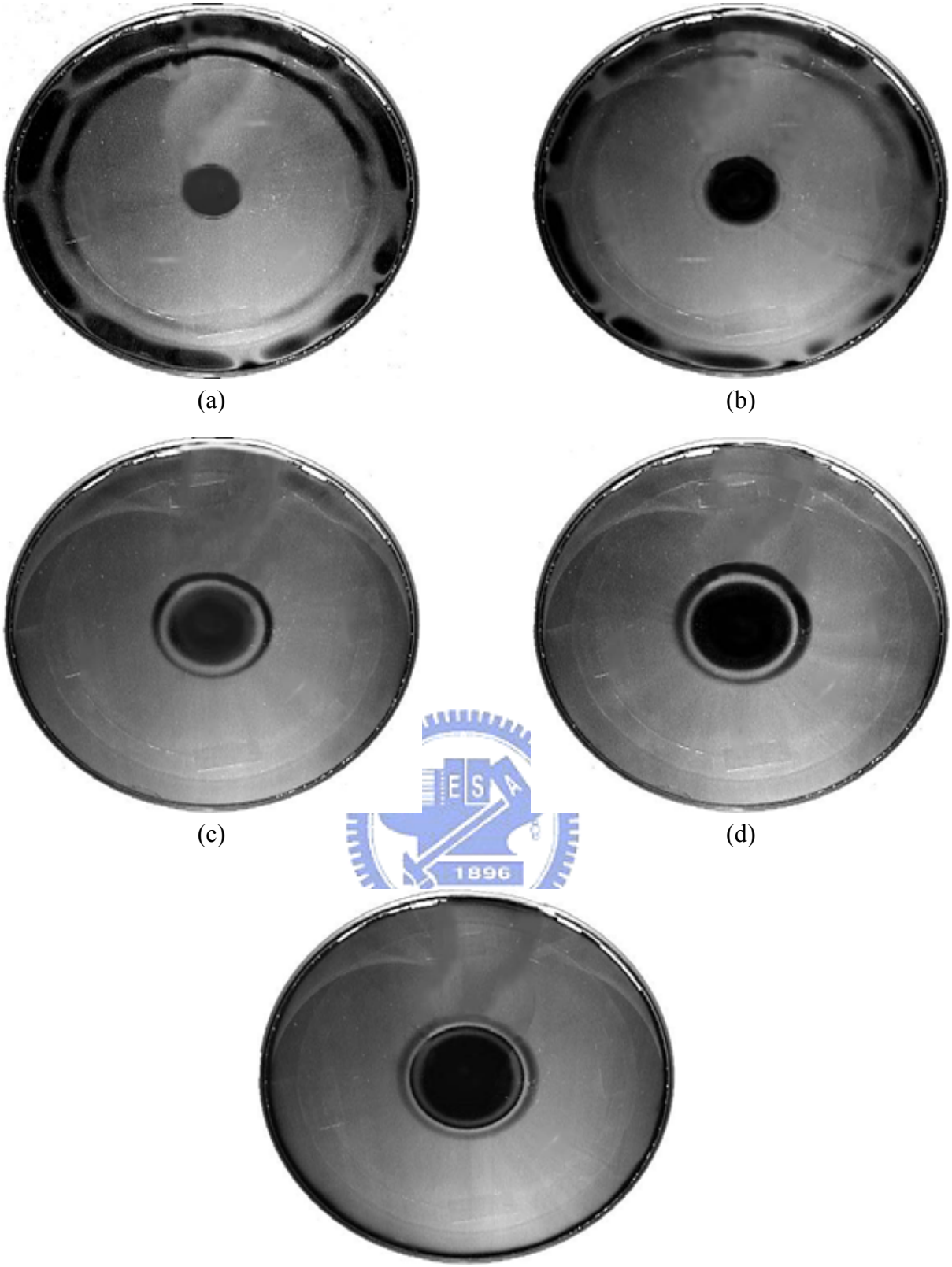

Fig. 3.28 Top view flow photos taken at the middle horizontal plane between the disk and chamber top with Ra =940 (ΔT=10.0℃) and D_j=10.0 mm at H=10.0 mm for Re_j= (a) 135, (b) 270, (c) 406, (d) 541, and (e) 676.

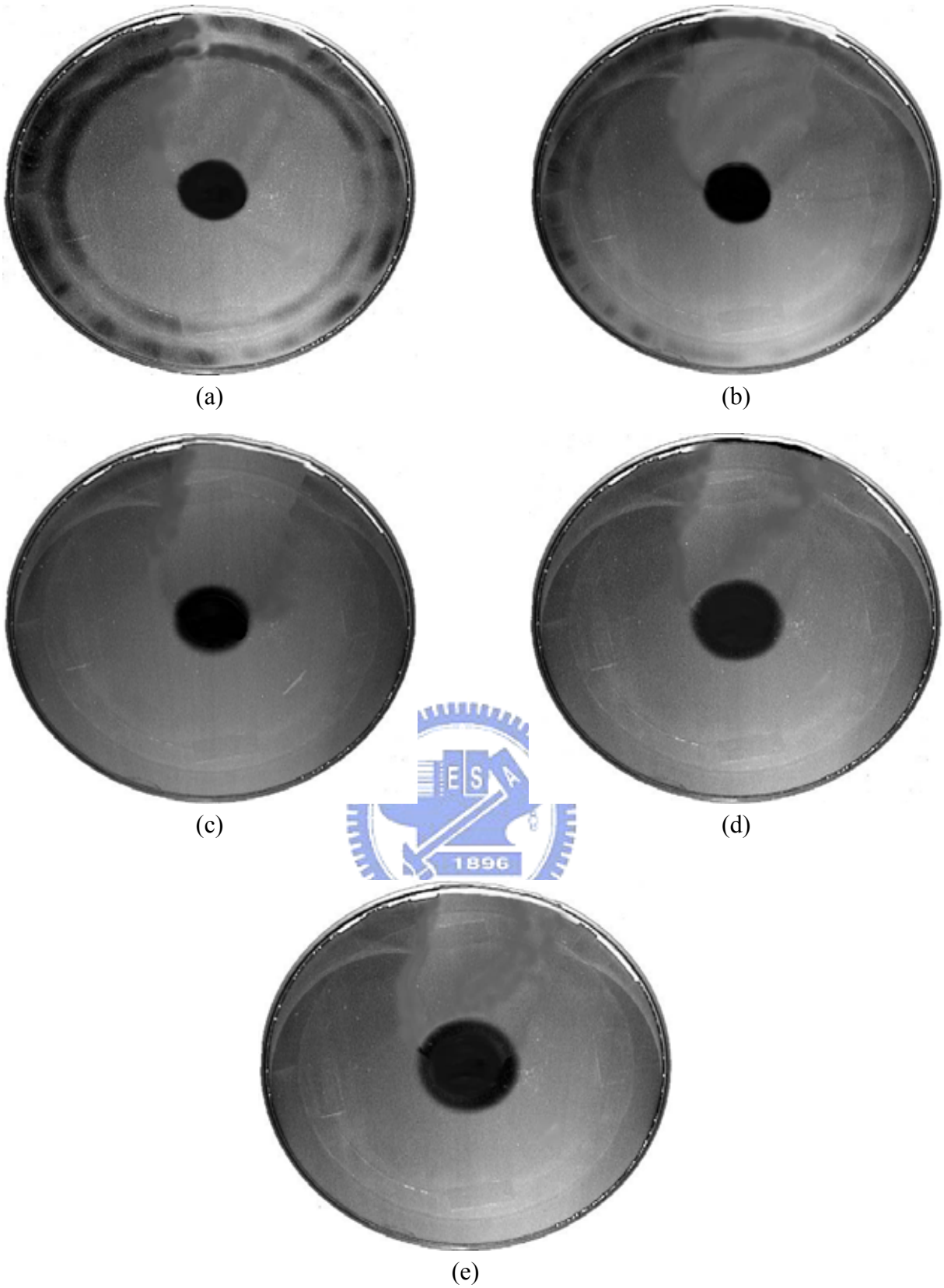

Fig. 3.29 Top view flow photos taken at the middle horizontal plane between the disk and chamber top with Ra=1,880 (ΔT=20.0℃) and D_j=22.1mm at H=10.0 mm for Re_j= (a) 61, (b) 122, (c) 184, (d) 245, and (e) 306.

Fig. 3.30 Top view flow photos taken at the middle horizontal plane between the disk and chamber top with Ra =2,350 (ΔT=25.0℃) and D_j=10.0 mm at H=10.0 mm for Re_j= (a) 135, (b) 270, (c) 406, (d) 541, and (e) 676.

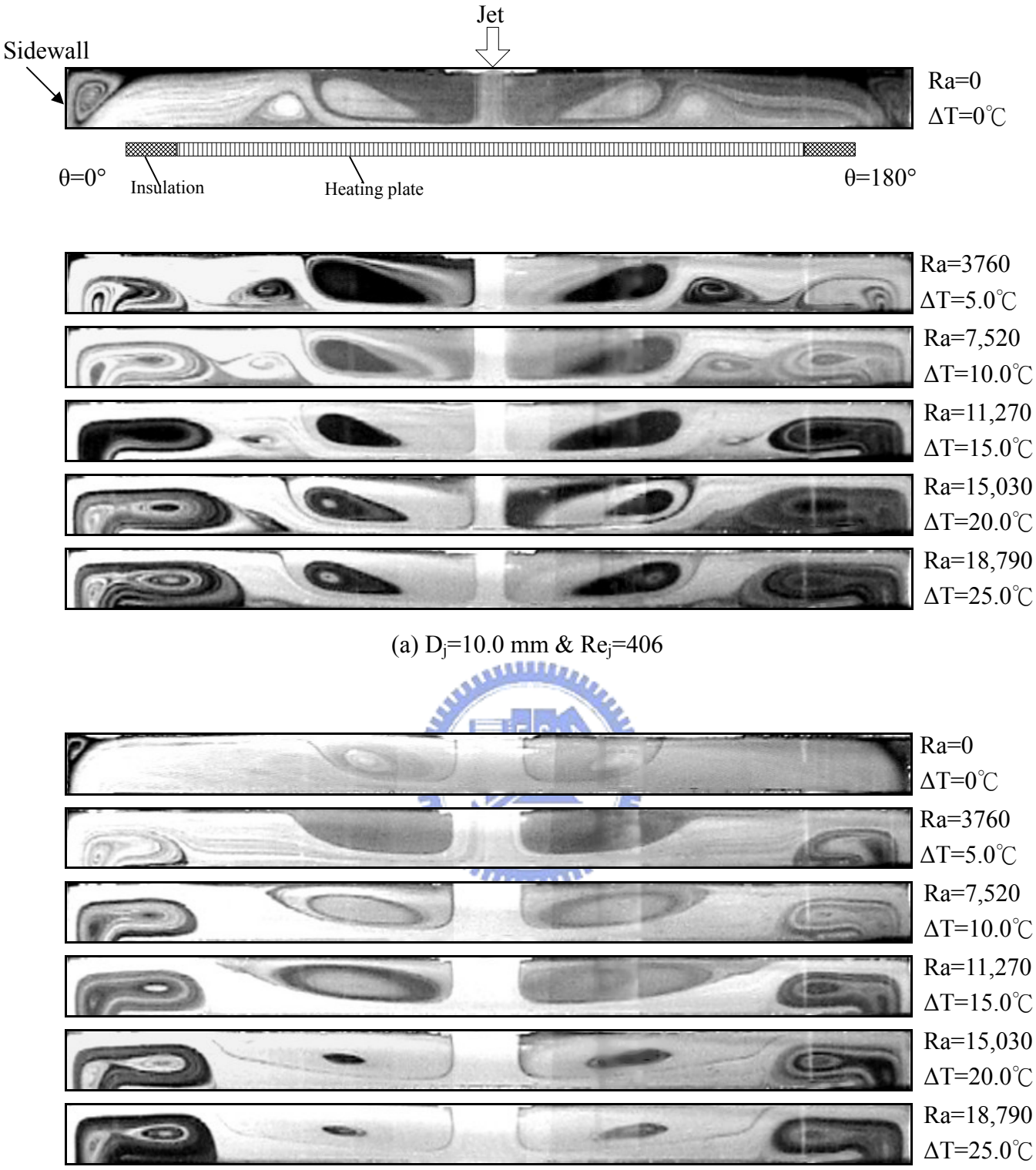

(a) D_j=10.0 mm & Re_j=406

(b) D_j=22.1 mm & Re_j=184

Fig. 3.31 Steady side view flow photos taken at the cross plane θ=0° & 180° for various Rayleigh numbers at Q_j=3.0 slpm for D_j= (a) 10.0 mm & Re_j=406 and (b) 22.1 mm & Re_j=184.

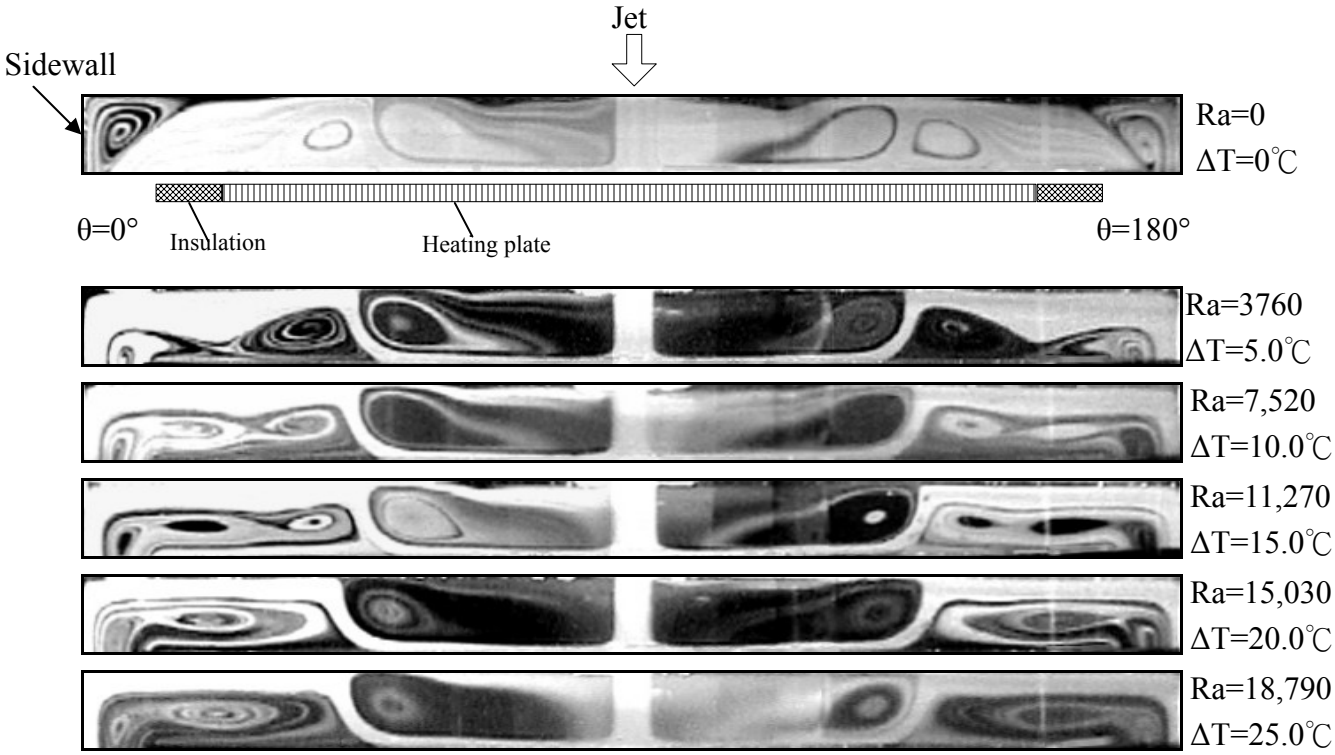

(a) D_j=10.0 mm & Re_j=676

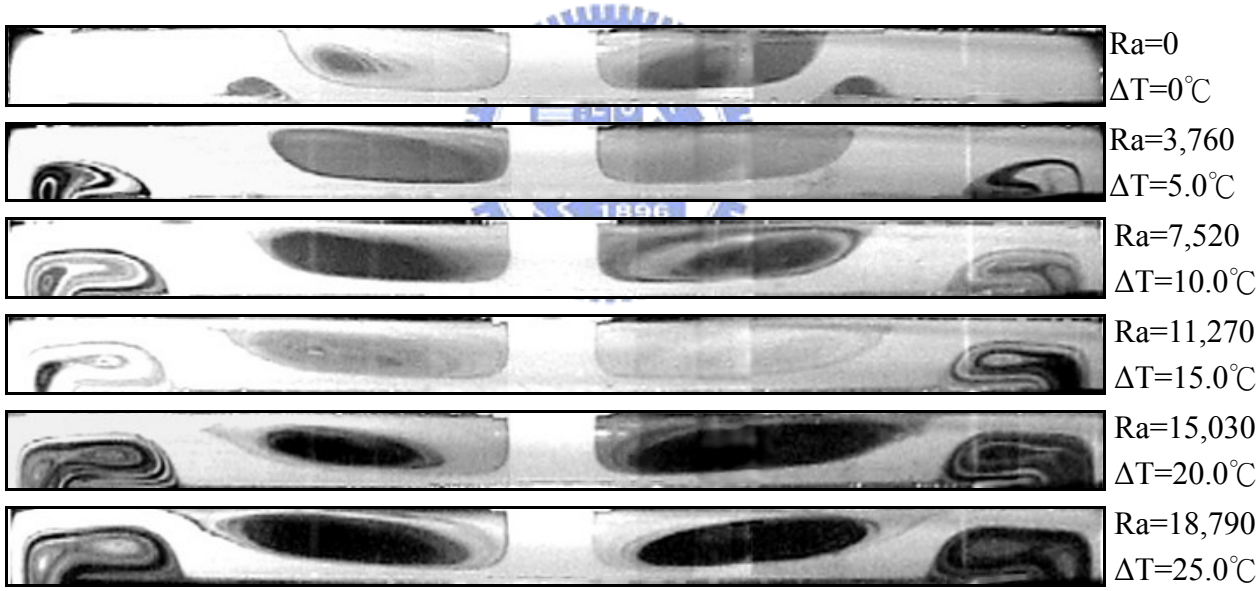

(b) D_j=22.1 mm & Re_j=306

Fig. 3.32 Steady side view flow photos taken at the cross plane θ=0° & 180° for various Rayleigh numbers at Q_j=5.0 slpm for D_j= (a) 10.0 mm & Re_j=676 and (b) 22.1 mm & Re_j=306.

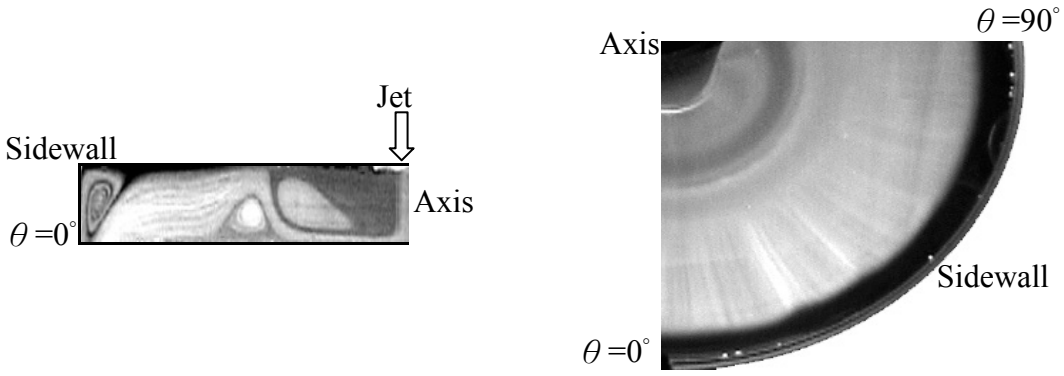

(a) Ra=0 & Re_j=406

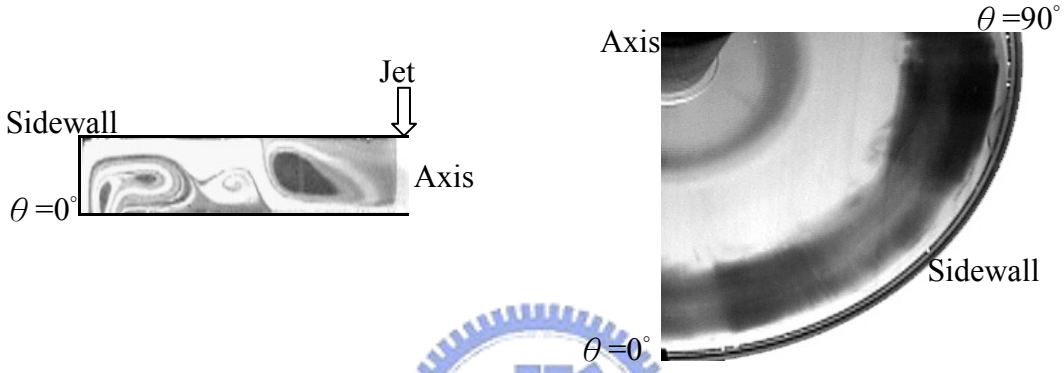

(b) Ra=7,520 & Re_j=406

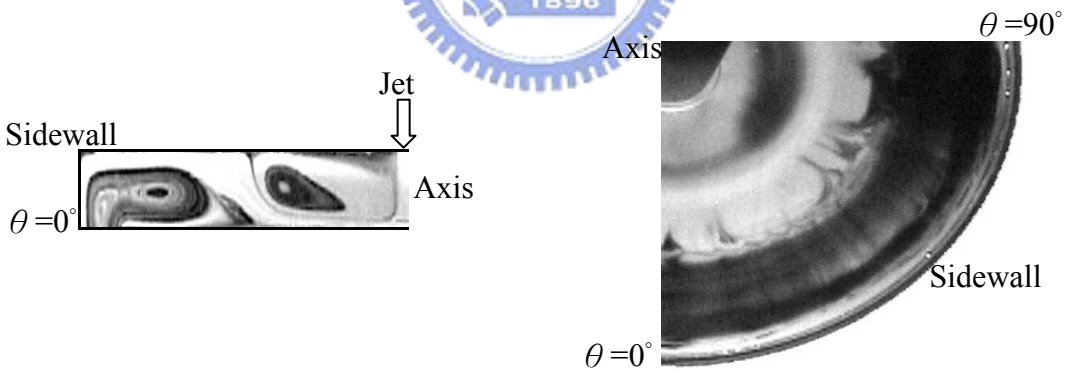

(c) Ra=15,030 & Re_j=406

Fig. 3.33 Half of side view flow photos taken at θ=0° (left) and quarter of top view flow photos (right) taken at midheight of the chamber with Q_j=3.0 slpm, H=20.0 mm and D_j=10.0 mm at steady state for Ra= (a) 0, (b) 7,520, and (c) 15,030.

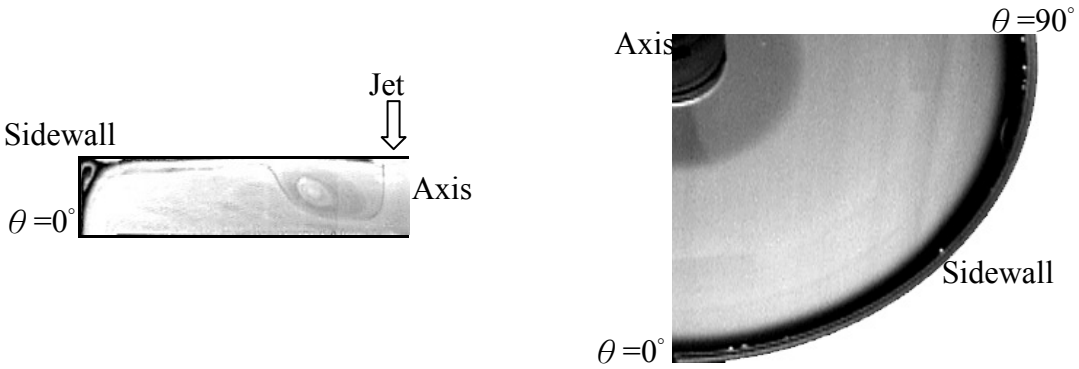

(a) Ra=0 & Re_j=184

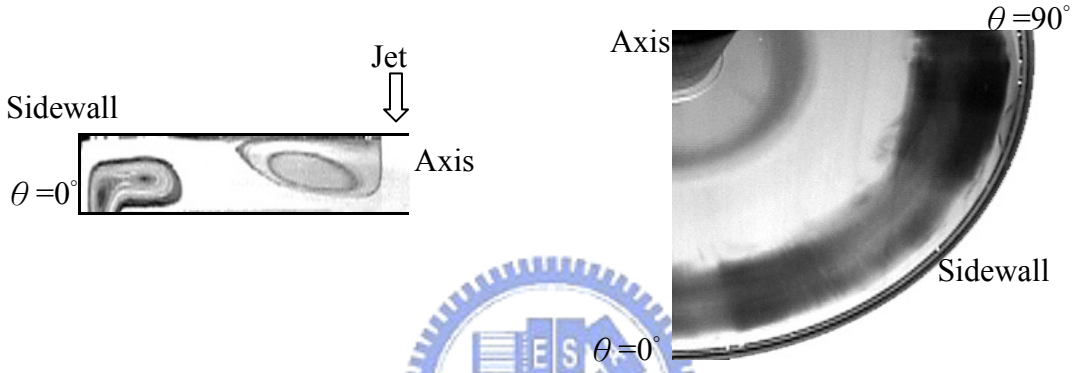

(b) Ra=7,520 & Re_j=184

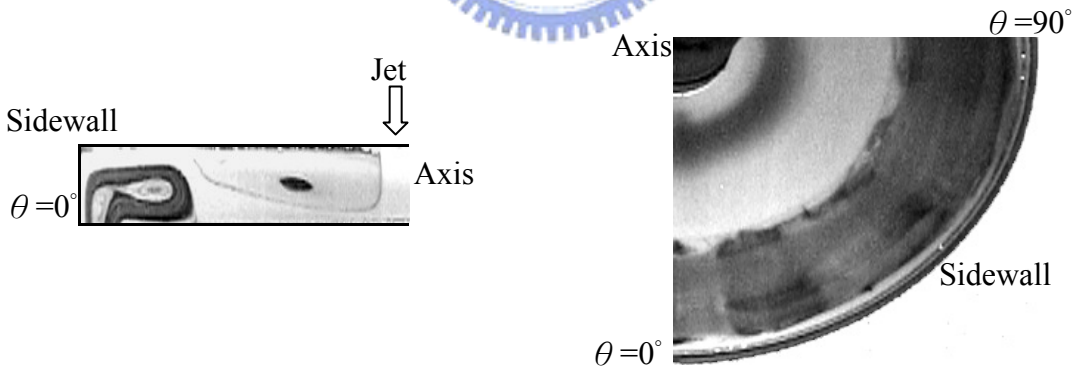

(c) Ra=15,030 & Re_j=184

Fig. 3.34 Half side view flow photos taken at θ =0° (left) and quarter of top view flow photos (right) taken at midheight of the chamber with Q_j=3.0 slpm, H=20.0 mm and D_j=22.1 mm at steady state for Ra=(a) 0, (b) 7,520, and (c) 15,030.

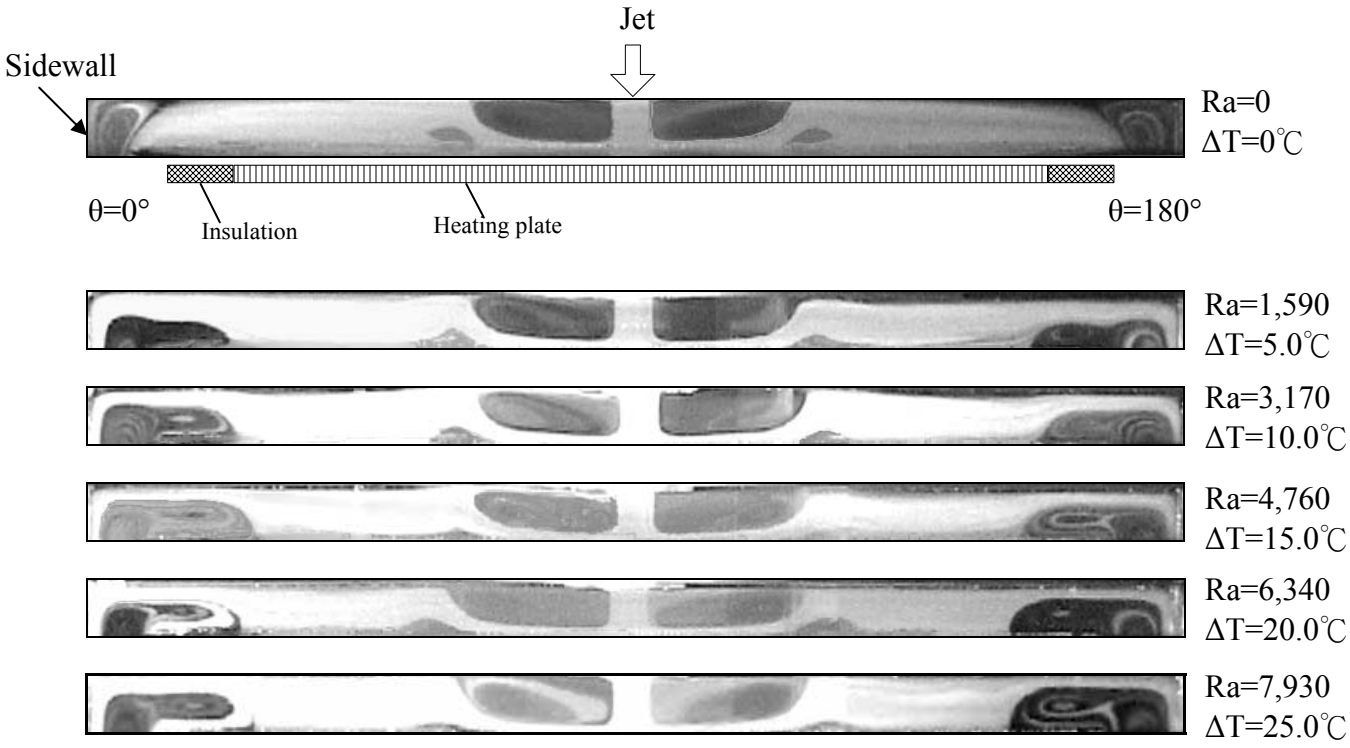

(a) D_j=10.0 mm & Re_j=270

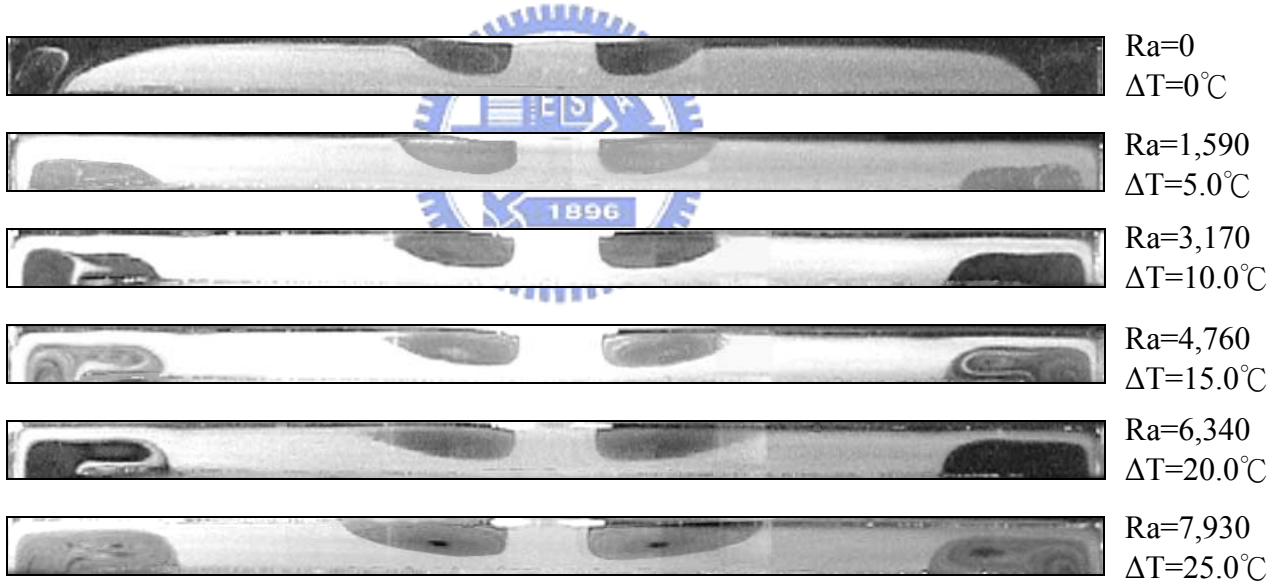

(b) D_j=22.1 mm & Re_j=122

Fig. 3.35 Steady side view flow photos taken at the cross plane θ=0° & 180° for various Rayleigh numbers at H=15.0 mm with Q_j=2.0 slpm for D_j= (a) 10.0 mm and (b) 22.1 mm.

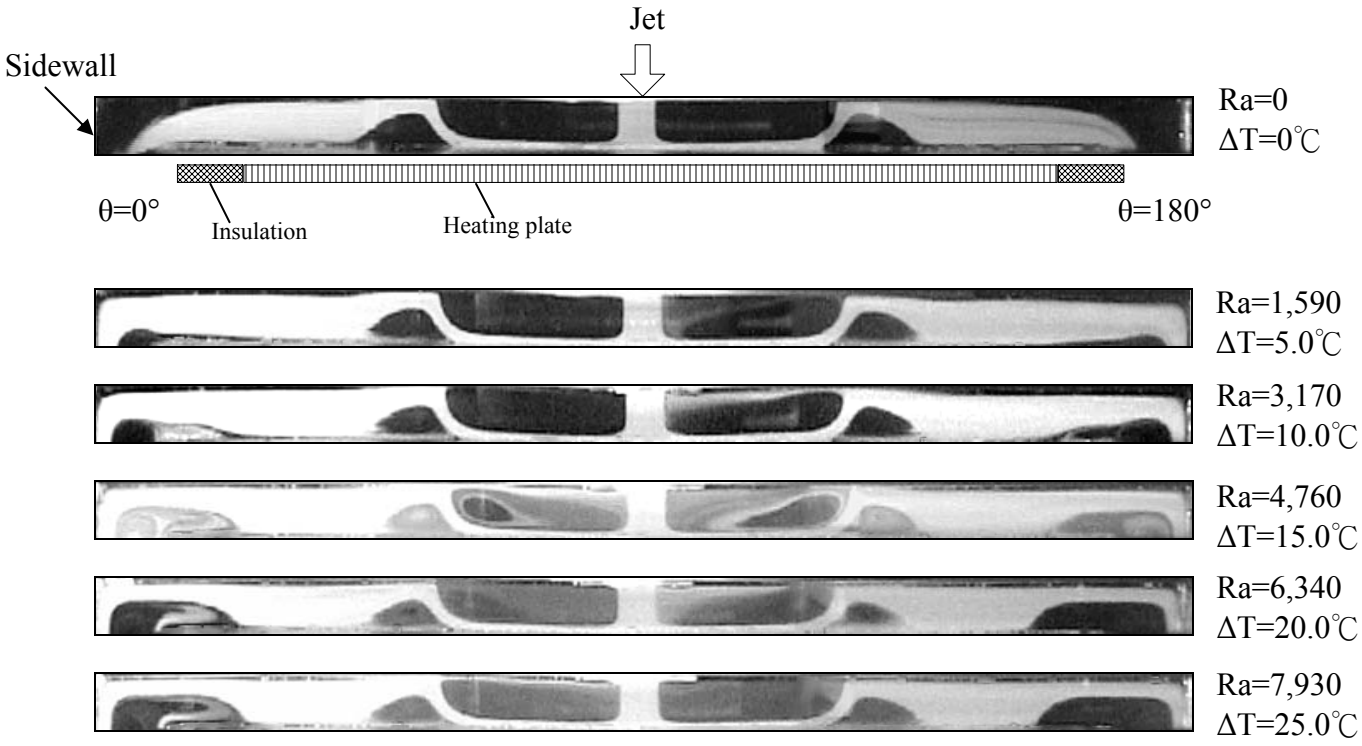

(a) D_j=10.0 mm & Re_j=541

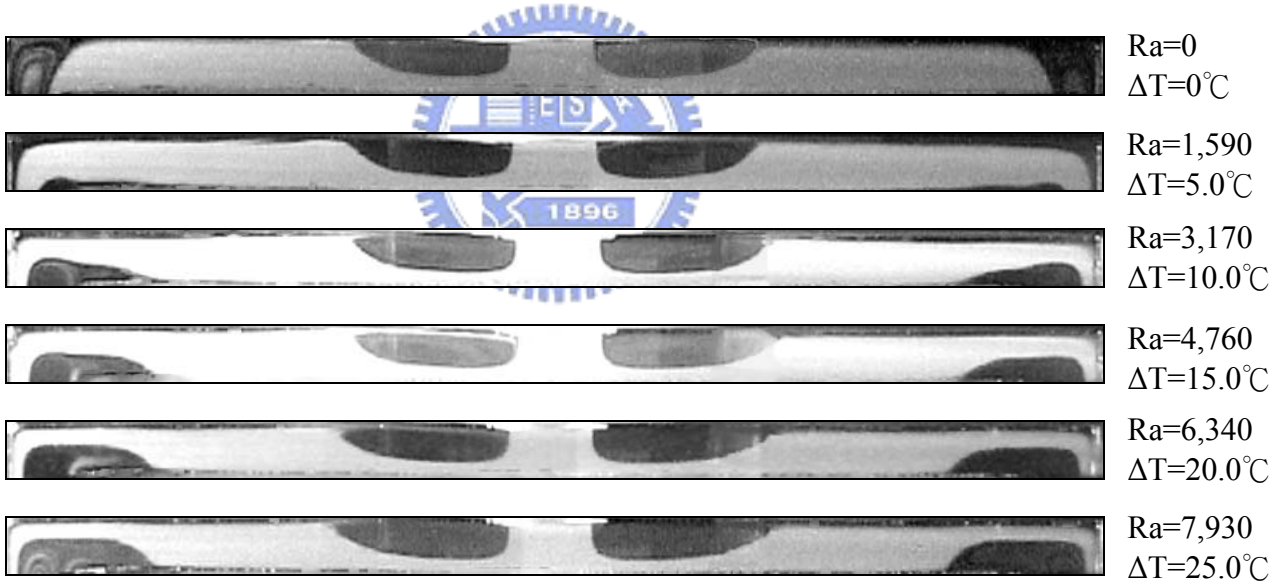

(b) D_j=22.1 mm & Re_j=240

Fig. 3.36 Steady side view flow photos taken at the cross plane θ=0° & 180° for various Rayleigh numbers at H=15.0 mm with Q_j=4.0 slpm for D_j= (a) 10.0 mm and (b) 22.1 mm.

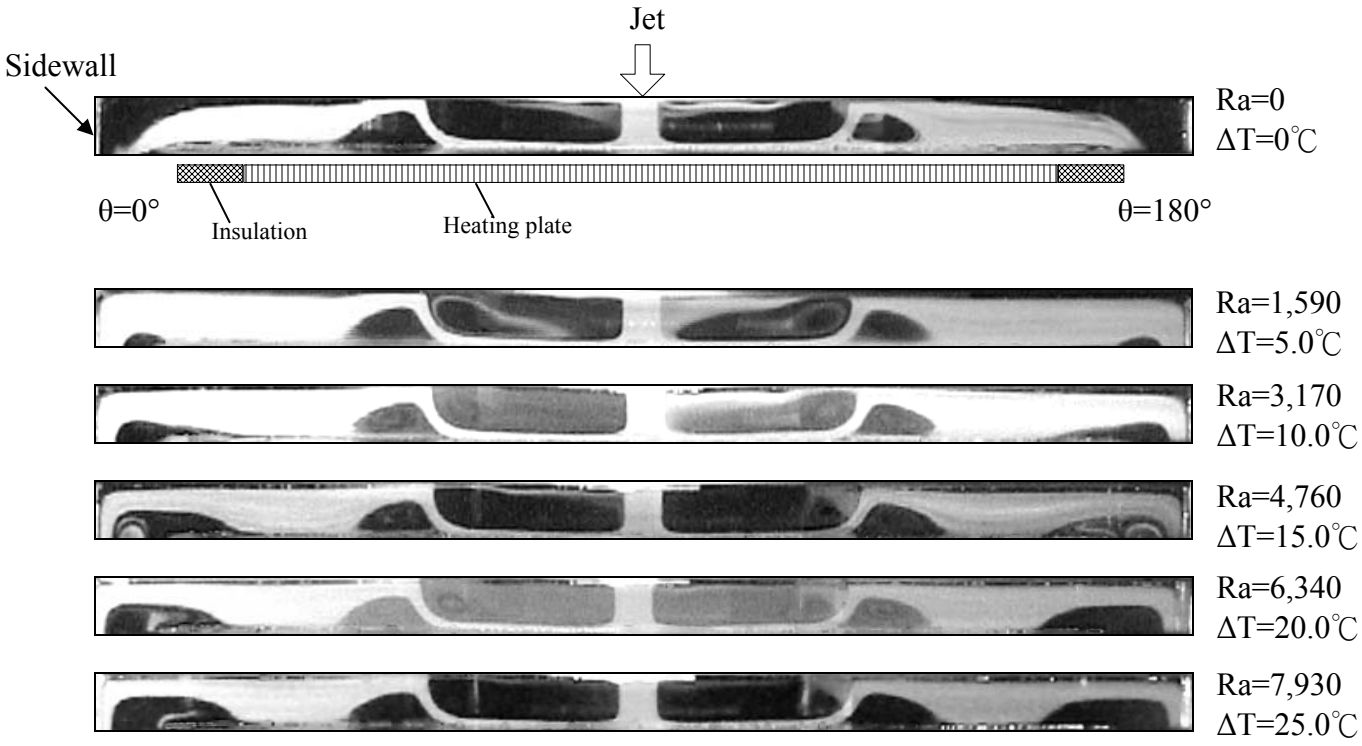

(a) D_j=10.0 mm & Re_j=676

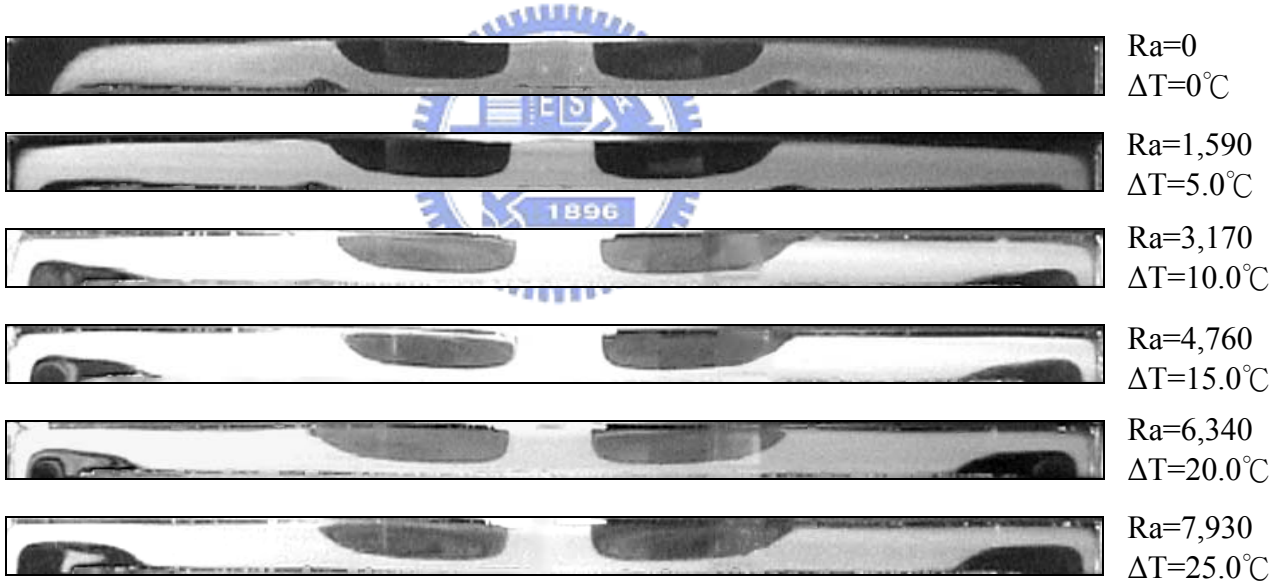

(b) D_j=22.1 mm & Re_j=306

Fig. 3.37 Steady side view flow photos taken at the cross plane θ=0° & 180° for various Rayleigh numbers at H=15.0 mm with Q_j=5.0 slpm for D_j=(a) 10.0 mm and (b) 22.1 mm.

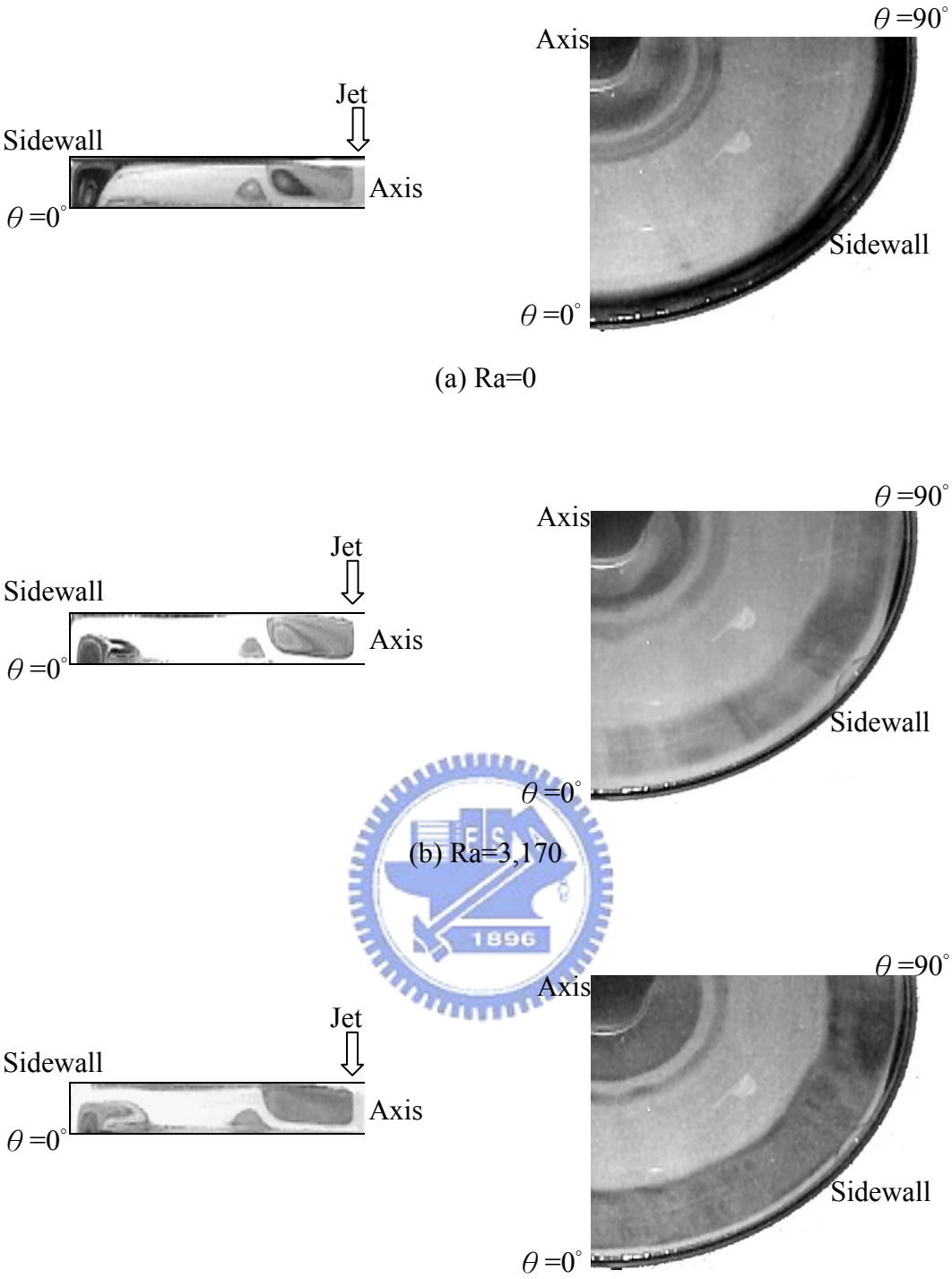

Fig. 3.38 Half side view flow photos taken at θ =0° (left) and quarter of top view flow photos (right) taken at midheight of the chamber with Re_j=406, H=15.0 mm and D_j=10.0 mm at steady state for Ra= (a) 0, (b) 3,170, and (c) 6,340.

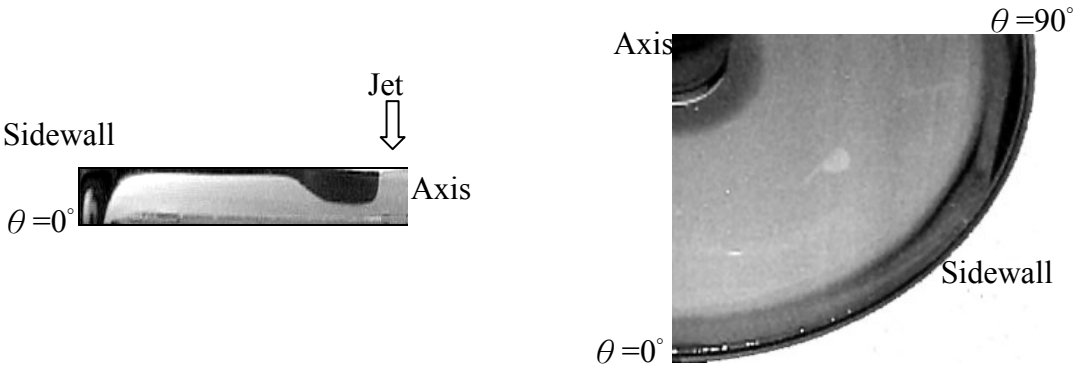

(a) Ra=0

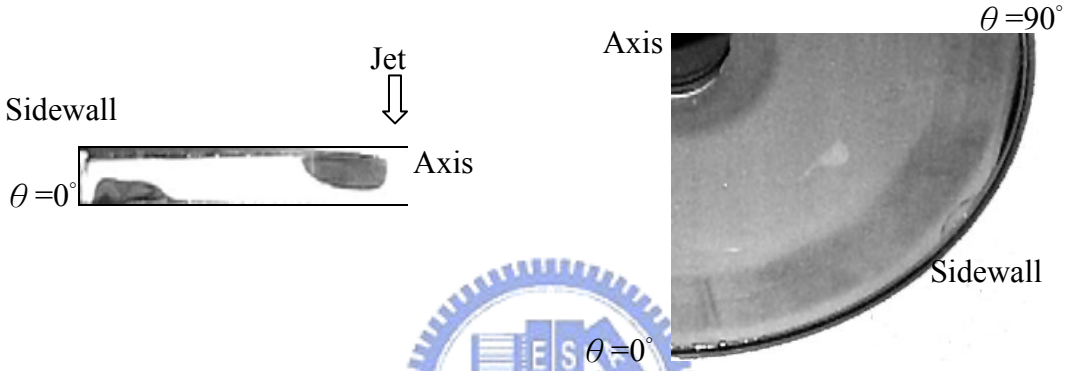

(b) Ra=3,170

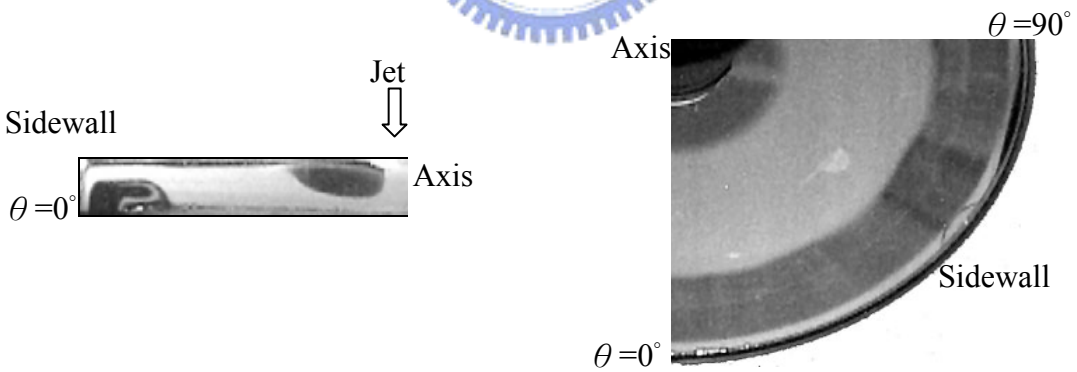

(c) Ra=6,340

Fig. 3.39 Half side view flow photos taken at θ =0° (left) and quarter of top view flow photos (right) taken at middle horizontal plane with Re_j=184, H=15.0 mm and D_j=22.1 mm at steady state for Ra=(a) 0, (b) 3,170, and (c) 6,340.

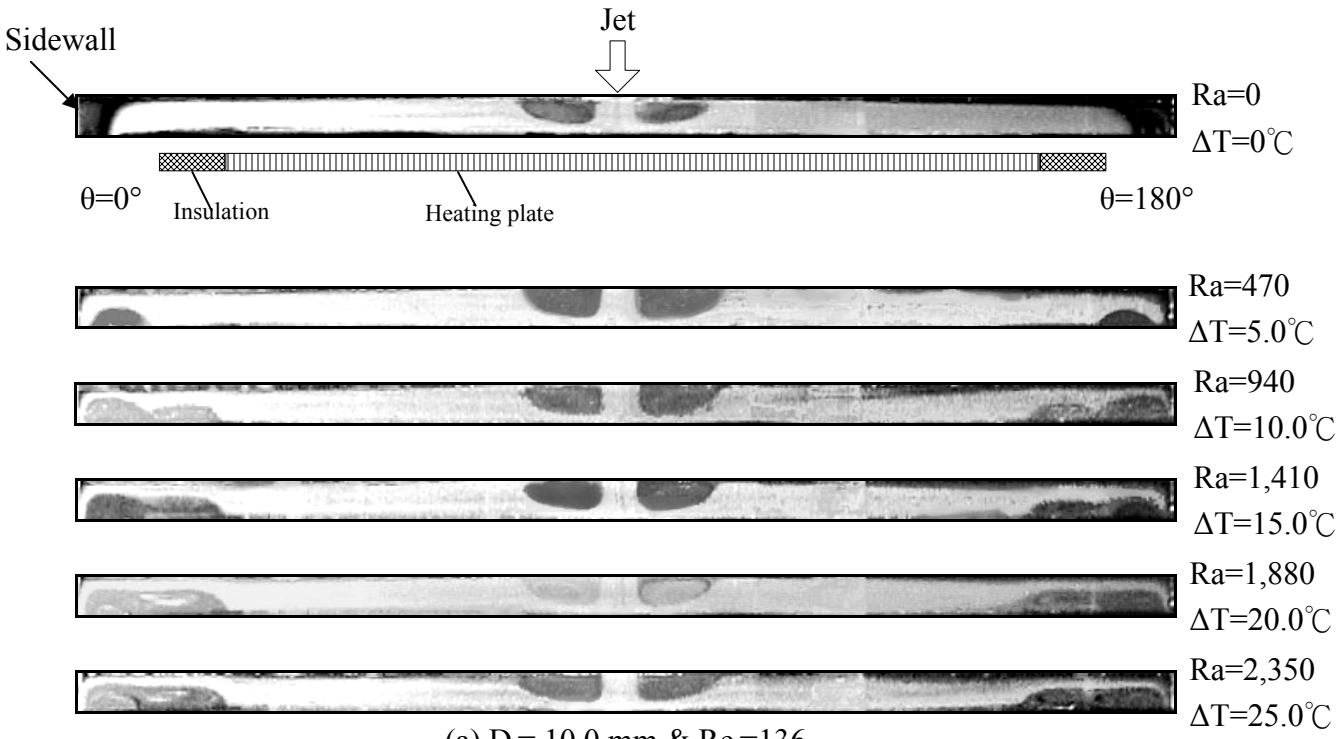

(a) D_j= 10.0 mm & Re_j=136

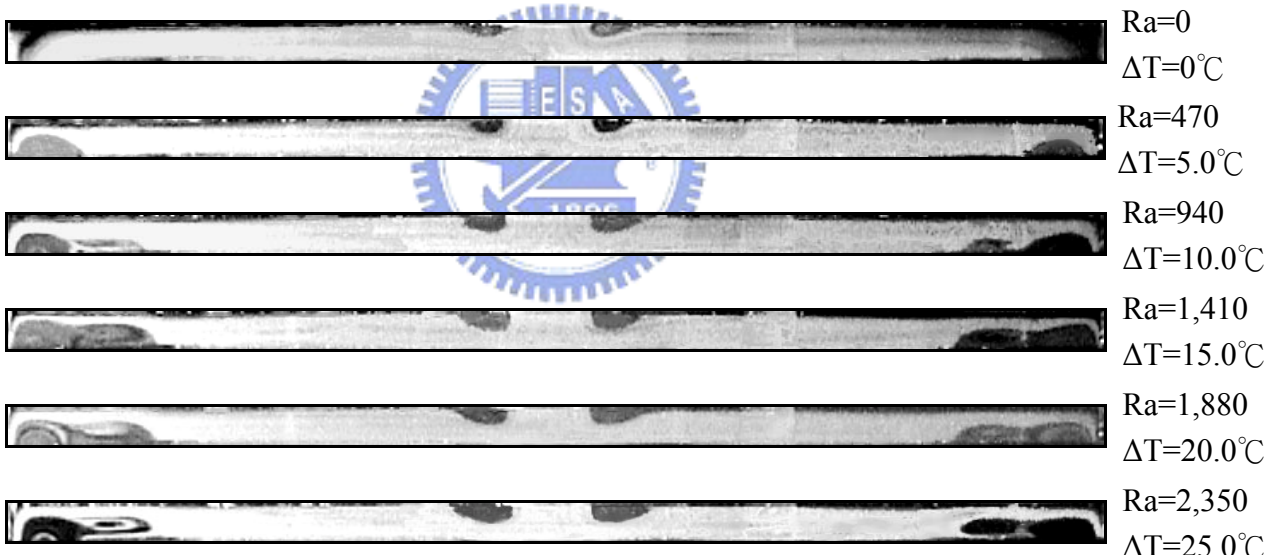

(b) D_j= 22.1 mm & Re_j=61

Fig. 3.40 Steady side view flow photos taken at the cross plane θ=0° & 180° for various Rayleigh numbers at H=10.0 mm & Q_j=1.0 slpm for D_j= (a) 10.0 mm and (b) 22.1 mm.

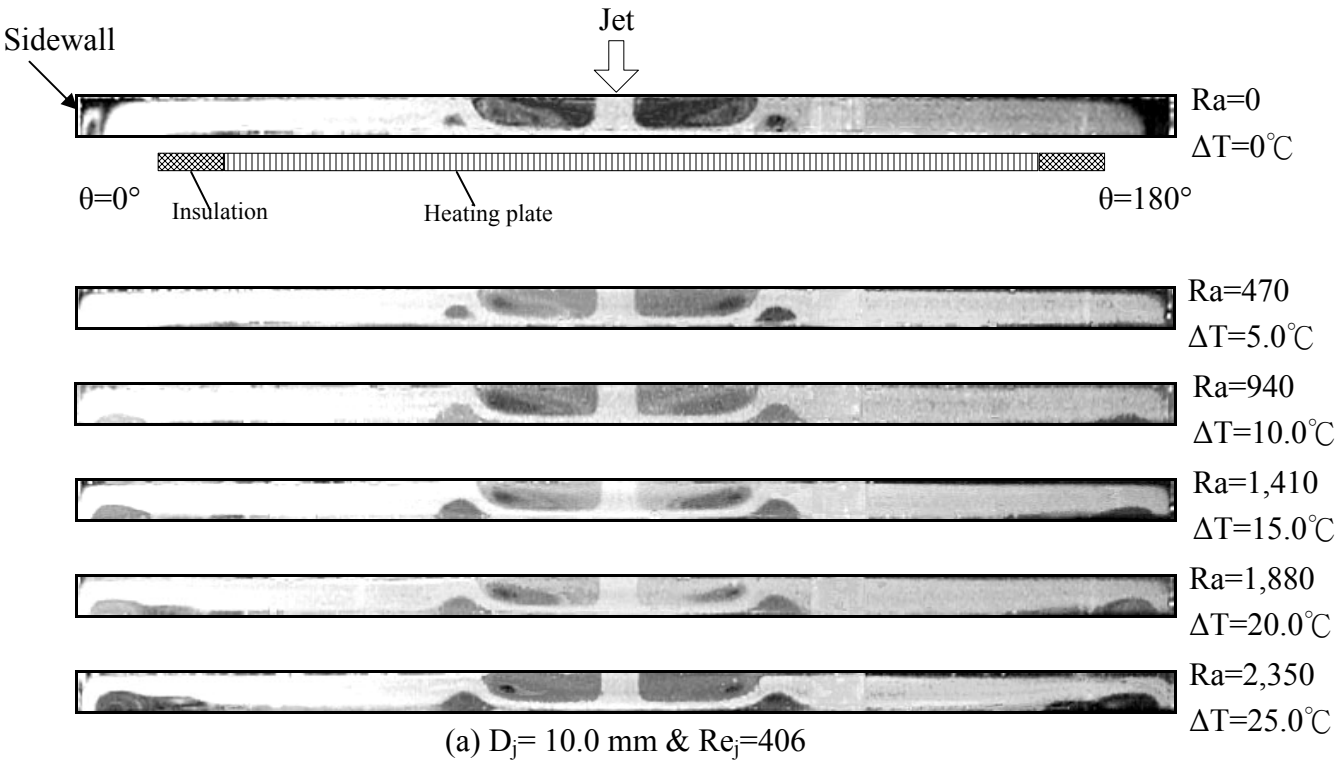

(a) D_j= 10.0 mm & Re_j=406

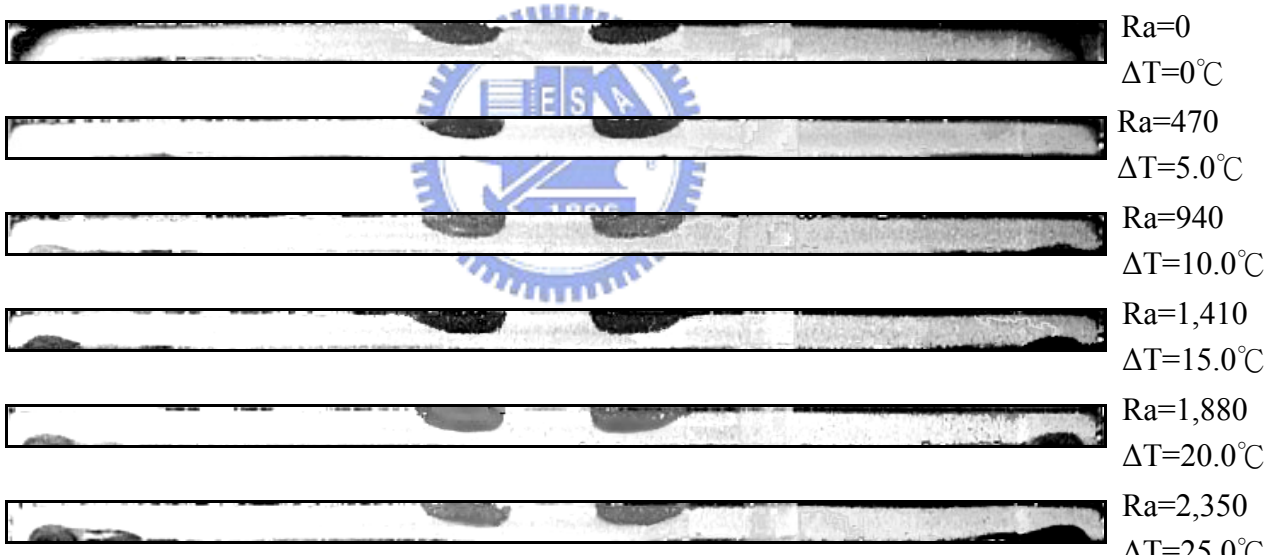

(b) D_j= 22.1 mm & Re_j=184

Fig. 3.41 Steady side view flow photos taken at the cross plane θ=0° & 180° for various Rayleigh numbers at H=10.0 mm & Q_j=3.0 slpm for D_j= (a) 10.0 mm and (b) 22.1 mm.

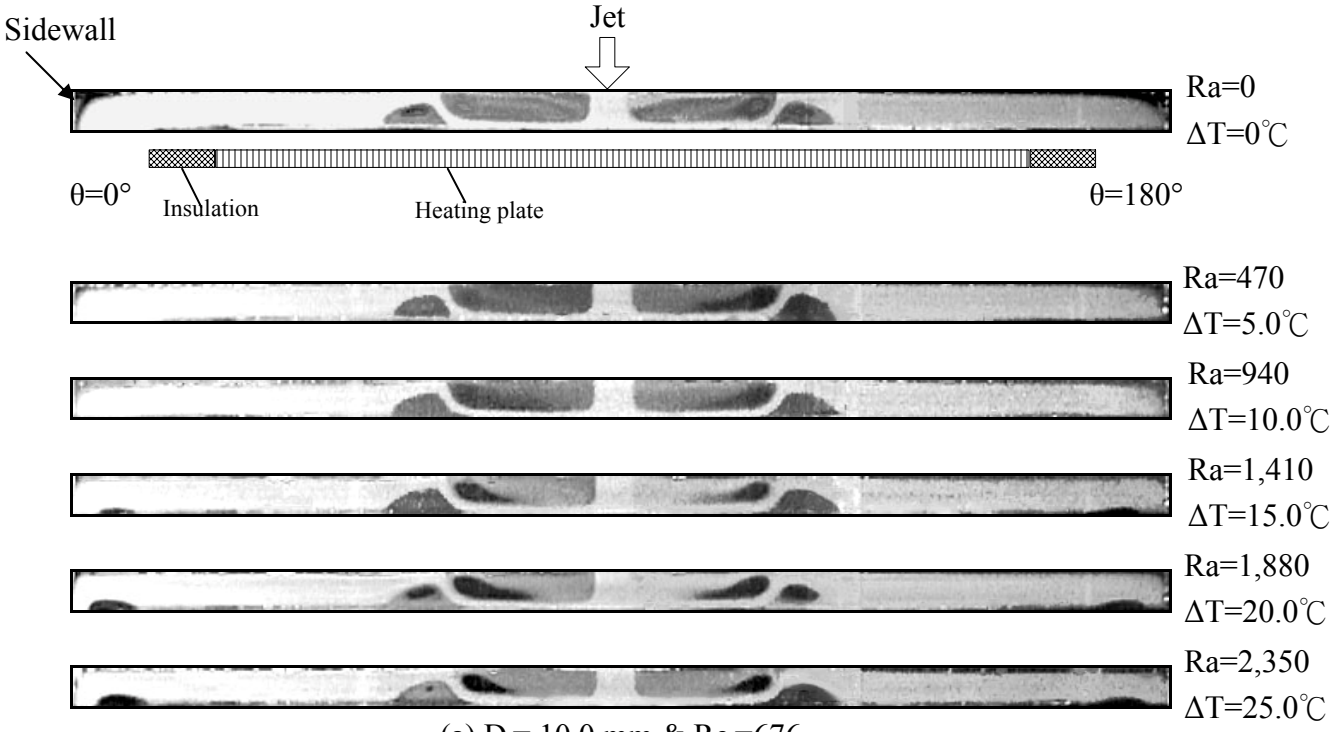

(a) D_j= 10.0 mm & Re_j=676

(b) D_j= 22.1 mm & Re_j=306

Fig. 3.42 Steady side view flow photos taken at the cross plane θ=0° & 180° for various Rayleigh numbers at H=10.0 mm & Q_j=5.0 slpm for D_j= (a) 10.0 mm and (b) 22.1 mm.

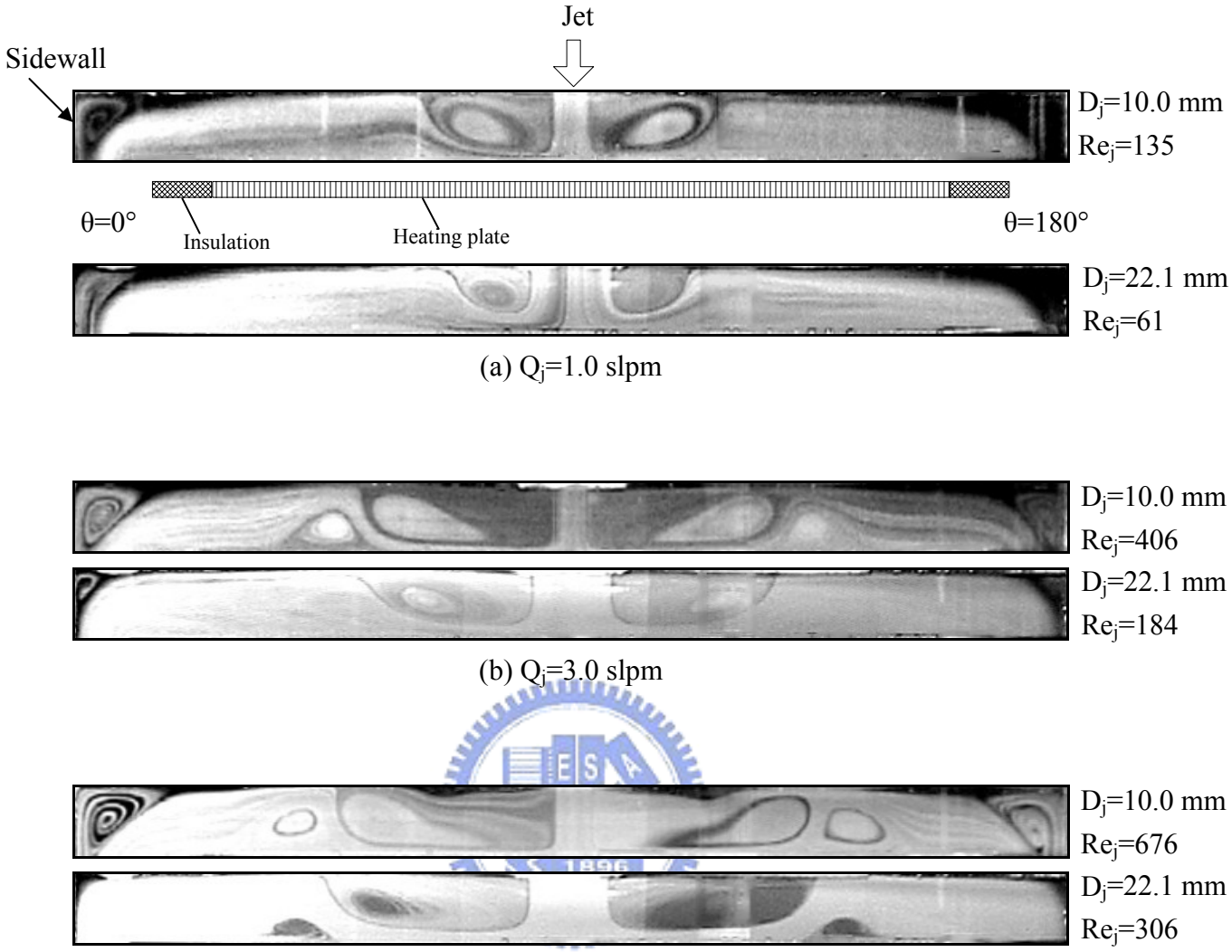

Fig. 3.43 Steady side view flow photos taken at the cross plane θ=0° & 180° at Q_j=3.0 slpm & H=20.0 mm with Ra=0.

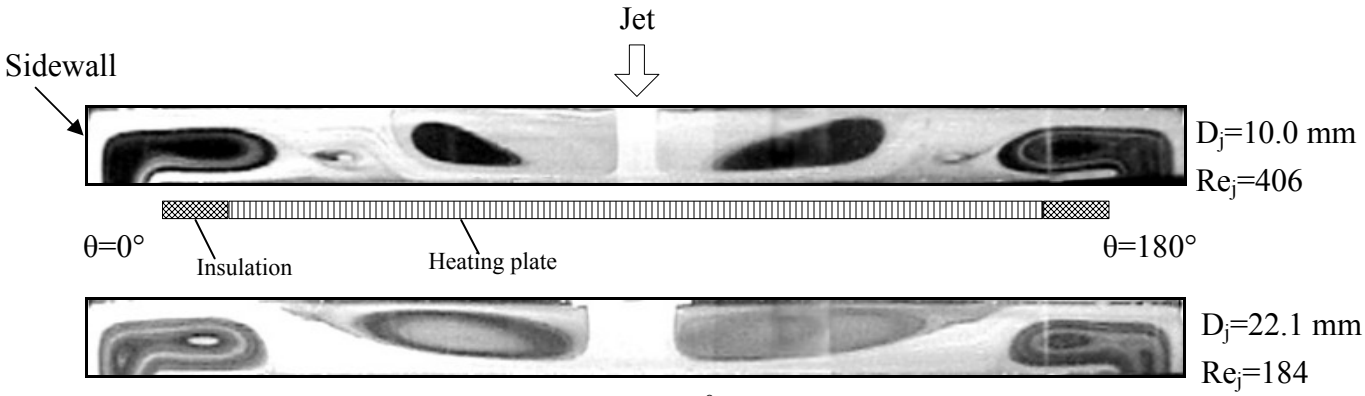

(a) Q_j=3.0 slpm & ΔT=15.0℃ (Ra=11,270)

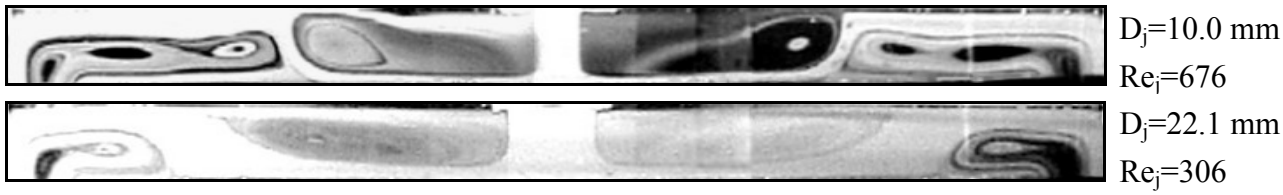

(b) Q_j=5.0 slpm & ΔT=15.0℃ (Ra=11,270)

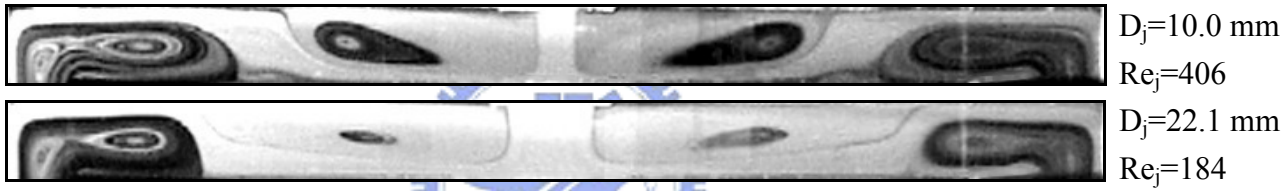

(c) Q_j=3.0 slpm & ΔT=25.0℃ (Ra=18,790)

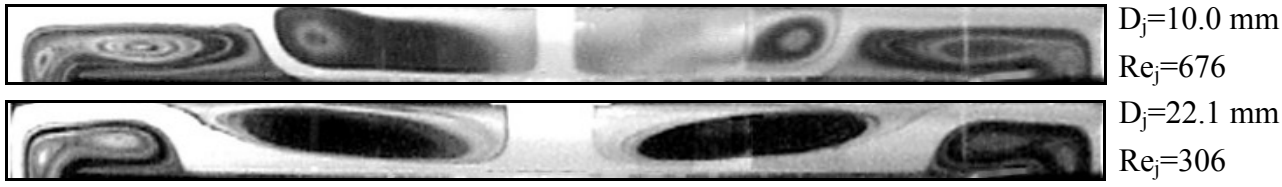

(d) Q_j=5.0 slpm & ΔT=25.0℃ (Ra=18,790)

Fig. 3.44 Steady side view flow photos taken at the cross plane θ=0° & 180° at H=20.0 mm.

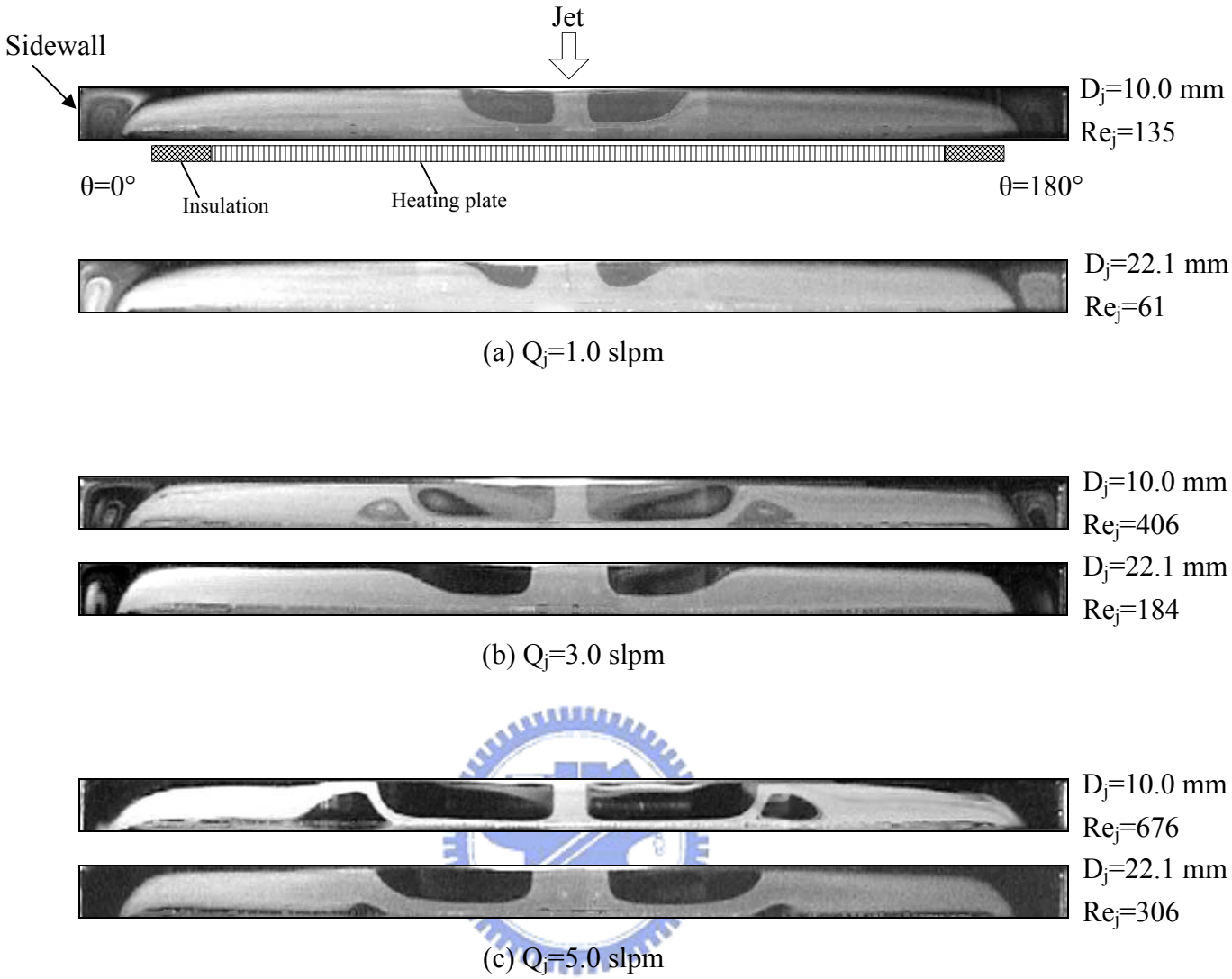

Fig. 3.45 Steady side view flow photos taken at the cross plane θ =0° & 180° at H=15.0 mm with Ra=0.

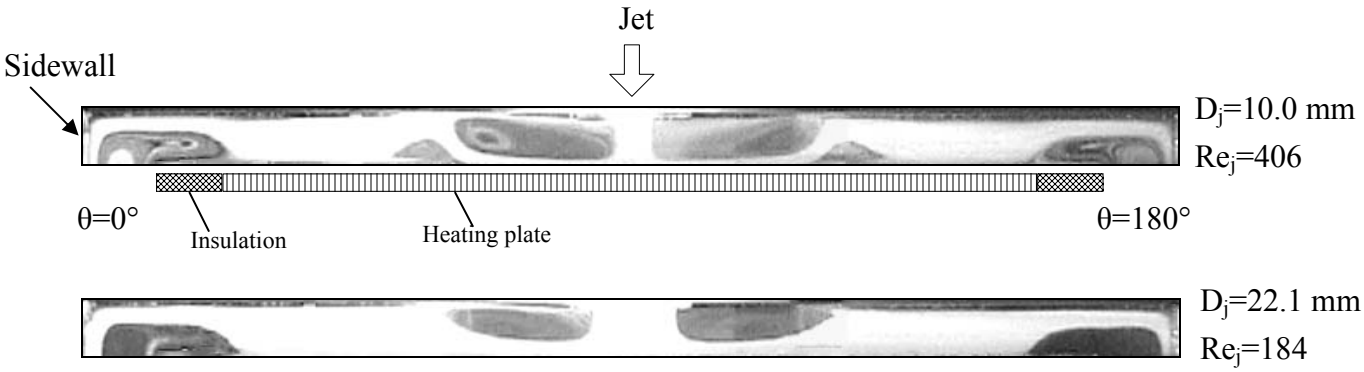

(a) Q_j=3.0 slpm & ΔT=15.0℃ (Ra=4,760)

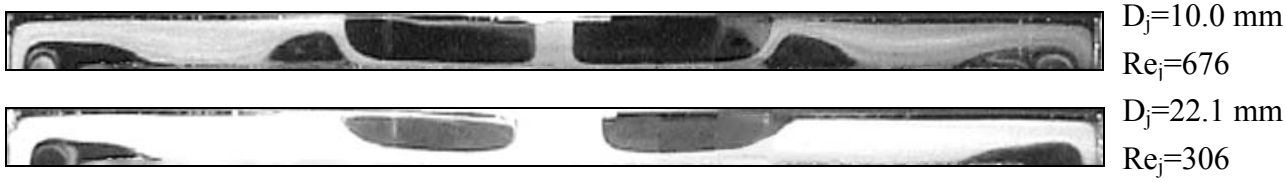

(b) Q_j=5.0 slpm & ΔT=15.0℃ (Ra=4,760)

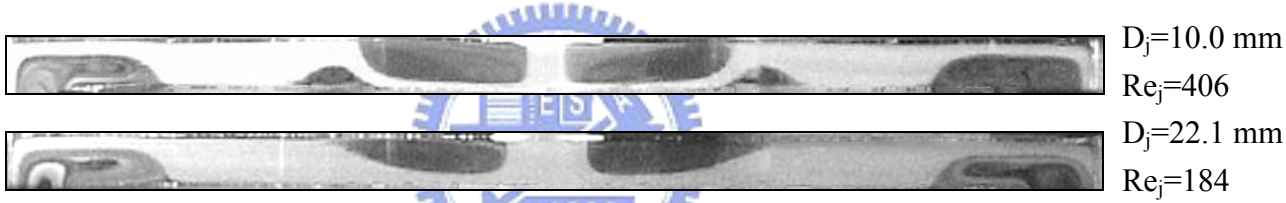

(c) Q_j=3.0 slpm & ΔT=25.0℃ (Ra=7,930)

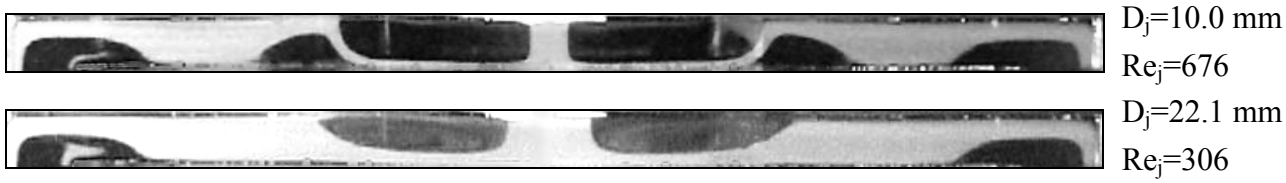

(d) Q_j=5.0 slpm & ΔT=25.0℃ (Ra=7,930)

Fig. 3.46 Steady side view flow photos taken at the cross plane θ=0° & 180° at H=15.0 mm.

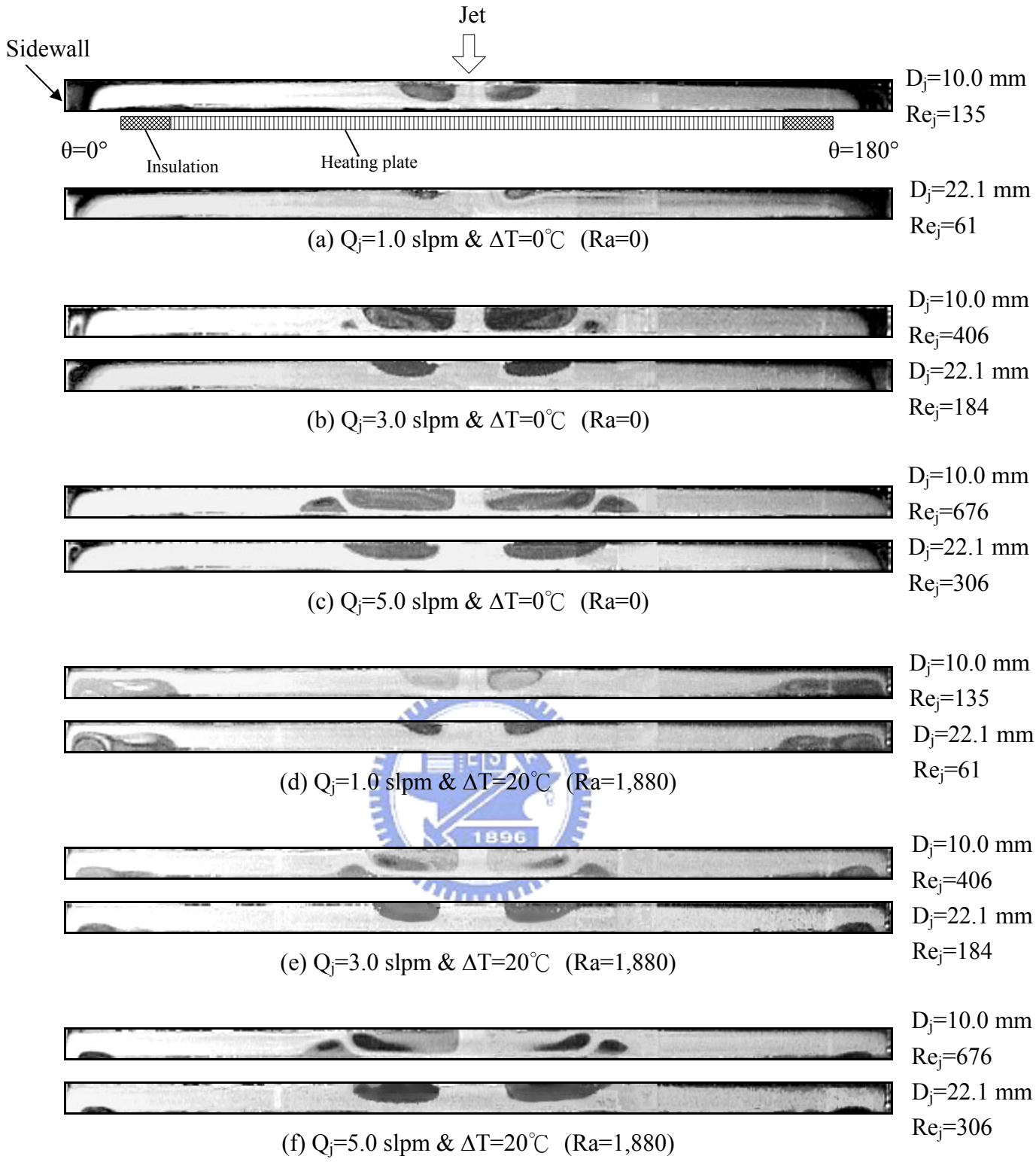

Fig. 3.47 Steady side view flow photos taken at the cross plane θ=0° & 180° at H=10.0 mm.

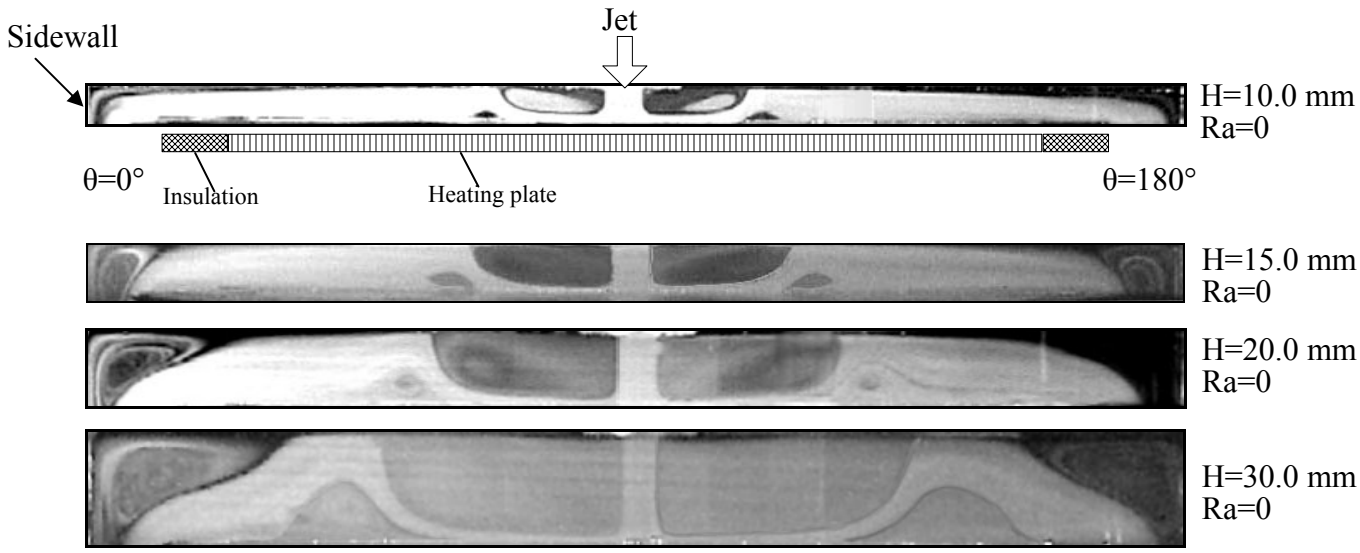

(a) $\Delta T=0℃$ & $Q_j=2.0$ slpm ($Re_j=270$)

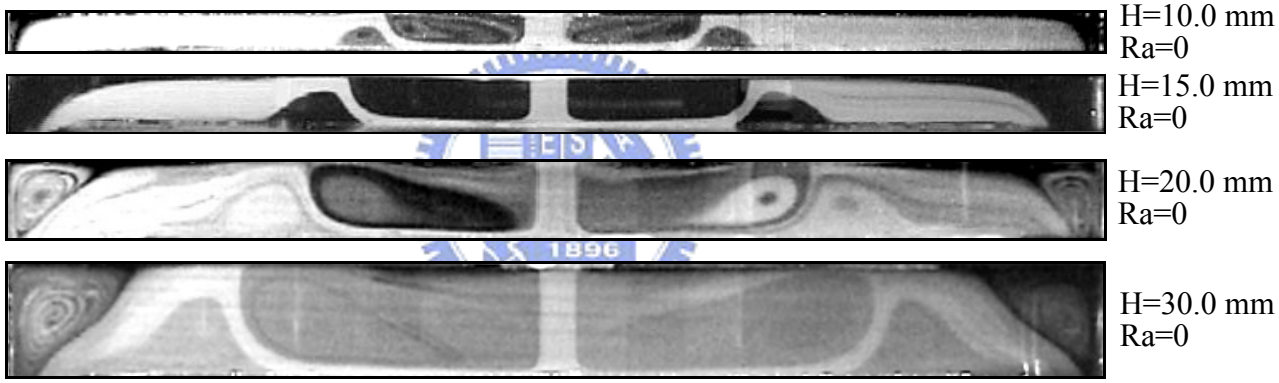

(b) $\Delta T=0℃$ & $Q_j=4.0$ slpm ($Re_j=541$)

Fig. 3.48 Steady side view flow photos taken at the cross plane $\theta=0°$ & 180° for $D_j=10.0$ mm at given $\Delta T=0℃$ for various H.

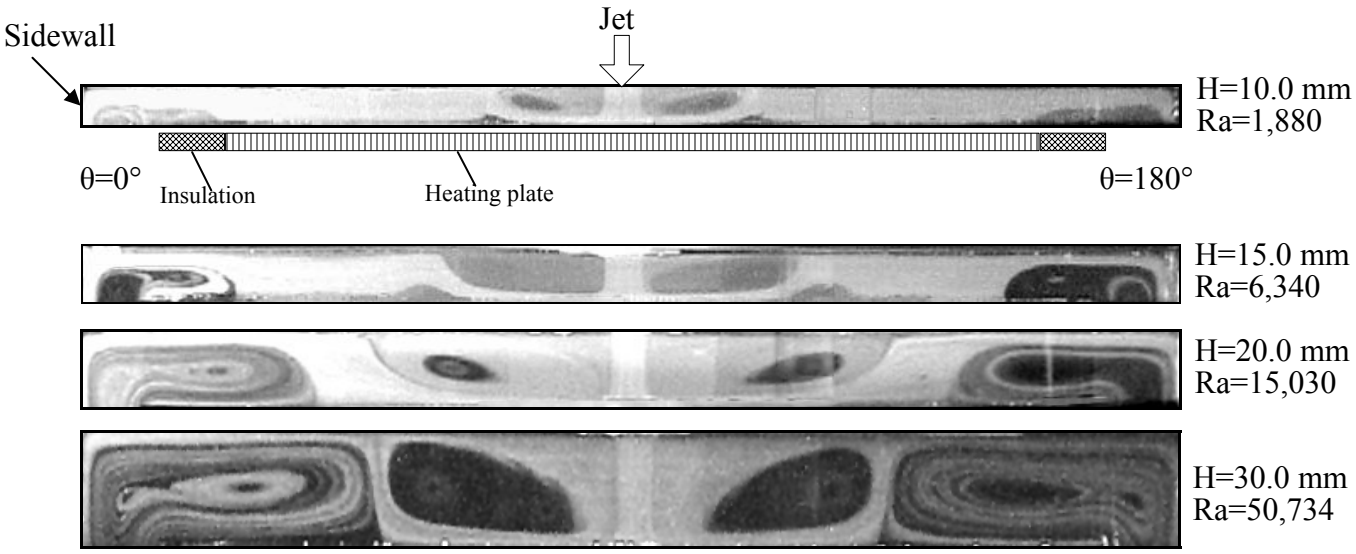

(a) ΔT=20.0℃ & Q_j=2.0 slpm (Re_j=270)

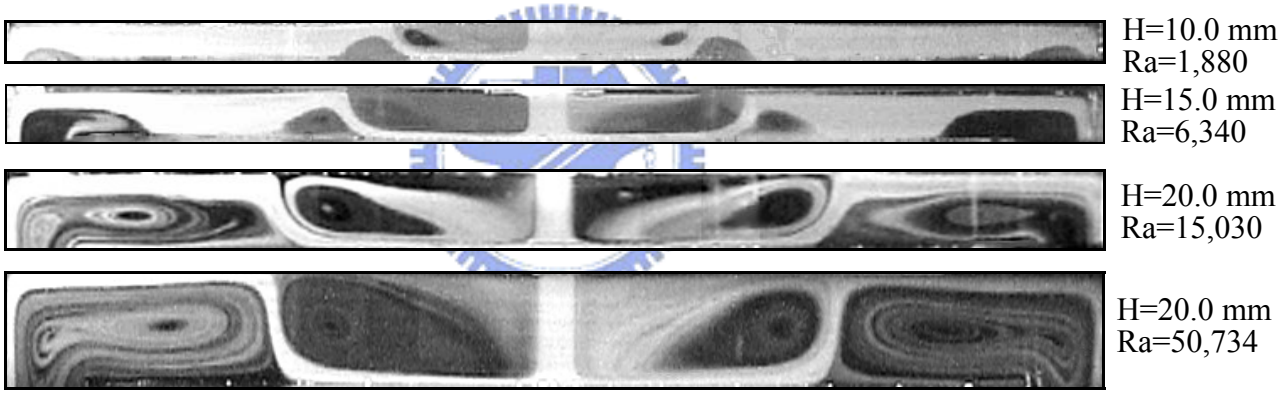

(b) ΔT=20.0℃ & Q_j=5.0 slpm (Re_j=676)

Fig. 3.49 Steady side view flow photos taken at the cross plane θ=0° & 180° for D_j=10.0 mm at given ΔT=20.0℃ for various H.

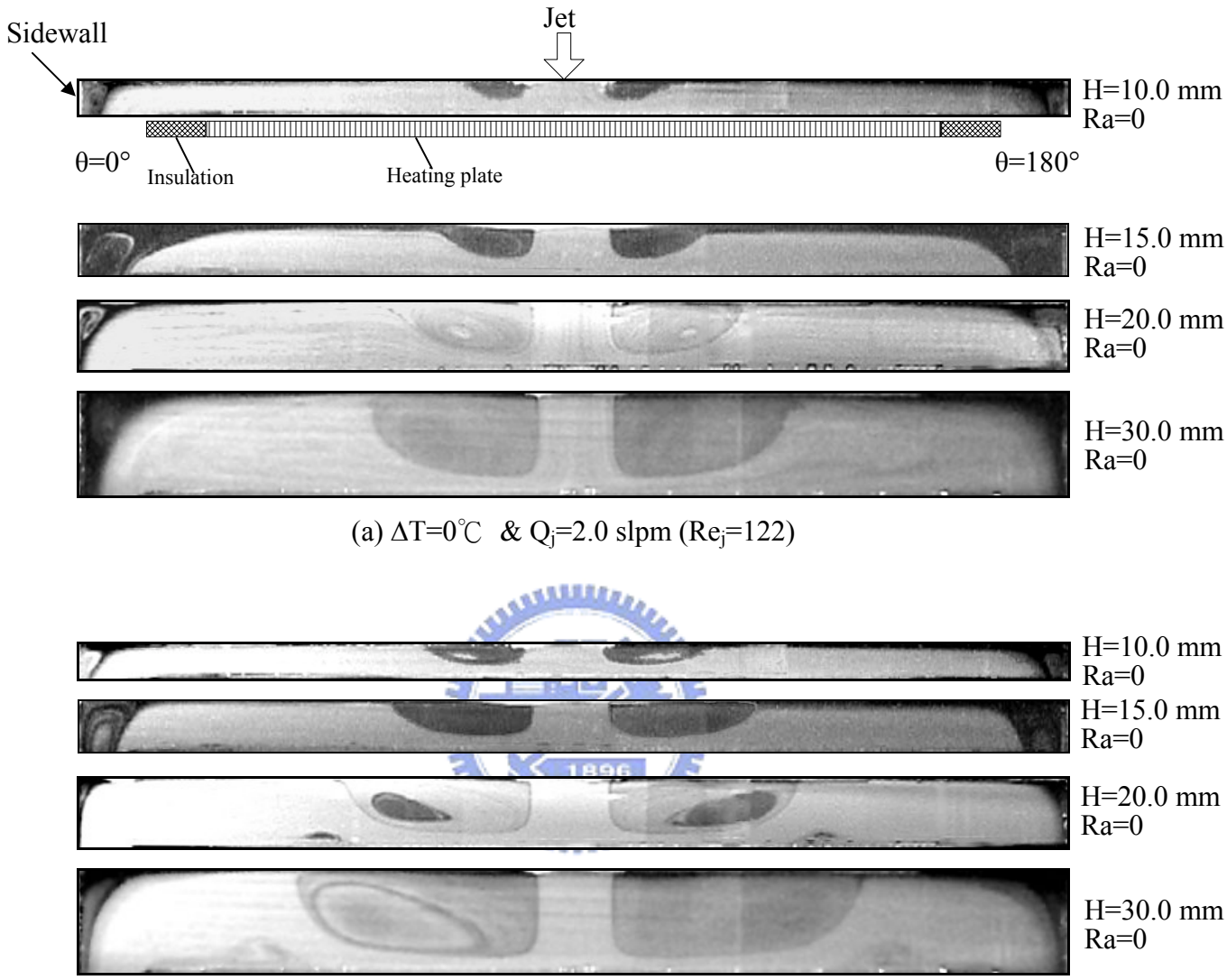

(a) $\Delta T=0℃$ & $Q_j=2.0$ slpm ($Re_j=122$)

(b) $\Delta T=0℃$ & $Q_j=4.0$ slpm ($Re_j=245$)

Fig. 3.50 Steady side view flow photos taken at the cross plane $\theta=0°$ & 180° for $D_j=22.1$ mm at given $\Delta T=0℃$ for various H.

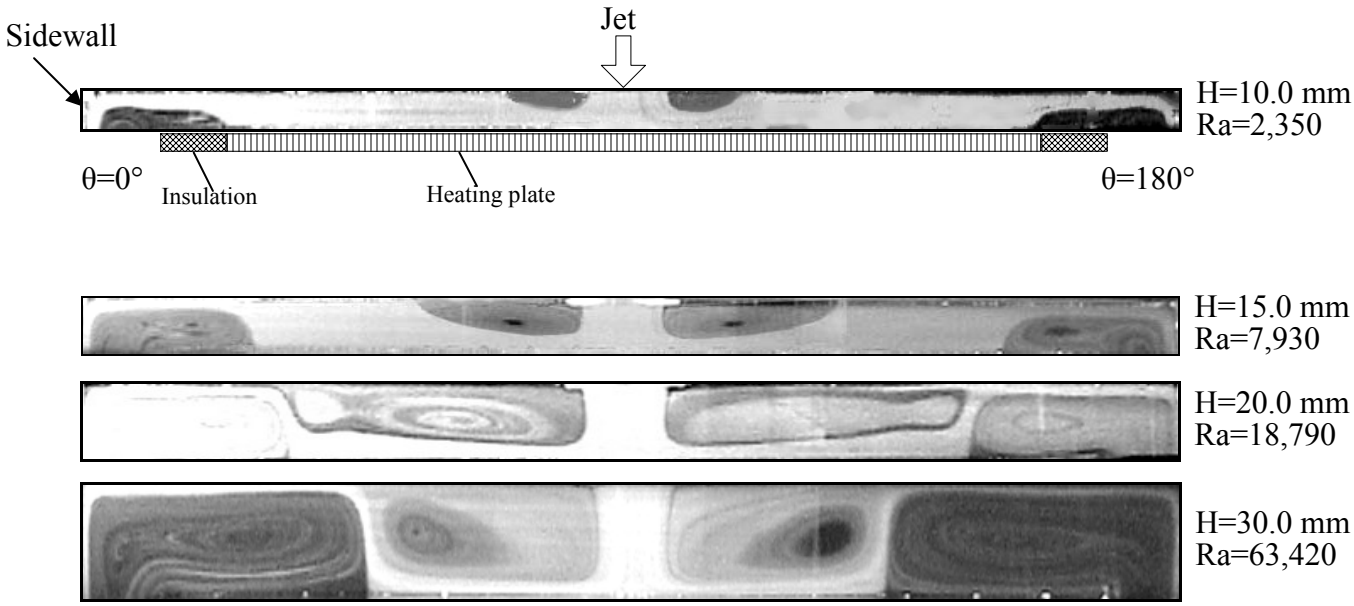

(a) ΔT=25.0℃ & Q_j=2.0 slpm (Re_j=122)

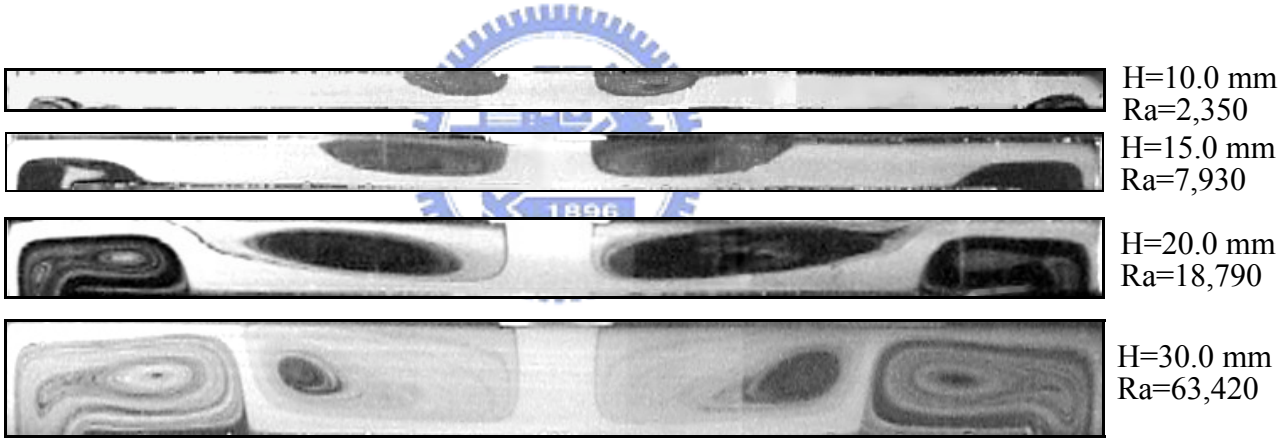

(b) ΔT=25.0℃ & Q_j=5.0 slpm (Re_j=306)

Fig. 3.51 Steady side view flow photos taken at the cross plane θ=0° & 180° for D_j=22.1 mm at given ΔT=25.0℃ for various H.

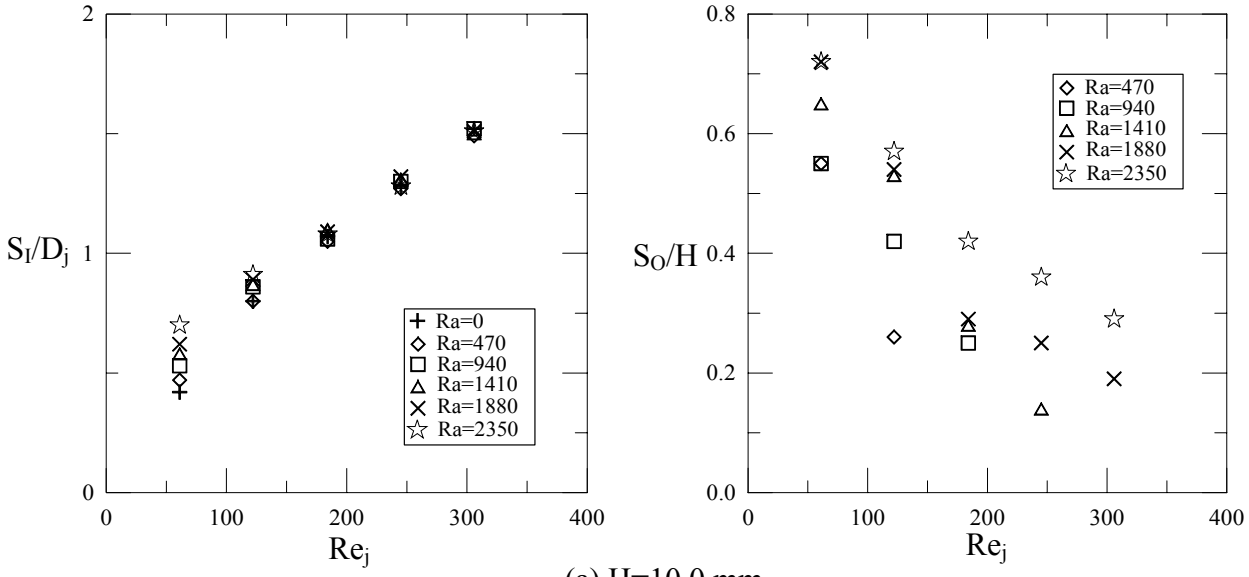

(a) H=10.0 mm

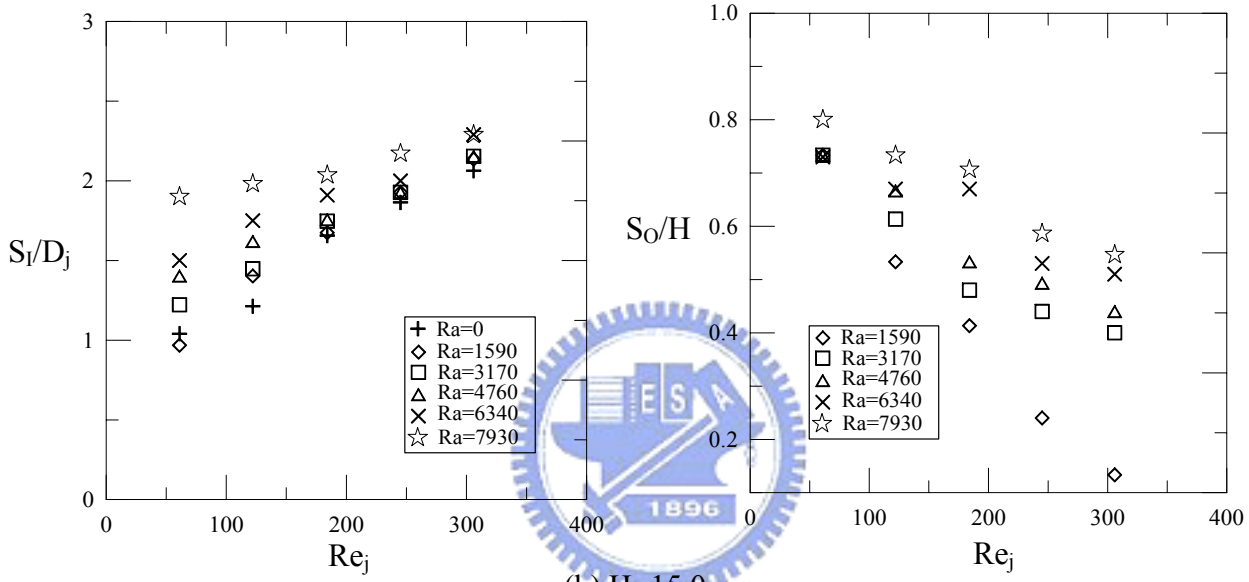

(b) H=15.0 mm

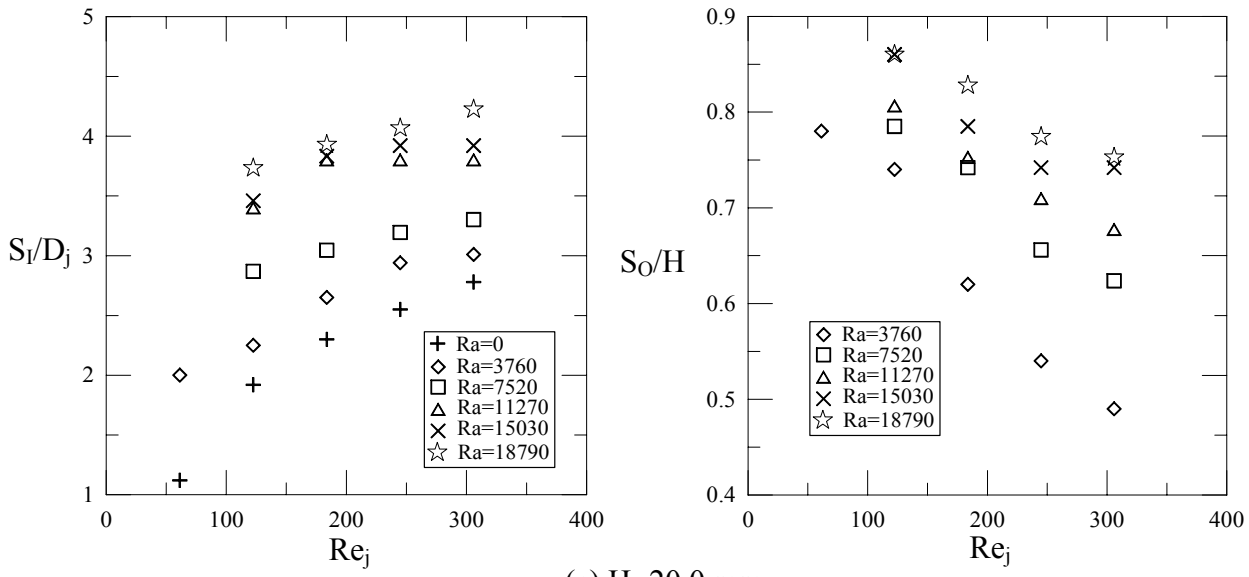

(c) H=20.0 mm

Fig. 3.52 Radial extent of the primary inertia-driven rolls with D_j=22.1 mm for H= (a) 10.0 mm, (b) 15.0 mm, and (c) 20.0 mm.

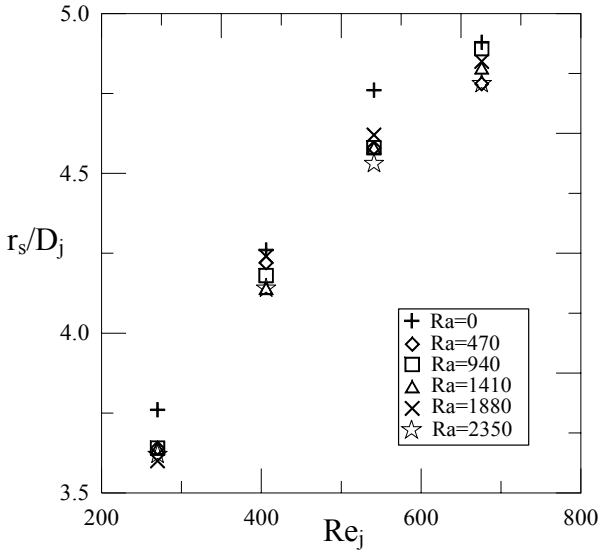

(a) H=10.0 mm

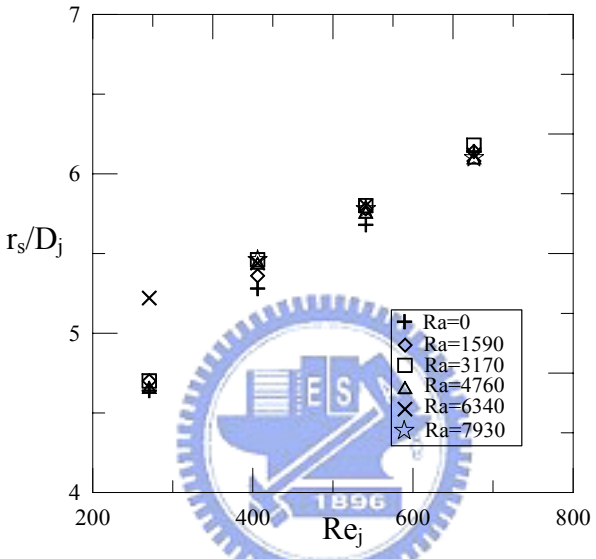

(b) H=15.0 mm

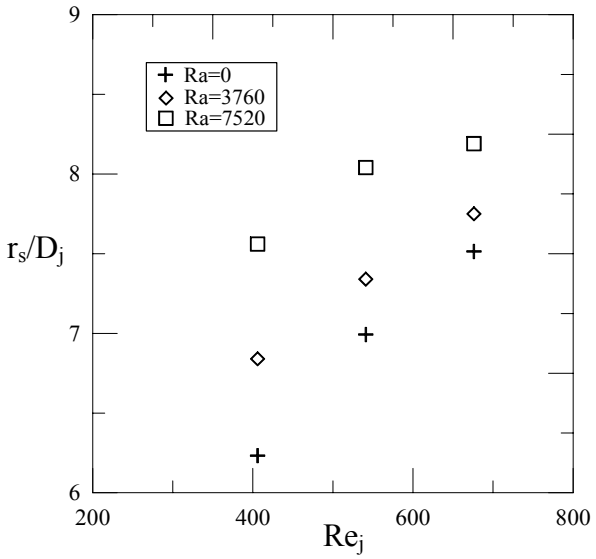

(c) H=20.0 mm

Fig. 3.53 Radial location of the secondary inertia-driven rolls with D_j=10 mm for H= (a) 10.0 mm, (b) 15.0 mm, and (c) 20.0 mm.

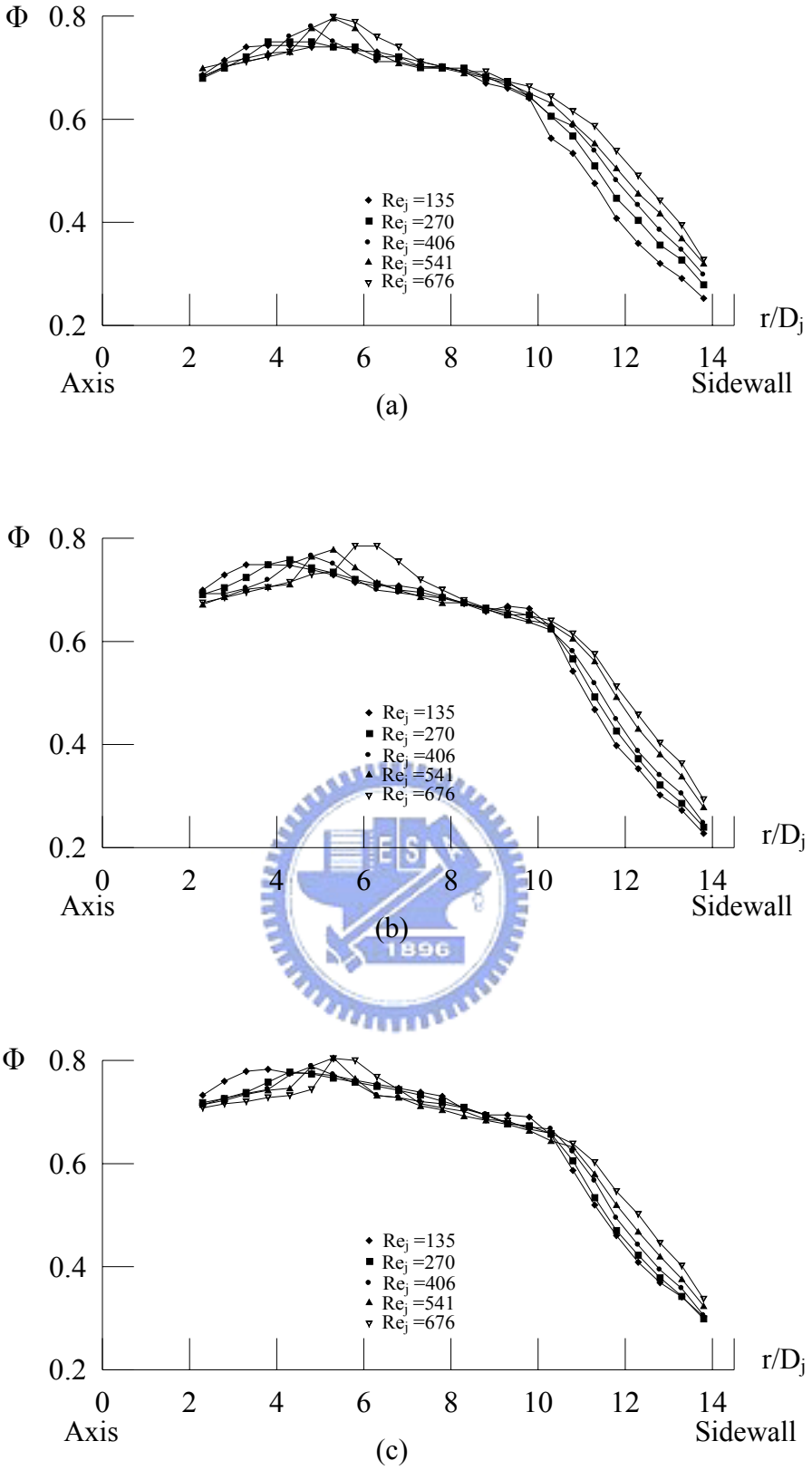

Fig. 3.54 Radial variation in non-dimensional steady air temperature with various Re_j for H=15.0 mm & D_j=10.0 mm at Z=0.5 for Ra= (a) 3,170, (b) 6,340, and (c) 7,930.

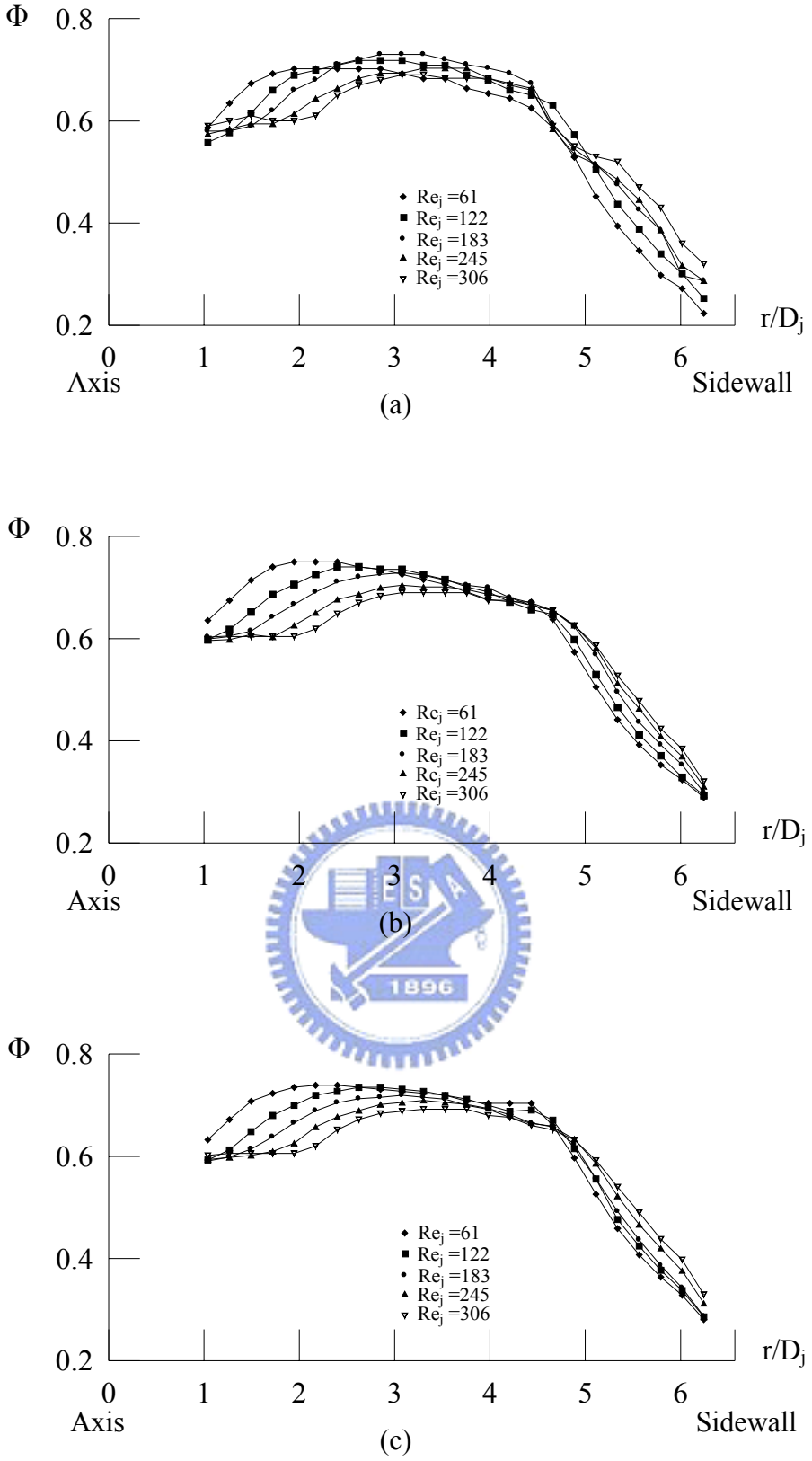

Fig. 3.55 Radial variation in non-dimensional steady air temperature with various Re_j for H=15.0 mm & D_j=22.1 mm at Z=0.5 for Ra= (a) 3,170, (b) 6,340, and (c) 7,930.

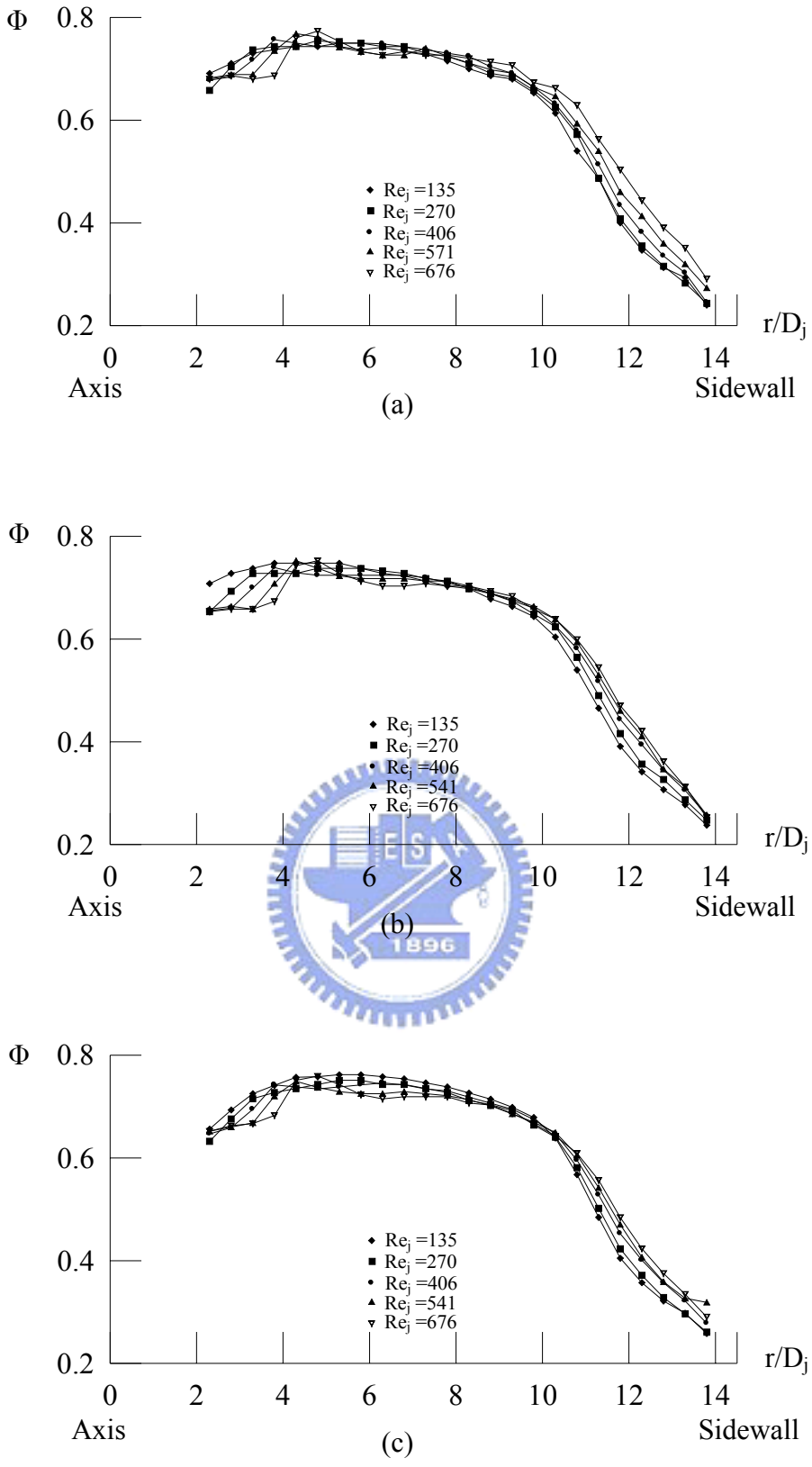

Fig. 3.56 Radial variation in non-dimensional steady air temperature with various Re_j for H=10.0 mm & D_j=10.0 mm at Z=0.5 for Ra= (a) 1,410, (b) 1,880, and (c) 2,350.

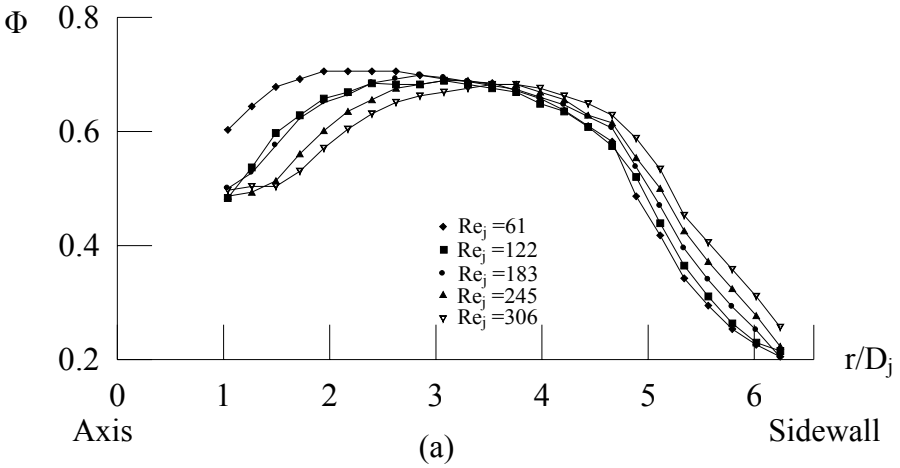

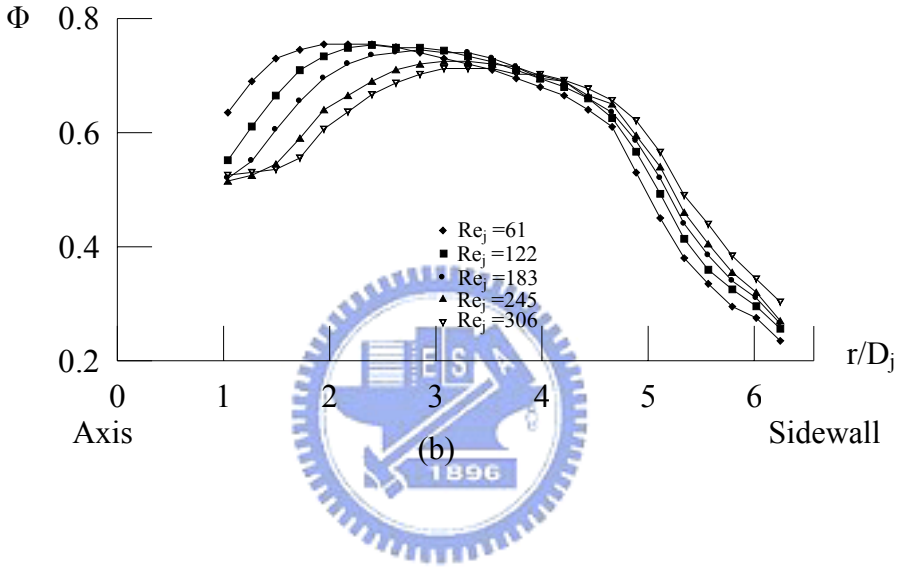

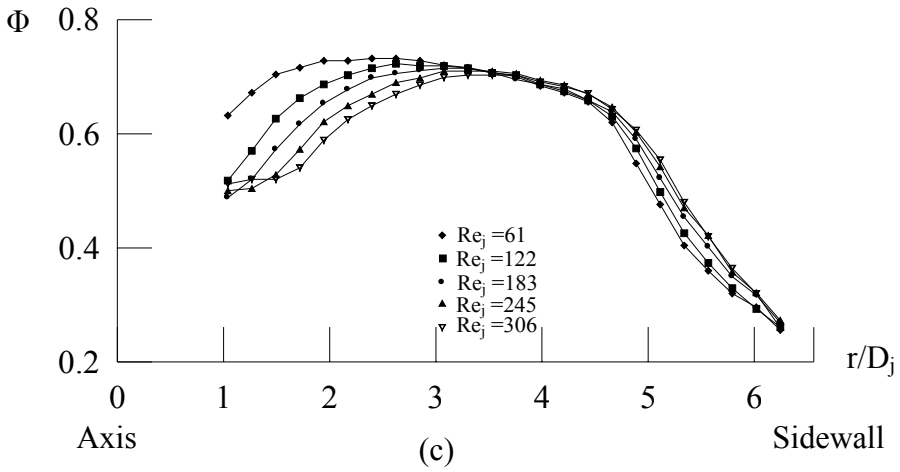

Fig. 3.57 Radial variation in non-dimensional steady air temperature with various Re_j for H=10.0 mm & D_j=22.1 mm at Z=0.5 for Ra= (a) 1,410, (b) 1,880, and (c) 2,350.